Design of Organic Materials with Unique Supramolecular Assembly for Optical, Electronic, and Biomedical Applications

by

Kyeongwoon Chung

A dissertation submitted in partial fulfillment
of the requirements for the degree of
Doctor of Philosophy
(Macromolecular Science and Engineering)
in The University of Michigan
2016

Doctoral Committee:

Professor Jinsang Kim, Chair
Professor L. Jay Guo
Assistant Professor Emmanouil Kioupakis
Associate Professor Anne J. McNeil

© Kyeongwoon Chung

2016

To My Father, Dong-Hak Chung, the Wisest and Strongest Man in My World

ACKNOWLEDGEMENTS

I definitely believe that the sincere support from many people has motivated me to finally arrive where I am. I deeply appreciate all the support I have gotten during my Ph.D. study. Professor Jinsang Kim has been an unbelievably great research advisor as well as mentor. He has been the best counselor for every aspect of my life in the US. He influenced me a lot not only as a researcher but also as a person. I really appreciate and thank him for his warm-hearted advices and guidance. I hope to emulate him to be a good mentor and advisor. The research results I have accomplished are based on some wonderful collaboration. I thank Andrew McAllister and Prof. Emmanouil Kioupakis for the wonderful computational collaborations. I thank Prof. L. Jay Guo and Prof. Ji Ho Youk for their thoughtful advices and discussions. I thank Dr. Brendan M. Leung and Prof. Shuichi Takayama for the collaboration on interesting cell experiments. I thank Dr. Antek G. Wong-Foy and Prof. Adam J. Matzger for the excellent crystal structure analyses. I thank Dr. Min Su Kim and Prof. Jeongyong Kim for the valuable collaboration in optical properties measurement. I appreciate Dr. Johannes Gierschner for the insightful discussion and beautiful collaboration in computation. I appreciate Geunseok Jang, Jongho Kim and Prof. Taek Seung Lee for their tremendous collaborative effort for the synthesis of conjugated polymer and its analysis. I thank Jong-Gyu Kim and Prof. Soo-Young Park for the collaboration in polymer X-ray analysis. I am grateful to my committee members, Prof. L. Jay Guo, Prof. Anne McNeil, and Prof. Emmanouil Kioupakis for their kind comments and discussions. Also, I deeply

appreciate Kim group members who were the best collaborators, supporters and friends during my journey in Ann Arbor. Dr. Bong-Gi Kim, Dr. David Bilby, Dr. Eun Jeong Jeong, Dr. Min Sang Kwon, Dr. Youngchang Yu, Dr. Mounggon Kim, Dr. Do Hyun Kang, Dr. Dongwook Lee, Dr. Sunghun Lee, Dr. Jiseok Lee, Dr. Sunjong Lee, Dr. Dong Hyuk Park, Dr. Sungbaek Seo, Jaehun Jung, Deokwon Seo, Apoorv Shanker, Andrew Phillips, Da Seul Yang, Joonkoo Kang, Geunseok Jang, Jongho Kim, Yoonjung Na, Yirang Im, Noah Gadja, Alica Smith, Prof. Hyong-Jun Kim, Prof. Jaesook Yun, Prof. Jin-Hyun Choi, and Prof. Ji Ho Youk, I will never forget your warm support and beautiful memories with you. At last, my father, my mother and my wife, their endless love and support gave me strength to go through all the difficulties I encountered during my Ph.D. study. Thank you and love you from the bottom of my heart.

TABLE OF CONTENTS

LIST OF FIGURES

Figure

LIST OF TABLES

Table

ABSTRACT

Rational material design is inevitable to fully realize the properties of organic conjugated materials in applications, by regulating their intermolecular packing as well as intramolecular properties. In this dissertation, molecular design strategies to control interactions and assemblies of organic conjugated materials are systematically investigated, which enables unique optoelectronic properties for various optoelectronic applications. In Chapter 2, a molecular design to control intermolecular interactions renders a unique thermally stable supercooled liquid and its shear-triggered lighting-up crystallization with 25-times fluorescence enhancement. The origin of the unique property is systematically scrutinized. Furthermore, possible biosensor application is proposed by demonstrating highly sensitive crystallization of the supercooled liquid by living cell attachment. Insightful design consideration for both intrachain and interchain properties is also critically important for conjugated polymers (CPs). In Chapter 3, molecular design of CPs' main and side chains is logically investigated to regulate optical properties. Tailored CPs exhibit identical color in solution manifesting the same intramolecular optical properties by conjugated backbone design. Contrastingly, they show distinct color gradation in the solid state due to the coined intermolecular packing propensity difference through side chain design. Latent optical information encoding using CPs as security inks is demonstrated, which reveals and conceals hidden information upon CP aggregation/deaggregation. Furthermore, expansion of the design principles for efficient CP

alignment is investigated (Chapter 4). Realization of CP alignment largely affects optoelectronic applications of CPs since it is inevitable to fully utilize CPs' anisotropic properties in devices. Previously identified molecular design rules to realize directed CP alignment are evaluated, and more detailed design factors are additionally revealed. The properties of organic conjugated materials are also influenced by environmental factors, including characteristics of a substrate and solvent molecules. In Chapter 5, a novel optical sensor is devised based on controlled subtle interaction differences between substrates, fluorescent sensory molecules, and analyte solvents. The highly selective sensor array can clearly distinguish physicochemically similar liquids; ethanol, methanol, ethylene glycol, and water. The thoroughly discussed molecular design principles in this dissertation depict an insightful picture on how unique optoelectronic properties of conjugated organic molecules and polymers can be designed and fully utilized in various applications.

CHAPTER 1

Introduction

The section 1.3.2 of this chapter has been published in K. Chung, Y. Yu, M. S. Kwon, J. Swets, J. Kim, J. H. Youk, Assembly and alignment of conjugated polymers: materials design, processing, and applications. *MRS Commun.* **5,** 169–189 (2015) – Published by Materials Research Society.

1.1. Conjugated Organic Materials in Applications

Synthetic organic materials have become ubiquitous in our daily life; right from simple

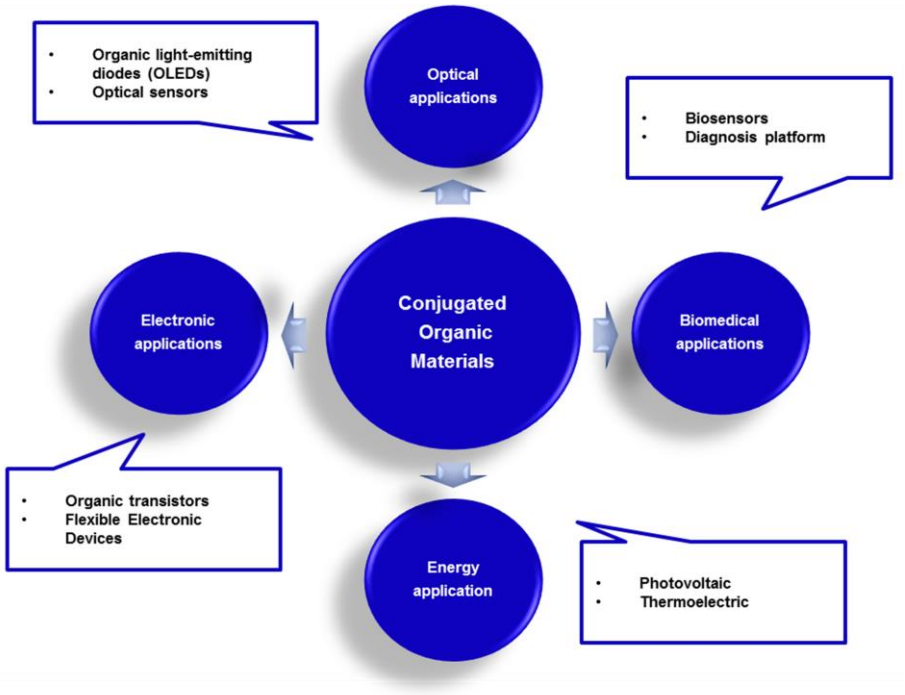

Figure 1.1 Various applications of conjugated organic materials.

plastic bags and bottles to high tech machinery components. Beyond the traditional organic materials and its applications, semiconducting conjugated organic materials have been widely investigated in recent decades. The semiconducting optoelectronic properties of conjugated organic materials, including small molecules and polymers, originates from the alternating saturated and unsaturated bonds in the chemical structure, which results in p-orbital overlap through the conjugation.[1] Because of their tunable optoelectronic properties through molecular design and their advantages such as light-weight, low cost solution-based processability, and applicability to flexible and wearable devices, the conjugated organic materials have been extensively researched for various applications (**Figure 1.1**) including optical applications (organic light-emitting diodes (OLEDs)[2,3] and optical sensors[4,5]), electronic applications (organic thin film transistors (OTFTs)[6,7]), energy devices (organic photovoltaics (OPVs)[8–10] and organic thermoelectrics[11,12]), and biomedical applications (biosensors[13–15]).

1.2. Conventional Intrachain Design Strategies for Conjugated Organic Materials

Rational material design, especially chemical structure design in organic materials, is very important to realize desired optimal characteristics for various applications. Because the number of possible chemical structure is infinite, the design of organic materials has a wide window to accomplish target properties such as absorption, emission, energy levels, and charge mobility. The intrinsic intramolecular properties of conjugated organic materials, such as optical and electrochemical properties in dilute solution, are mainly determined by the conjugated chemical structure of the materials. Material designing strategies for regulating the intramolecular properties have been widely investigated, including conjugated building block modification and addition of functional groups.

1.2.1. Building Block Modification

Modification of conjugated chemical building blocks has a strong impact on the properties of organic materials. By applying different types of conjugated building blocks, the intramolecular properties of the materials can be efficiently adjusted. For example, conjugated polymers (CPs) with phenyl linkage, such as poly(*p*-phenylene) and polyfluorene, show bluish emission resulting from a large band gap even in a high-molecular weight regime due to the twisted conformation of phenyl linkages, which results in restricted effective conjugation.[16–18] In contrast, CPs with planar thienyl analogues, for example regioregular poly(3-hexylthiophene-2,5-diyl) (rrP3HT), has orange emission with an absorption band edge around ca. 540 nm.[19,20]

The building block modification is a widely investigated design strategy especially for the low band gap CPs in the energy and optoelectronic applications. One of the most promising strategies to build low band gap CPs is an alternation of electron-donating (electron-rich) building block and an electron-accepting (electron-deficient) building block in the CP analogue. The alternating electron-donating and electron-accepting building block enables intramolecular charge transfer

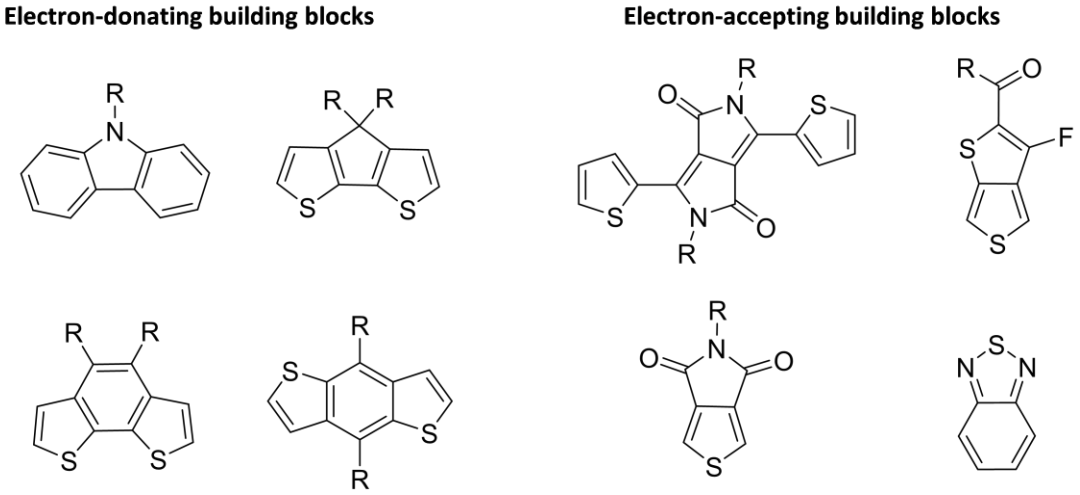

Figure 1.2 Examples of electron-donating and electron-accepting building blocks for CPs.

and molecular orbital hybridization, resulting in a narrow band gap.[21–23] Representative examples of electron donor and acceptor building blocks are presented in **Figure 1.2**.

Furthermore, systematic modification of the building block allows sophisticated modulation of the CPs' properties. Kim *et al.* demonstrated gradual shift in absorption range as well as highest occupied molecular orbital (HOMO) and lowest unoccupied molecular orbital (LUMO) in a series of CPs via modification of the strength of the electron-accepting building blocks.[23] The electron-accepting power of the building blocks were controlled by applying different electron-withdrawing moieties in the building blocks for PBTCT, PBTCTO, PBTPDO, and PBTFDO (**Figure 1.3a**). As electron-accepting strength of the building block increases (from PBTCT to PBTFDO), the polymers exhibit red-shifted absorption range and a narrowed band gap (**Figure 1.3b**). The solution color of the CPs clearly represents the gradation in absorption: orange in PBTCT, purple in PBTCTO, blue in PBTPDO, and greenish blue in PBTFDO (**Figure 1.3c**). It is also confirmed that the LUMO energy level of the CPs gradually

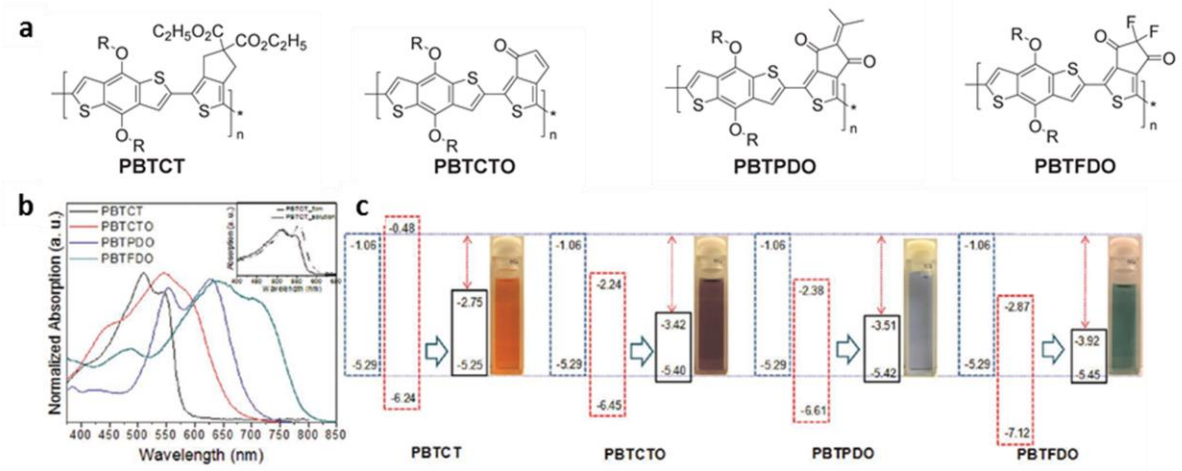

Figure 1.3 Chemical structures and properties of the designed CPs with different electron-accepting building blocks. (a) Chemical structures of the CPs. (b) UV-vis absorption spectra of the CP solutions (in chloroform). (c) Color and energy levels of the CPs and applied monomers. [23] (Reproduced with permission, copyright 2013 WILEY-VCH Verlag GmbH & Co. KGaA, Weinheim)

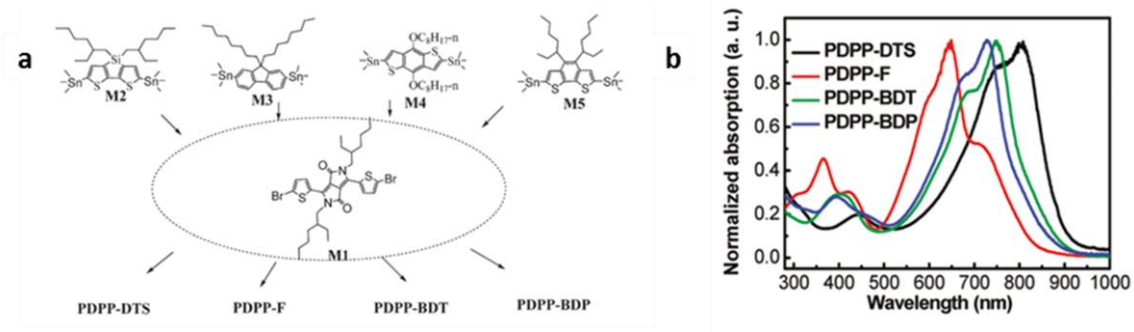

Figure 1.4 Chemical structures and optical properties of the designed CPs with different electron-donating building blocks. (a) Chemical structures regarding the designed CPs. (b) UV-vis absorption spectra of the CP solutions (in chloroform).[24] (Reproduced with permission, copyright 2009 American Chemical Society)

decreases as the electron-accepting power of the building blocks increases (**Figure 1.3c**). Similarly, Yang *et al.* presented a series of CPs with different electron-donating building blocks which exhibits gradation in absorption spectrum resulting from building block modification (**Figure 1.4**).[24]

1.2.2. Addition of Functional Group

The addition of functional group is an important design strategy for the organic conjugated materials, which is widely utilized especially to modify energy level of CPs for OPV application. Introduction of fluorine to the CP analogue, for example, has been reported to accomplish deeper HOMO level of CP, which is directly correlated to the open circuit voltage (V_{oc}) characteristic in the OPV device application.[25–28] The fluorine atom is the most electronegative element which has a comparable size with hydrogen. Therefore, addition of fluorine in the conjugated main chain of CPs enables the energy level modification without building massive steric hinderance.[25] Yu *et al.* presented CPs with and without fluorine atom attached to the thieno[3,4-*b*]thiophene building block (PTB4 and PTB5 in **Figure 1.5a**); PTB4 which has fluoride in the CP analogue exhibits HOMO level deeper than PTB5 by about 0.1 eV (**Figure 1.5b**).[28]

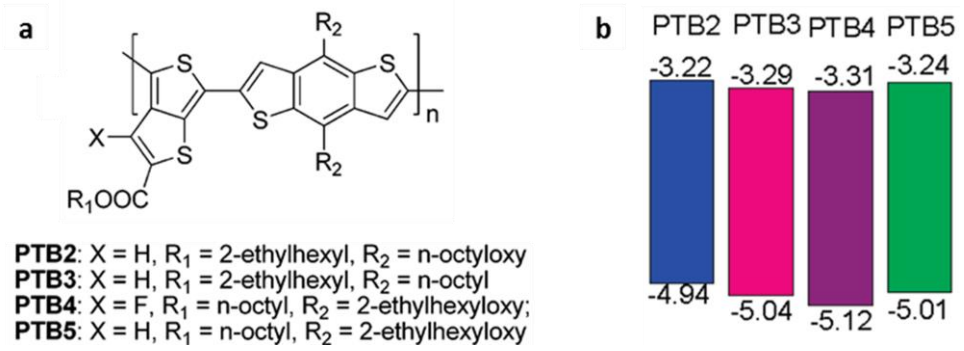

Figure 1.5 Chemical structures and energy levels of the CPs: Introduction of fluorine atom and alkoxy side chains in the designed CP analogues. (a) Chemical structures of the CPs. (b) HOMO and LUMO energy levels of the CPs.[28] (Reproduced with permission, copyright 2009 American Chemical Society)

In addition, Yu *et al.* investigated CPs with different functional groups on the side chain (PTB2 and PTB3 in **Figure 1.5a**).[28] The alkoxy functional group has better electron-donating power than alkyl side chain, resulting in shallow HOMO energy level of a CP. As a consequence, PTB2 is observed to have HOMO level of -4.94 eV that is raised about 0.1 eV from the HOMO energy level of PTB3 (**Figure 1.5b**).[28] Similarly, it is reported that replacing alkoxy side chain to the alkylthienyl side chain in the electron-donating benzo[1,2-*b*:4,5-*b'*]dithiophene building block allows slightly deeper energy levels of a CP.[29]

1.3. Intermolecular Property of the Organic Materials

The design of conjugated chemical structure also partially affects the intermolecular packing properties. For instance, utilizing planar building blocks in CP analogue, such as thiophene linked diketopyrrolopyrrole (DPP), promotes effective co-facial packing of conjugated main chain, leading to enhanced charge mobility in CP films.[30] In addition, atom substitution in the CP building block has been suggested as one of the strategies to control interchain interactions. In the literature, substitution of thiophene (sulfur) to selenophene (selenium) in a CP main chain

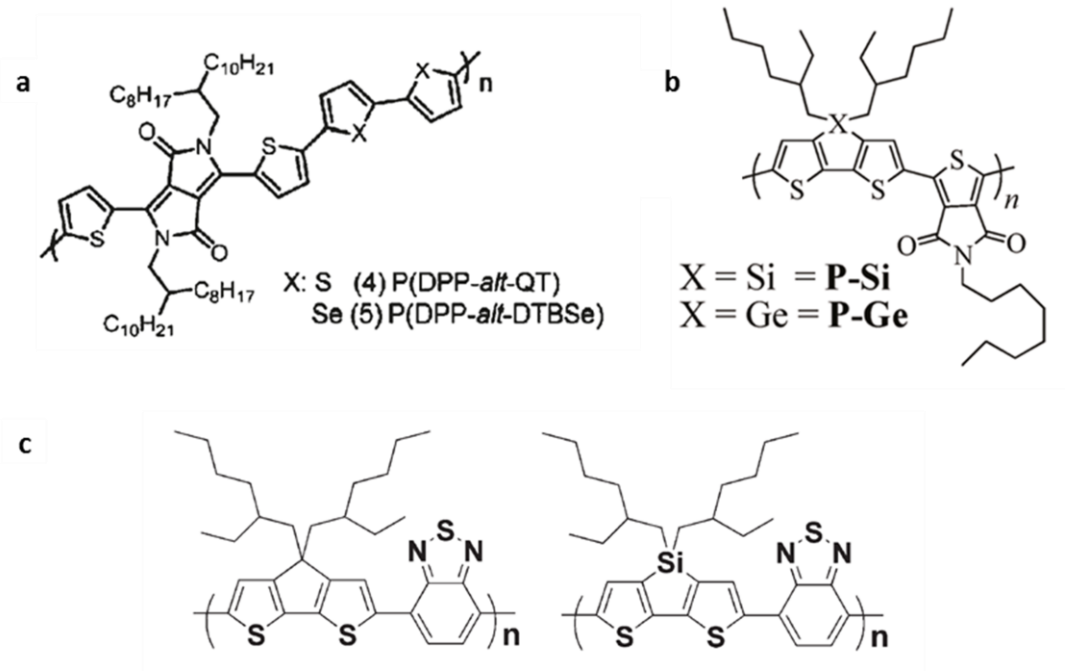

Figure 1.6 Chemical structures of the CPs: Atom substitution. (a) Substitution of sulfur to selenium.[30] (Reproduced with permission, copyright 2011 American Chemical Society) (b) Substitution to germanium.[35] (Reproduced with permission, copyright 2011 American Chemical Society) (c) Substitution of carbon to silicon.[32] (Reproduced with permission, copyright 2010 WILEY-VCH Verlag GmbH & Co. KGaA, Weinheim)

analogue (**Figure 1.6a**) is proposed as a design strategy to enhance chain interactions between neighboring chains because of a stronger heteroaromatic interaction, resulting in improved charge transport property.[30,31] Substitution of a carbon atom to a silicon[32–34] or a germanium atom[35] in the conjugated CPs' main chain (**Figure 1.6**, **b** and **c**) has also been reported as a strategy to induce stronger interchain packing, possibly due to a longer bond length in Si-C and Ge-C compared to that of C-C bond, which provide reduced steric hindrance of alkyl side chains when the conjugated main chains pack each other.

Nevertheless, it is still challenging to fully predict and control intermolecular packing of small molecules and polymers compared to the intrinsic properties of the conjugated organic materials, since the intermolecular packing properties can be influenced by various factors.[36,37] For example, to date, it is likely not possible to predict the tendency of a given molecular

structure to exhibit multiple crystalline phases with different molecular arrangement (polymorphism) or the number of energetically accessible crystalline phases.[36] However, because materials are generally utilized in solid state for real applications, it is very important to consider intermolecular packing properties of the conjugated organic materials together with their intrinsic properties from the materials design point of view. Moreover, distinct intermolecular packing of the organic materials can enable unique phenomenon: For instance, crystal polymorphism, aggregation-induced enhanced emission (AIEE), and CP alignment.

1.3.1. Molecular System: Polymorphism & AIEE

1.3.1.1. Polymorphism of Organic Molecules

Polymorphism is a phenomenon that a compound exhibits at least two different crystalline solid phases having different arrangements of the component (molecules or atoms).[38] For example, graphite and diamond having different crystalline structure but made of same chemical constituent (carbon) are polymorphs.[39] It is not restricted only for organic molecules but observed in various type of materials including metals, inorganic compounds and organometallic compounds.[38] Furthermore, the polymorphism has been a research field of interest especially in chemistry, materials science, and pharmaceutical science since different polymorphs can have different characteristics (such as density, melting point, solubility, hardness, reactivity, and color) through different intermolecular packing structure regardless of their identical chemical structure.[38]

As a practical example of polymorphism, we can refer ‘chocolate’. A chocolate is made with cocoa butter, and the fatty acids in the cocoa butter have six different polymorphs.[40] The six polymorphs have different melting points and conditions to achieve it. In the commercial

chocolate products, only one type of polymorph, Form V (T_m= 29~34 ^oC), has been utilized considering flavor release, glossy appearance, feeling in mouth, and processability of chocolate.[40]

In pharmaceutical science, polymorphism may be directly related to the efficacy of the medication. Since polymorphs exhibit difference in free energy due to different intermolecular packing structure, the solubility of each crystal form can vary, and therefore it can result in discrepancy in bioavailability of the solid dosage.[41] Ritonavir, which is a protease inhibitor commercialized in 1996 for treating Acquired Immunodeficiency Syndrome (AIDS), was identified to have only one crystal form during development.[41] However, in 1998, it was revealed that a polymorph of ritonavir crystallized in ethanol/water solution (commercialized medication formulation) because of solubility difference of two forms of crystal polymorphs.[41] The newly observed polymorph was severely less soluble so that the formulation of ritonavir solution was 400% supersaturated condition for the less-soluble polymorph even though this solution formulation was not saturated condition for originally investigated crystal form of ritonavir.[41] This risk seriously threatened the AIDS patients' safety, and immediate reformulation of the medication was critically demanded.[41]

Polymorphism of organic conjugated materials has also been widely investigated. As a representative example, 5-methyl-2-[(2-nitrophenyl)amino]-3-thiophenecarbonitrile, so called 'ROY' for its red, orange and yellow colored crystals, was reported to have ten polymorphs (**Figure 1.7**).[39] Seven polymorphs of ROY have been investigated for their crystal packing structures. The distinct color shifts between polymorphs are attributed to the difference in absorption spectra, and this absorption difference results from the degree of conjugation depending on the conformational difference of ROY molecule in its crystal structure.[39] As

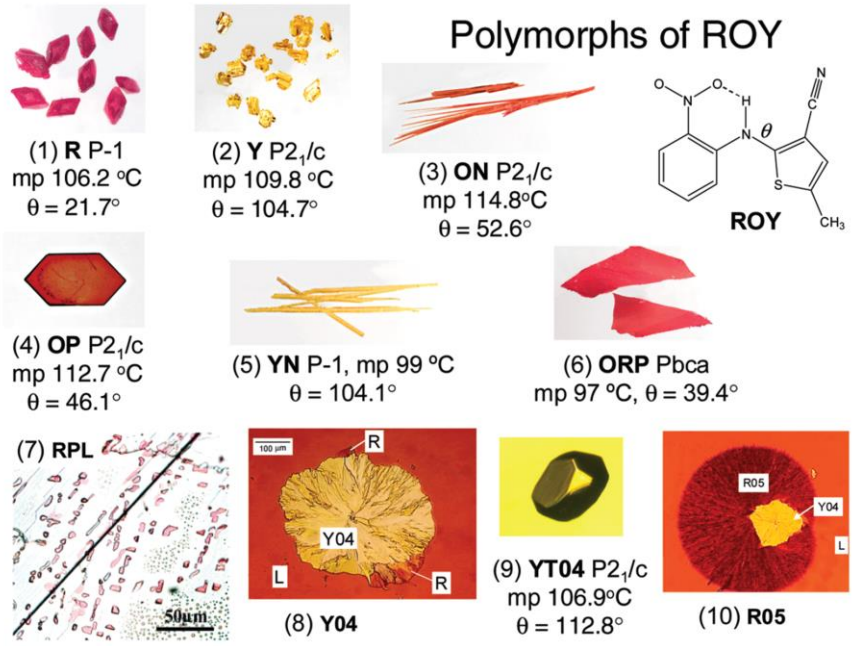

Figure 1.7 Ten polymorphs of 5-methyl-2-[(2-nitrophenyl)amino]-3-thiophenecarbonitrile (ROY).[39] (Reproduced with permission, copyright 2010 American Chemical Society)

torsional angle, θ in **Figure 1.7**, decreases, the visible absorption spectrum shift to longer wavelength.[39,42] Different from other polymorphic systems which may maintain only certain polymorph under specific range of temperature and pressure, ROY is an interesting system which can produce multiple kinetically stable polymorphs simultaneously from the same environment; this characteristic enables ROY as an important molecular system for investigation of the crystallization process.[39]

1.3.1.2. Aggregation-induced Enhanced Emission (AIEE) of Conjugated Organic Molecules

Generally, fluorescent organic conjugated molecules exhibit high fluorescence efficiency in a dilute solution, while fluorescence quantum yield decreases in the aggregated state. This concentration quenching (or aggregation-caused quenching) is mainly ascribed to the developed non-radiative deactivation process induced by intermolecular interactions, such as excimer

formation, excitonic coupling, energy migration to the impurity trap, etc.[43,44] Especially, planar aromatic molecules (and CPs) are prone to generate efficient molecular stacking due to strong π-π interaction, causing severe concentration quenching.[45,46] The strong π-π stacking is advantageous for the charge transport properties and, therefore, electronic applications of organic conjugated materials. However, in terms of optical device applications including OLEDs, the concentration quenching may obstruct application of the conjugated organic materials as an active layer material in the device.

Opposite to this common understanding, several classes of organic molecules that exhibit higher fluorescence quantum yield (QY) in aggregated state than that of dilute solution state have been reported since early 2000. This aggregation-induced enhance emission (AIEE) (or Aggregation-induced emission (AIE)) is realized by intermolecular packing in specific organic conjugated molecular systems including cyanostilbene derivatives[44] and phenylsilole derivatives.[47] The AIEE behavior of cyanostilbene derivatives are explained by the aggregation-induced conformational change as well as J-type packing of molecules.[44,45] In solution, a cyanostilbene derivative, CN-MBE, (**Figure 1.8**) has a twisted conformation with restricted effective conjugation, causing negligible fluorescence.[44] However, in aggregated state (nanoparticle formation), aggregation-induced planarization enables extended effective conjugation and increases oscillator strength of the molecular system (**Figure 1.8a**).[44] Furthermore, the polar and bulky cyano group in CN-MBE prevents face-to-face H-type aggregation which may cause severe concentration quenching, but forms J-type aggregation.[44] The formation of J-type aggregation in CN-MBE system was further investigated with reference compound DPST which does not have cyano functional group in its molecular structure (**Figure 1.8b**). DPST exhibits blue-shifted absorption spectrum as aggregation develops (as water

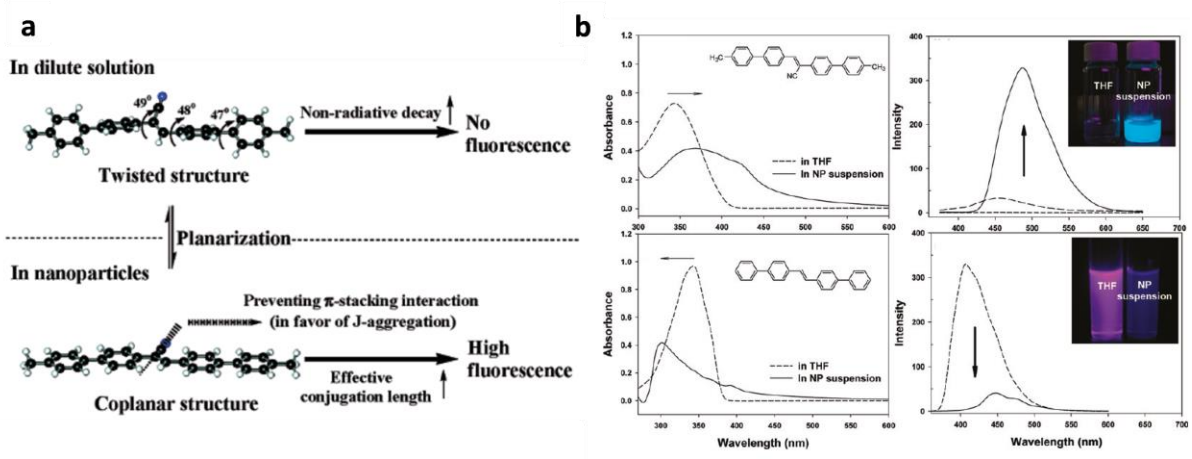

Figure 1.8 Aggregation-induced enhanced emission (AIEE) (a) Proposed mechanism of enhanced emission of CN-MBE molecular system.[44] (Reproduced with permission, copyright 2002 American Chemical Society) (b) Absorption (left) and photoluminescence (right) characteristics of CN-MBE (top) and DPST (bottom) in tetrahydrofuran (THF) solution and nanoparticle suspension (80 vol% water in THF).[45] (Reproduced with permission, copyright 2011 American Chemical Society)

fraction increases in THF/water mixed solvent system) which is a typical observation from the H-type aggregation formation, and shows massive photoluminescence (PL) quenching (**Figure 1.8b**).[44] In contrast, CN-MBE shows enhanced emission in PL and new absorption band around 420 nm because of J-type aggregation formation (**Figure 1.8b**).[44,45]

On the other hand, phenylsilole derivatives, hexaphenylsilole (HPS) for example (**Figure 1.9a**), have phenyl rings attached to the silole group, which exhibit rotational motion in dilute

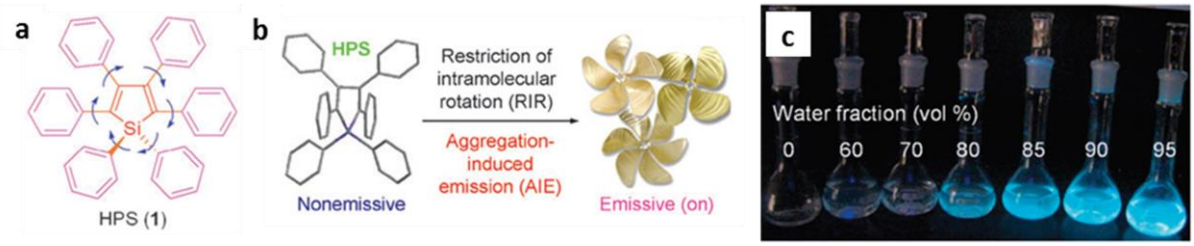

Figure 1.9 Aggregation-induced emission (AIE) of hexaphenylsilole (HPS). (a) Chemical structure of HPS. (b) Proposed mechanism of enhanced emission. (c) Fluorescence image of HPS solutions in acetonitrile-water mixture.[48] (Reproduced with permission, copyright 2009 The Royal Society of Chemistry)

solution.[46,48] This intramolecular rotation of phenyl rings annihilates the excited state non-radiatively so that the molecular system is non-emissive in solution.[46,48] However, in an aggregated state, the rotational motion of phenyl rings is restricted and the molecular system becomes fluorescent (**Figure 1.9b**).[46,48] In **Figure 1.9c**, the enhanced fluorescence of HPS is well illustrated as aggregation develops (as water fraction increases in water/acetonitrile mixed solvent system).

1.3.2. Conjugated Polymer System: CP alignment[49]

CPs have a long, one-dimensional (1-D), rigid rod-like main chain structure with *p*-orbital overlaps along the main chain. Due to these 1-D *p*-orbital overlaps, CPs exhibit intriguing anisotropic properties such as charge transport, absorption, and emission. Therefore, the macroscopic alignment and assembly of CPs are essential to fully utilize their optical and electronic properties.

The degree of alignment of CPs in thin films is quantified by the dichroic ratio, which is defined as the ratio of the intensity of the absorption (or emission) parallel to the alignment direction to that of the perpendicular to the alignment direction (dichroic ratio = $I_{//}/I_{\perp}$). Although the dichroic ratio is generally derived from the polarized UV-vis absorption or photoluminescence (PL) intensity, the dichroic ratios derived from the integral of the polarized absorption or emission spectrum ($A_{//}/A_{\perp}$) and mobility anisotropy ($\mu_{//}/\mu_{\perp}$) have also been used to measure the degree of alignment in some cases. If the dichroic ratio is 1, absorption or emission is independent of the polarized direction implying that there is no alignment and instead the CPs are randomly oriented. As CP alignment develops, the dichroic ratio increases.

Macroscopic alignment of CPs is challenging because of their easy aggregation during solvent drying, which is mainly due to strong π-π interactions between rigid rod-like conjugated main chains.[37] The low mobility and randomly oriented growth of CP aggregates hampers the capability of macroscopically directed CP alignment.[37] Nevertheless, various processing methods, including Langmuir-Blodgett (LB) technique, mechanical rubbing, nanoimprinting, electrospinning, and directional solidification in addition to the use of pre-patterned substrates and foreign matrix methods, have been investigated to accomplish a certain level of macroscopic alignment for several specific types of CPs. However, it is still elusive as to what CPs are suitable for alignment processing, and what material designs are crucial to achieving well-defined macroscopic alignment. Insight into material design is necessary to identify characteristics of CPs that allow for alignment in order for their potential anisotropic properties to be maximized in solid state applications. Otherwise, it is likely that severe difficulties in achieving directed organization will be encountered even if state of the art processing techniques for CP alignment are utilized.

1.3.2.1. Langmuir-Blodgett Technique

Langmuir-Blodgett (LB) technique is one of the promising methods to produce well-defined CP alignment.[18,50] Schematic illustration of LB technique is presented in **Figure 1.10a**; the CP solution is spread at the

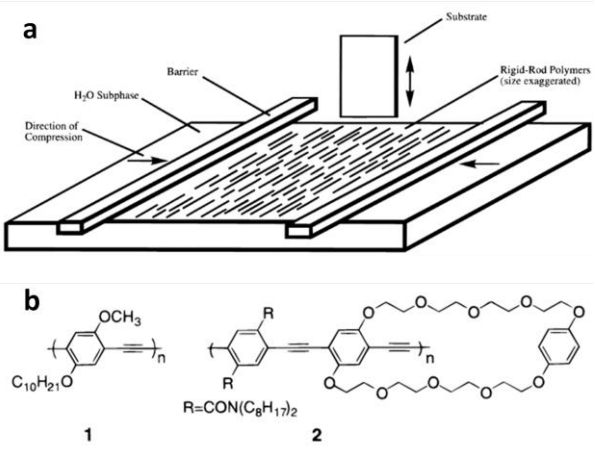

Figure 1.10 Langmuir-Blodgett (LB) technique. (a) Schematic illustration of LB deposition geometry. (b) Chemical structure of prepared PPEs.[50] (Reproduced with permission, copyright 1999 American Chemical Society).

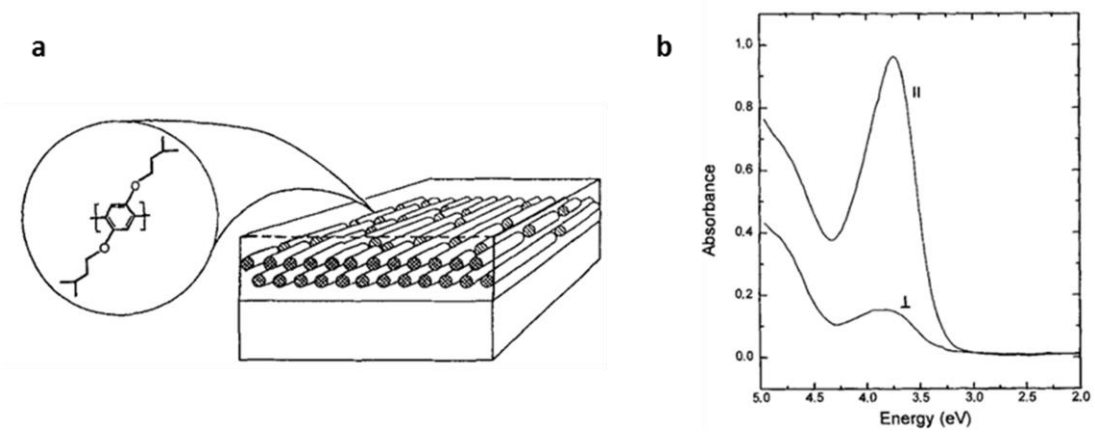

Figure 1.11 Langmuir-Blodgett (LB) technique. (a) Schematic illustration of molecular orientation of PPP in the LB film. (b) Polarized absorption spectra of 100 monolayers LB film under parallel (//) and perpendicular (⊥) to the dipping direction.[18] (Reproduced with permission, copyright 1996 WILEY-VCH Verlag GmbH & Co. KGaA, Weinheim).

air-water interface, and under compression of the two barriers, the rigid rod-like CPs align normal to the compression direction. The aligned CP monolayer is then transferred to a substrate through up-stroke and down-stroke movement of the substrate through the monolayer. Neher *et al.* reported alignment of poly(*p*-phenylene) (PPP) via the LB technique.[18] PPP chains are aligned parallel to the substrate dipping direction (**Figure 1.11a**). The dichroic ratio in absorption was observed ca. 5 (**Figure 1.11b**). Swager *et al.* demonstrated the alignment poly(phenylene ethynylene)s (PPEs) via the LB method.[50] The two synthesized PPEs (**Figure 1.10b**) were successfully aligned to the dipping direction of the substrate, and exhibited an anisotropic optical property with an absorption dichroic ratio of 3.4~6.3.

1.3.2.2. Mechanical Rubbing

Mechanical rubbing is a well-known processing method for preparing a polyimide to align liquid crystalline (LC) materials. This process has also been utilized in CP alignment by rubbing

a CP film with a fabric or substrate, like quartz, generally at an elevated temperature.[51–54] Alignment of polydiacetylene (PDA) was demonstrated by mechanically rubbing a

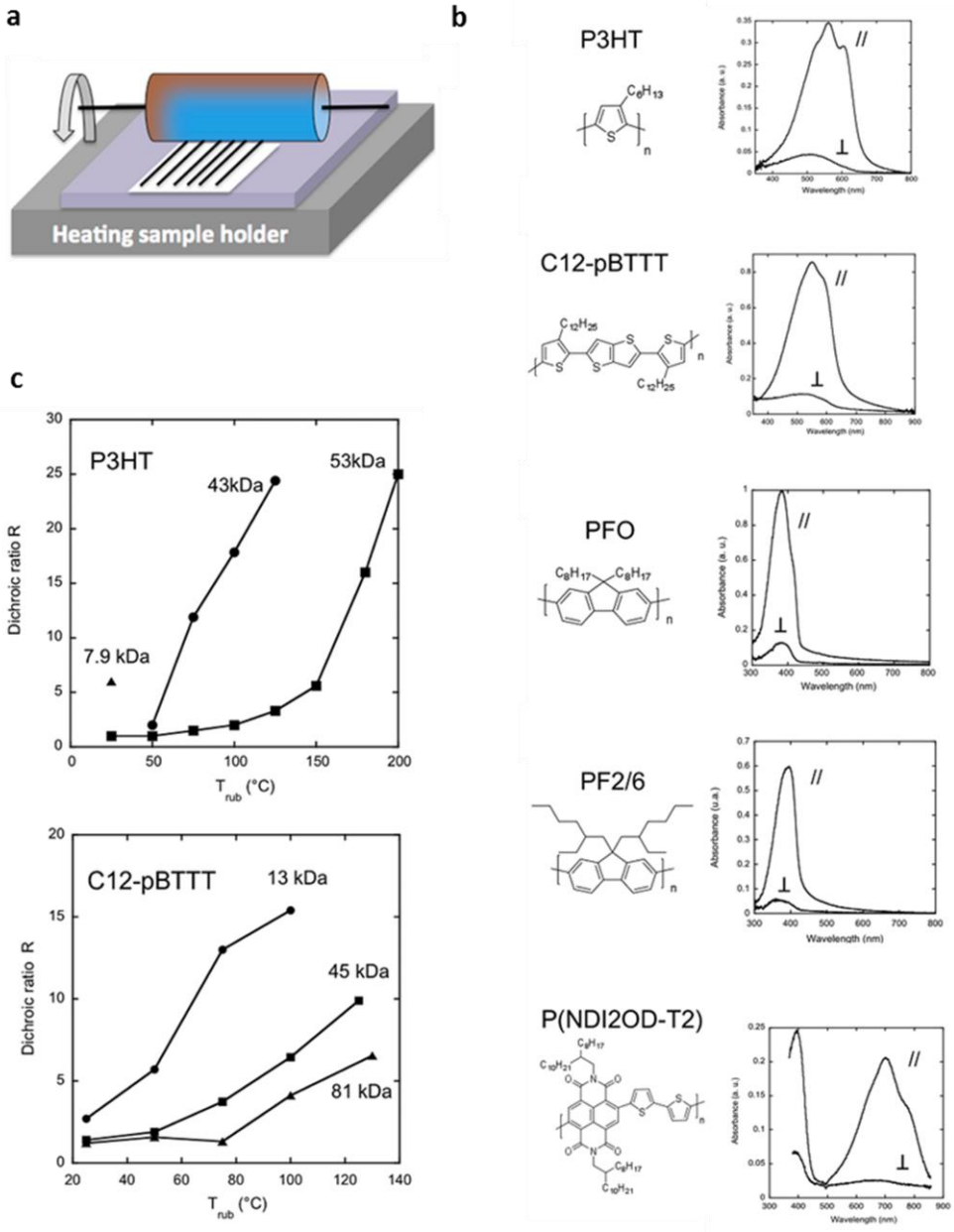

Figure 1.12 CPs alignment via mechanical rubbing. (a) Schematic illustration of homemade rubbing machine. (b) Polarized absorption spectra under parallel (//) and perpendicular (⊥) to the rubbing direction of highly oriented various CPs' films prepared by high temperature rubbing. (c) Rubbing temperature dependence of dichroic ratio at 605 nm for P3HT and C12-pBTTT with different molecular weights.[54] (Reproduced with permission, copyright 2014 American Chemical Society).

photopolymerized PDA film with a silicon cloth and an absorption dichroic ratio of 8 was observed.[51] Regioregular poly(3-hexylthiophene) (rrP3HT) was also reported to be aligned by mechanical rubbing. A spincast 20 nm thick P3HT film rubbed with a piece of velvet about 10 times at 100 ^{o}C, and showed a dichroic ratio of 5.1 in absorption.[52] In addition, Yang and Moses *et al.* reported a dichroic ratio around 10 from a rrP3HT film rubbed with a quartz plate at 95 ^{o}C.[53]

Recently, Brinkmann and coworkers demonstrated mechanical rubbing induced alignment of various CPs.[54] In their procedure, mechanical rubbing was applied by a homemade rubbing instrument on a polymer film prepared by the doctor blade method (**Figure 1.12a**). As illustrated in **Figure 1.12b**, different types of CPs were aligned by mechanical rubbing and were shown to have high absorption dichroic ratios. In the specific case of a rubbed rrP3HT film at 180 ^{o}C, an absorption dichroic ratio above 25 was observed. The correlation between the degree of alignment and the rubbing temperature and the molecular weight of CPs were further investigated. As the rubbing temperature increased, the dichroic ratio also increased (**Figure 1.12c**). It was also found that as the molecular weight of the CP increases, a higher rubbing temperature is required to achieve a similar dichroic ratio (**Figure 1.12c**). It is possible that this is due to molecular weight dependence of the crystal to LC transition temperature.

1.3.2.3. Nanoimprinting

CP alignment has also been accomplished by nano-confinement of polymer chains by nanoimprinting. Friend, Kim and Huck *et al.* reported a method for the alignment of LC CP, poly(9,9-dioctylfluorene-*co*-benzothiadiazole) (F8BT), via nanoimprinting using a silicon mold

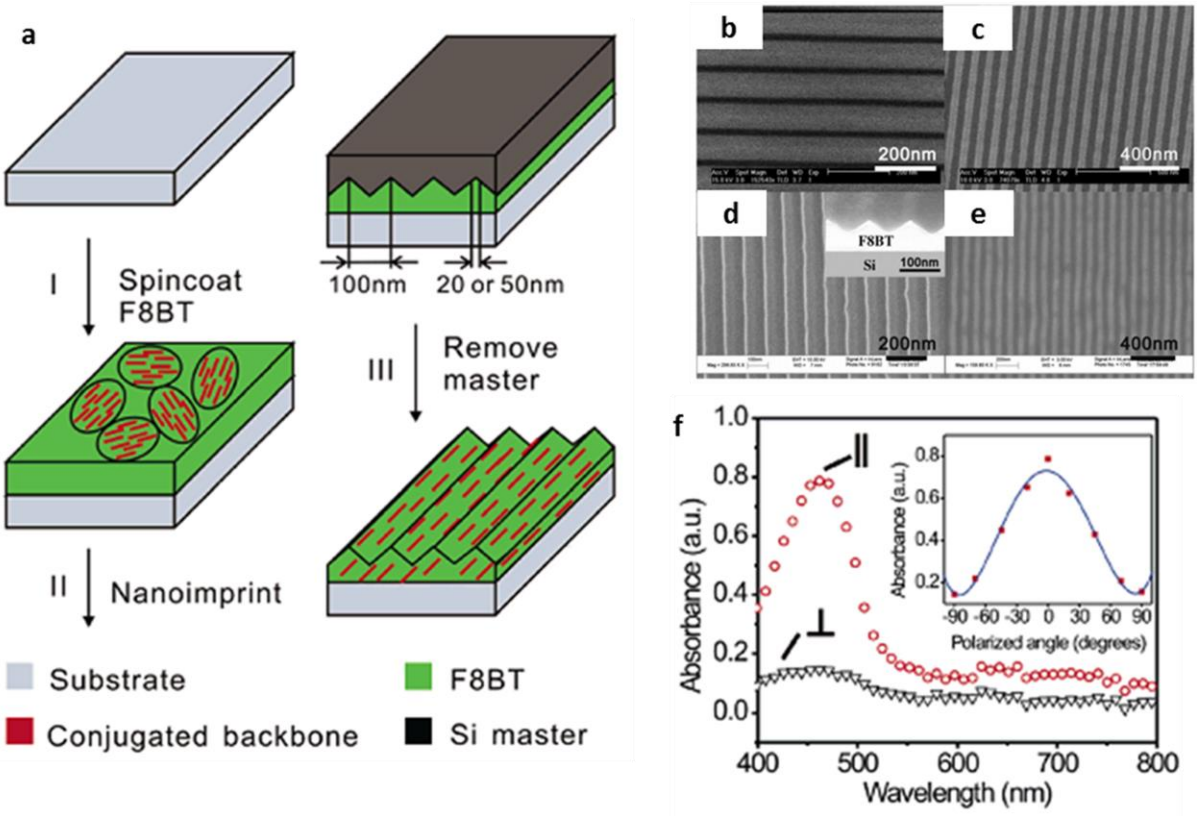

Figure 1.13 CPs alignment through nanoimprinting. (a) Schematic illustration of aligning F8BT by nanoconfinement. (b-e) SEM images of Si mold (b, c) and nanoimprinted F8BT using Si mold (d, e). (f) Polarized absorption spectra of aligned F8BT parallel (//) and perpendicular (⊥) to the nanochannel array. The inset shows absorption peak intensity at different angle of polarization.[55] (Reproduced with permission, copyright 2007 American Chemical Society).

of nanochannel arrays.[55] The green-emitting F8BT was spincast onto a substrate, and imprinted with the mold at 160 ^{o}C and 40 bar for 5 min (**Figure 1.13a**). The scanning electron microscopy (SEM) images of the mold and the imprinted F8BT are presented in **Figure 1.13**, **b-e**. The imprinted CP film showed nanochannel arrays identical to those present in the mold, and exhibited clear optical anisotropy with an observed absorption dichroic ratio of 7 (**Figure 1.13f**). In this procedure, the self-organization of CP chains in the LC phase was thought to be similar to the LC alignment on a rubbed polyimide film, which was suggested to be a possible alignment mechanism. The structural factor of the imprinted CP film was revealed to be irrelevant to the

observed anisotropic optical property as imprinted amorphous films of poly(2,7-(9,9-di-n-octylfluorene)-alt-(1,4-phenylene-((4-sec-butylphenyl)imino)-1,4-phenylene)) did not exhibit any optical anisotropy even though the same nanochannel pattern was produced by nanoimprinting with the same silicon mold.[55]

Regulation of CP assembly inside of nanopillars or nanogratings was also demonstrated by means of nanoimprinting.[56,57] Hu *et al.* reported vertical chain alignment of rrP3HT in both nanogratings and nanopillars fabricated by nanoimprinting at 170 ^{o}C.[56] In addition, Hu *et al.* controlled face-on and edge-on orientation of rrP3HT chains via solvent-assisted room temperature nanoimprint lithography.[57] Differing from the general nanoimprinting process conducted at a temperature above the glass transition temperature (T_g) of the CP, this process was applied at room temperature on a still wet polymer film immediately after film fabrication but before the solvent completely dried out. Interestingly, the orientation of rrP3HT in the nanopillars was determined by the critical diameter of the nanopillar; face-on orientation was dominant when the nanopillars had a diameter less than 85 nm while edge-on orientation was dominant when the nanopillars had a diameter greater than 85 nm.[57]

1.3.2.4. Pre-Patterned Substrate

The substrate is one of the important factors that critically affects CP alignment. As described above, mechanically rubbed polyimide layers are widely used as a substrate for liquid crystal and LC CP alignment. Sirringhaus *et al.* reported alignment of a thermotropic LC CP, poly(9,9'-dioctyl-fluorene-*co*-bithiophene) (F8T2), on a rubbed polyimide alignment layer.[58] The aligned F8T2 was prepared by spin casting F8T2 onto a polyimide alignment layer, followed by

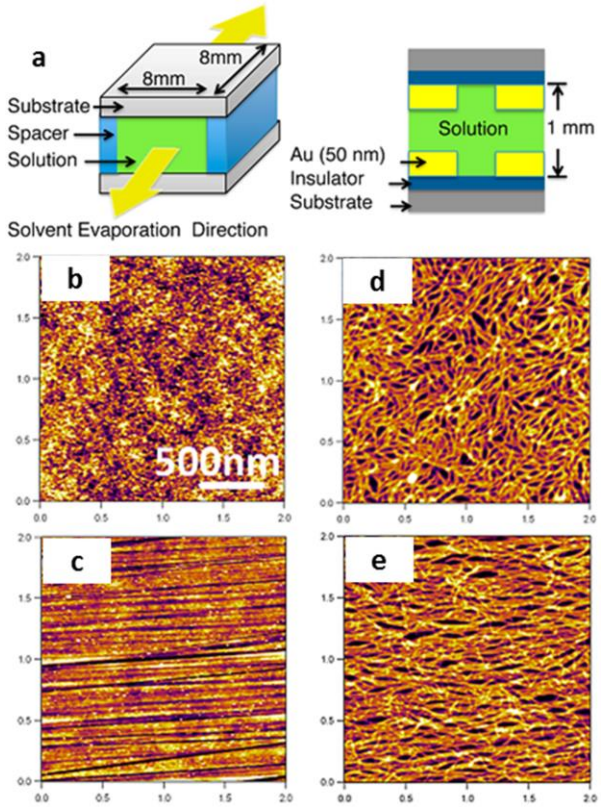

Figure 1.14 CPs' alignment on pre-patterned substrate. (a) Schematic illustration of solvent evaporation setup with cross-sectional illustration. (b-e) AFM images of dielectric substrate (b,c) and PCDTPT fiber morphology (d,e). (b) Surface without structures, (c) 100 nm-structured (scratched) surface, (d) polymer fibers on non-structured surface, (e) polymer fibers on 100 nm-structured (scratched) surface.[59] (Reproduced with permission, copyright 2012 American Chemical Society).

annealing at the temperature of the thermotropic LC phase (275~285 ^{o}C). The film was then quenched to room temperature to preserve the obtained alignment and to suppress crystallization. The resulting nematic CP glass exhibited dichroic ratio of 5~12 depending on the thickness of films, annealing condition of F8T2, and the rubbing procedure of polyimide.[58]

More recently, researchers at the University of California-Santa Barbara reported a CP alignment method using a nanogrooved substrate.[59–61] To make the nanogrooved substrate, a silicon wafer was scratched with a diamond lapping film (**Figure 1.14**, **b** and **c**). By applying the nanogrooved substrate and controlling the solvent evaporation direction and speed (**Figure 1.14a**), nanofibers of poly[4-(4,4-dihexadecyl-4H-cyclopenta[1,2-b:5,4-b′]-dithiophen-2-yl)-*alt*-[1,2,5]thiadiazolo [3,4-*c*]pyridine] (PCDTPT) were fabricated and ordered parallel to the nanogroove direction (**Figure 1.14**, **d** and **e**).[59] The aligned PCDTPT nanofibers exhibited anisotropic optical properties, dichroic ratio of ca. 2, as well as anisotropic charge mobility; 6

times higher hole mobility was observed in the parallel to the alignment direction compared to the perpendicular to the alignment direction.

1.3.2.5. Matrix Assisted Alignment

Matrix assisted alignment of CP chains has been actively investigated. Because of their useful 1-D pore structure, porous silica[62–64] and anodized aluminum oxide (AAO)[65] have been used as a matrix or a template for directional CP alignment. CP chains have also been embedded in a polymer matrix followed by uniaxial tensile drawing,[66,67] and blended into aligned LC molecules[68] that result in directed CP alignment.

Tolbert and coworkers utilized hexagonal honeycomb structured porous silica to confine CP chains inside nanopores.[62–64] The silica framework was synthesized by co-assembly of silica precursors and organic surfactants via LC intermediate, followed by chemical cross-linking of the silica.[62] By facilitating growth on a rubbed polyimide substrate, the 1-D pores of the silica framework are aligned parallel to the substrate.[63,64] Poly(2-methoxy-5-(2'-ethyl-hexyloxy)-1,4-phenylenevinylene) (MEH-PPV) solution was applied on the hydrophobized surface of the silica framework to fill the pores at an elevated temperature. The MEH-PPV that aligned inside the silica nanopores exhibited dichroic ratio of 5~6 in absorption.[63,64] **Figure 1.15** presents the anisotropic absorption properties under polarized light both vertical and parallel to the pore direction and the image of the nanoporous silica together with a schematic illustration of the aligned CPs in the silica nanochannels.

Recently, Iacopino *et al.* reported highly aligned poly(9,9-dioctylfluorene) (PFO) nanofibers fabricated using AAO as a template.[65] In this process, PFO nanofibers were prepared by solution

wicking through AAO membranes (pore diameter 25 nm) and collected after dissolving AAO membranes by aqueous NaOH. Because of the alignment of PFO chains during pore infiltration, the obtained PFO nanofibers have a highly anisotropic emission property. The PL intensity dichroic ratio is 15, implying that CP chains are aligned in the direction of the pores by the flow field generated during the solution infiltration.[65]

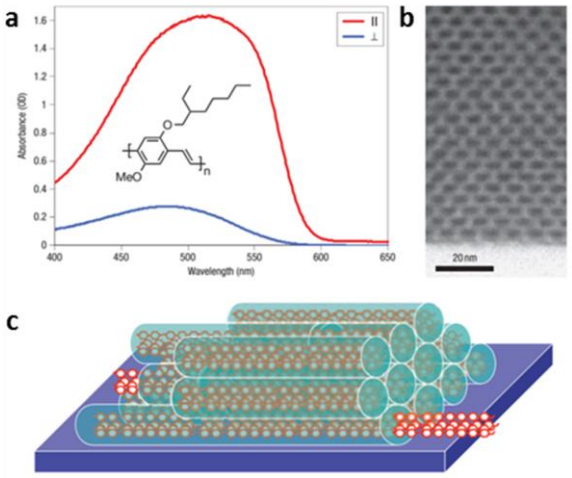

Figure 1.15 Porous silica assisted CP alignment. (a) Polarized absorption spectra of a MEH-PPV/aligned mesoporous silica composite film parallel (//) and perpendicular (⊥) to the pore direction. (b) TEM image of thin section of an aligned nanoporous silica film. (c) Schematic illustration of CP chains incorporation into the aligned nanoporous silica channels.[64] (Reproduced with permission, copyright 2007 Nature Publishing Group).

Tensile drawing of a host-guest system has also been demonstrated as an efficient CP alignment method. MEH-PPV[66] and poly(2,5-dialkoxy-*p*-phenyleneethynylene)s (OPPEs)[67] are utilized as guest materials embedded in an ultrahigh molecular weight polyethylene (UHMW-PE) matrix followed by uniaxial tensile deformation at a temperature above T_g of the incorporated CP and below the melting point (T_m) of host polymer. Heeger *et al.* reported the uniaxial tensile drawing of MEH-PPV in UHMW-PE matrix, which showed highly anisotropic properties in both absorption and emission.[66] MEH-PPV blend films were prepared as freestanding films and drawn at 110~120 ^oC to a draw ratio of 50 where the draw ratio is defined as the final length divided by initial length. An absorption dichroic ratio of ca. 5 was observed. Weder and coworkers utilized OPPEs as a guest CP in UHMW-PE matrix (**Figure 1.16a**).[67] A huge dichroic ratio of 72 was achieved in emission from a tensile drawn film of 2 wt% of EHO-OPPE (M_n=

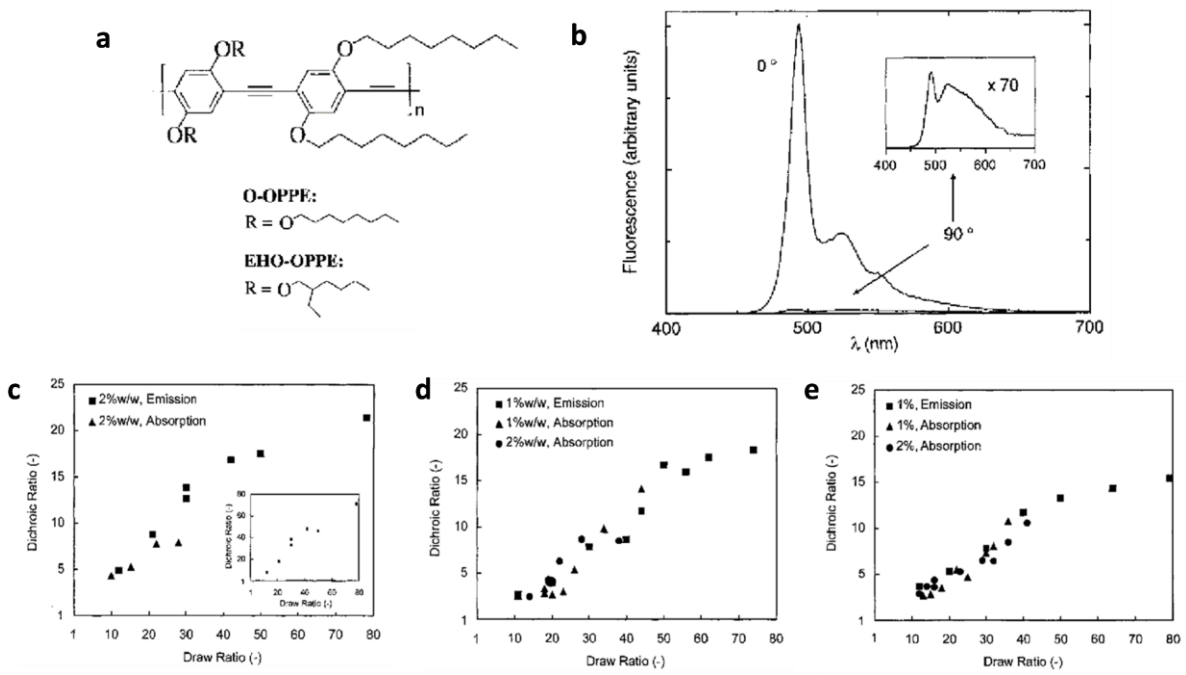

Figure 1.16 CPs alignment via uniaxial tensile drawing. (a) Chemical structure of OPPEs. (b) PL spectra of EHO-OPPE/UHMW-PE blend film recorded for emission parallel (0^o) and perpendicular (90^o) to the drawing direction. (c-e) Dichroic ratio (calculated from the integral of the respective spectra) as a function of draw ratio. (c) EHO-OPPE (M_n= 84,000 g·mol^{-1}) in UHMW-PE. Inset shows dichroic ratio calculated from PL intensity. (d) EHO-OPPE (M_n= 10,000 g·mol^{-1}) in UHMW-PE. (e) O-OPPE (M_n= 10,000 g·mol^{-1}) in UHMW-PE.[67] (Reproduced with permission, copyright 1997 WILEY-VCH Verlag GmbH & Co. KGaA, Weinheim).

84,000 g·mol^{-1}) in UHMW-PE (draw ratio = 80) (**Figure 1.16b**). Furthermore, the relationships between the degree of alignment (dichroic ratio calculated by the integral of the PL spectra), draw ratio, molecular weight of OPPE, and type of side chain were systematically investigated (**Figure 1.16**, **c-e**). As the draw ratio was increased, the dichroic ratio initially increased linearly before it plateaued at a draw ratio of ca. 50. When comparing EHO-OPPE having M_n of 10,000 g·mol^{-1} and 84,000 g·mol^{-1}, the larger molecular weight EHO-OPPE showed a higher alignment possibly due to the larger aspect ratio of CP chain (**Figure 1.16**, **c** and **d**). In addition, a branched side chain (EHO-OPPE) was suggested to be more favorable than a linear side chain (O-OPPE)

for CP alignment from tensile deformation of the host-guest polymer system (**Figure 1.16**, **d** and **e**).

LC molecules were also used as a host to align a guest CP. Swager *et al.* reported PPV and PPE derivatives aligned in nematic LC molecule, 1-(trans-4-hexylcyclohexyl)-4-isothiocyanatobenzene (6CHBT) (**Figure 1.17a**).[68] The CPs were dissolved in the LC molecule and loaded into a LC cell having a rubbed polyimide surface. The homogenous alignment of the LC molecules ensured CP chain alignment together with an increase in effective conjugation length as illustrated in the UV-vis absorption spectrum (**Figure 1.17**, **b** and **c**).

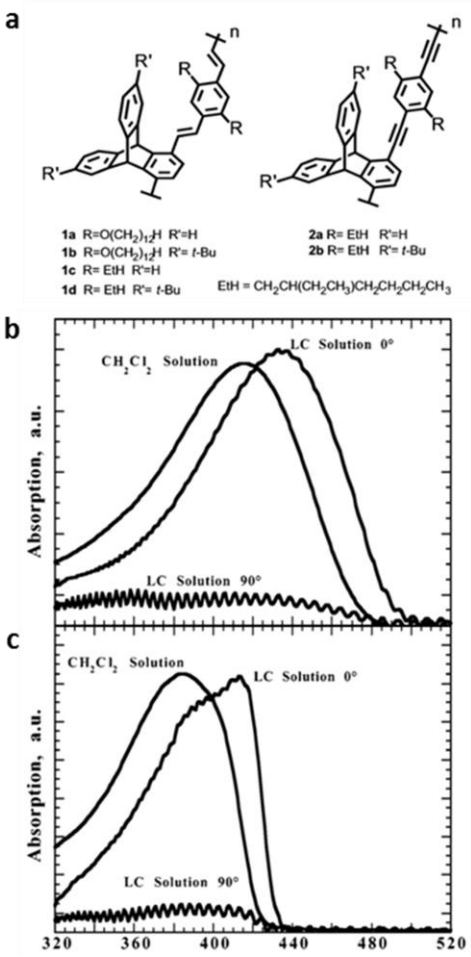

Figure 1.17 CP alignment induced by LC molecules. (a) Chemical structure of PPV and PPE derivatives. (b) Absorption spectra of 1d in methylene chloride and 6CHBT. (c) Absorption spectra of 2a in methylene chloride and 6CHBT. Alignment is clearly observed from the ratio of spectra taken at 0^{o} and 90^{o} to the nematic director.[68] (Reproduced with permission, copyright 2002 American Chemical Society).

1.3.2.6. Electrospinning

Alignment of electrospun nanofibers is another example of CP alignment. Generally, composite electrospun nanofibers containing CPs and spinnable polymers such as poly(methyl methacrylate) (PMMA)[69] and poly(ethylene oxide) (PEO)[70,71] are utilized for CP alignment. Chen *et al.* reported aligned eletrospun nanofibers from two types of polyfluorene/PMMA blends

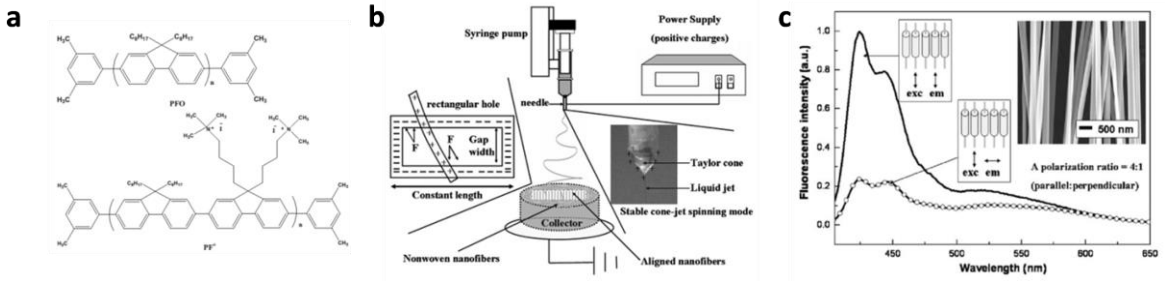

Figure 1.18 CPs alignment by electrospinning. (a) Chemical structures of the polyfluorene derivatives. (b) Schematic illustration for electrospinning setup to produce aligned nanofibers. (c) Polarized PL from PF+/PMMA nanofiber. The inset shows SEM images of aligned nanofibers.[69] (Reproduced with permission, copyright 2008 WILEY-VCH Verlag GmbH & Co. KGaA, Weinheim).

(**Figure 1.18a**).[69] A schematic representation of the electrospinning setup is illustrated in **Figure 1.18b**. The alignment of nanofibers spun from the syringe pump is ascribed to electrostatic force between the negatively charged collector gap edge and the positively charged nanofibers. In **Figure 1.18c**, PF+/PMMA nanofibers shows 1-directional orientation with optical anisotropy (dichroic ratio = 4 in PL). Murata *et al.* demonstrated alignment of electrospun nanofibers of MEH-PPV/PEO blend.[70] The anisotropic emission property was investigated from aligned electrospun nanofibers as well as nanofibers that were stretched after electrospinning. The initial dichroic ratio in emission was observed as ca. 13.3 but increased to ca. 25 after stretching three times.[70]

1.3.2.7. Directional Solidification

Directional solidification here refers to the polymer alignment driven by heterogeneous nucleation followed by epitaxial crystallization of polymers onto a crystalline surface of aromatic molecules.[72–76] Previously, epitaxial growth of PE onto aromatic crystals[72] and highly oriented

microdomain of polystyrene (PS)-*b*-PE block copolymer using benzoic acid as a solvent and nucleation site for polymer crystallization[73] have been demonstrated.

Brinkmann *et al.* reported directional solidification of CP on aromatic crystals.[74] In this method, 1,3,5-trichlorobenzene (TCB) was utilized as a solvent to crystallize rrP3HT. TCB powder was deposited on the drop cast rrP3HT film and heated until the TCB melts and dissolves the rrP3HT. Upon cooling the solution, the TCB crystallizes first and provides a foundation for the rrP3HT to nucleate and epitaxially crystallize. After the rrP3Ht was completely crystallized, the TCB was removed by slow evaporation under vacuum. This method provided a well-defined fibrous rrP3HT film with clear birefringence present under a crosspolarizer.[74]

In spite of efficient epitaxial crystallization of CP, this method suffers from a relatively complicated procedure, uncontrolled nucleation density, and only limited area of uniaxially aligned CP, all of which hamper efficient device application. Recently, directional solidification of spin casting and a blade coating method were developed using a mixed solvent system.[75,76] Müller *et al.* demonstrated a rather simplified method for directional solidification via spin casting using chlorobenzene (CB) and TCB as a mixed solvent for various CPs.[75] In this system, the concentration of TCB in CB was revealed to be an important factor in the epitaxial crystallization of rrP3HT as well as in controlling the nucleation density. If the solution contains less than 4 vol% of TCB in CB, the spincast film did not show directional crystallization. The maximum nucleation density for rrP3HT was observed at 7.5 vol% of TCB with ca. 4~5 nucleation points per square centimeter. The optical anisotropy of a directionally solidified rrP3HT film is presented in **Figure 1.19**, **a** and **b**. Furthermore, directional solidification of various CPs and CP:[6,6]-phenyl-C_{61}-butyric acid methyl ester ($PC_{61}BM$) blends was

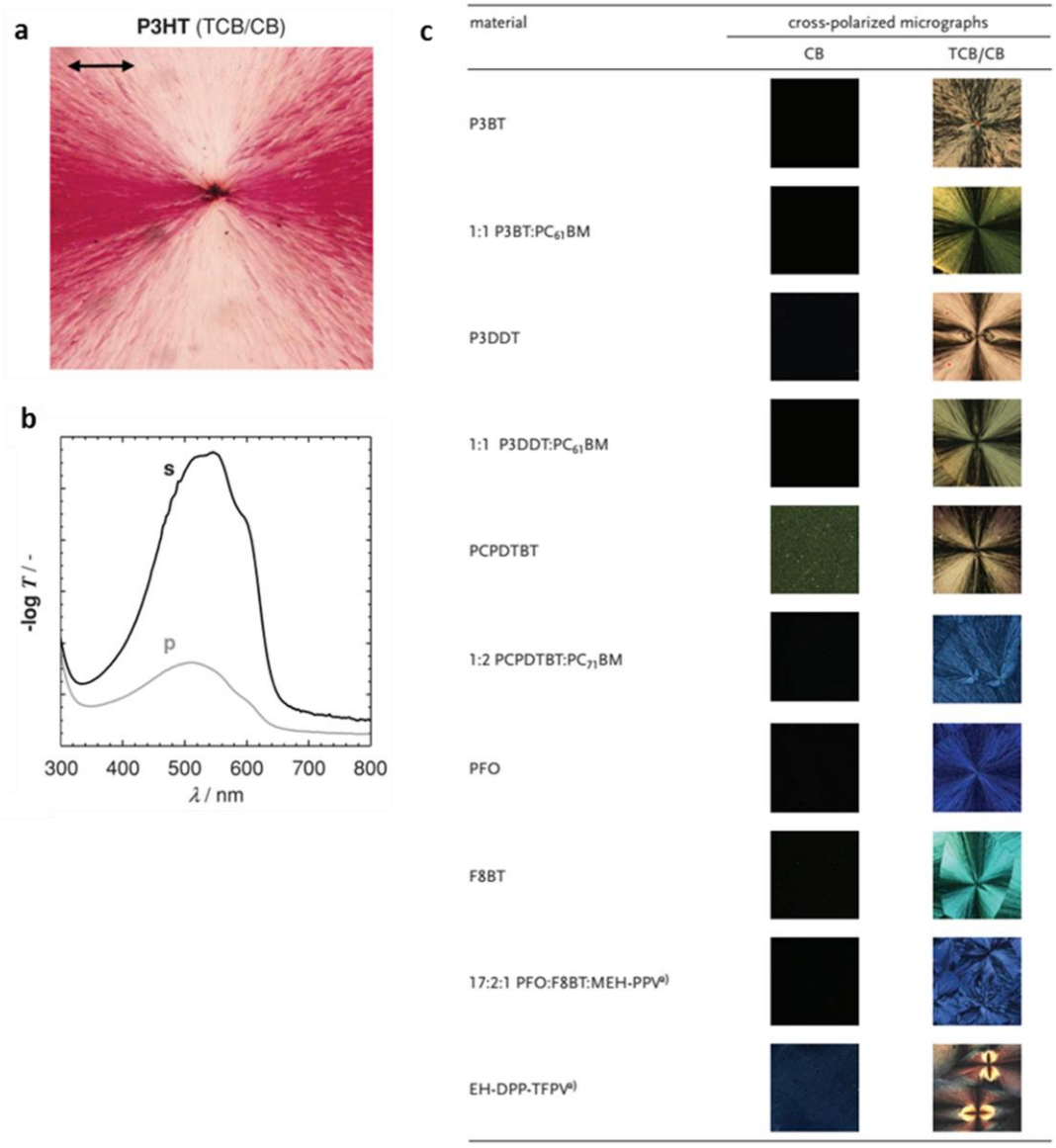

Figure 1.19 CPs alignment through directional solidification done by spin casting. (a) Polarized optical micrograph under single polarizer (black arrow) of spincasted P3HT from TCB (7.5 vol%)/CB mixed solvent. (b) Polarized photometry measurements at a horizontal distance of 1 mm from a spherulite structure center. (s-polarization horizontal, p-polarization vertical). (c) Cross-polarized micrographs of various CPs films fabricated by spin casting from CB or TCB/CB ([a)]spin casted from chloroform and TCB/chloroform).[75] (Reproduced with permission, copyright 2013 WILEY-VCH Verlag GmbH & Co. KGaA, Weinheim).

demonstrated using spin casting of a mixed solution (**Figure 1.19c**). The control of nucleation behavior in directional solidification was further investigated using a blade coating of CB/TCB mixed solvent for rrP3HT.[76] By controlling the blade speed under a specific ratio of the

incorporated materials, the solvent drying character could be controlled, which enabled epitaxially crystallized CP films to be produced across several square centimeters. The CP crystallization induced by TCB crystals occurs randomly through the entire film when blade stroke is fast; however, if blade stroke is slow enough (1~2 mm·s^{-1}), TCB nucleation is confined at the edge of the blade so that uniaxially crystallized CP films are grown over the whole area (**Figure 1.20**). A dichroic ratio of 3~4 was observed throughout the directionally solidified

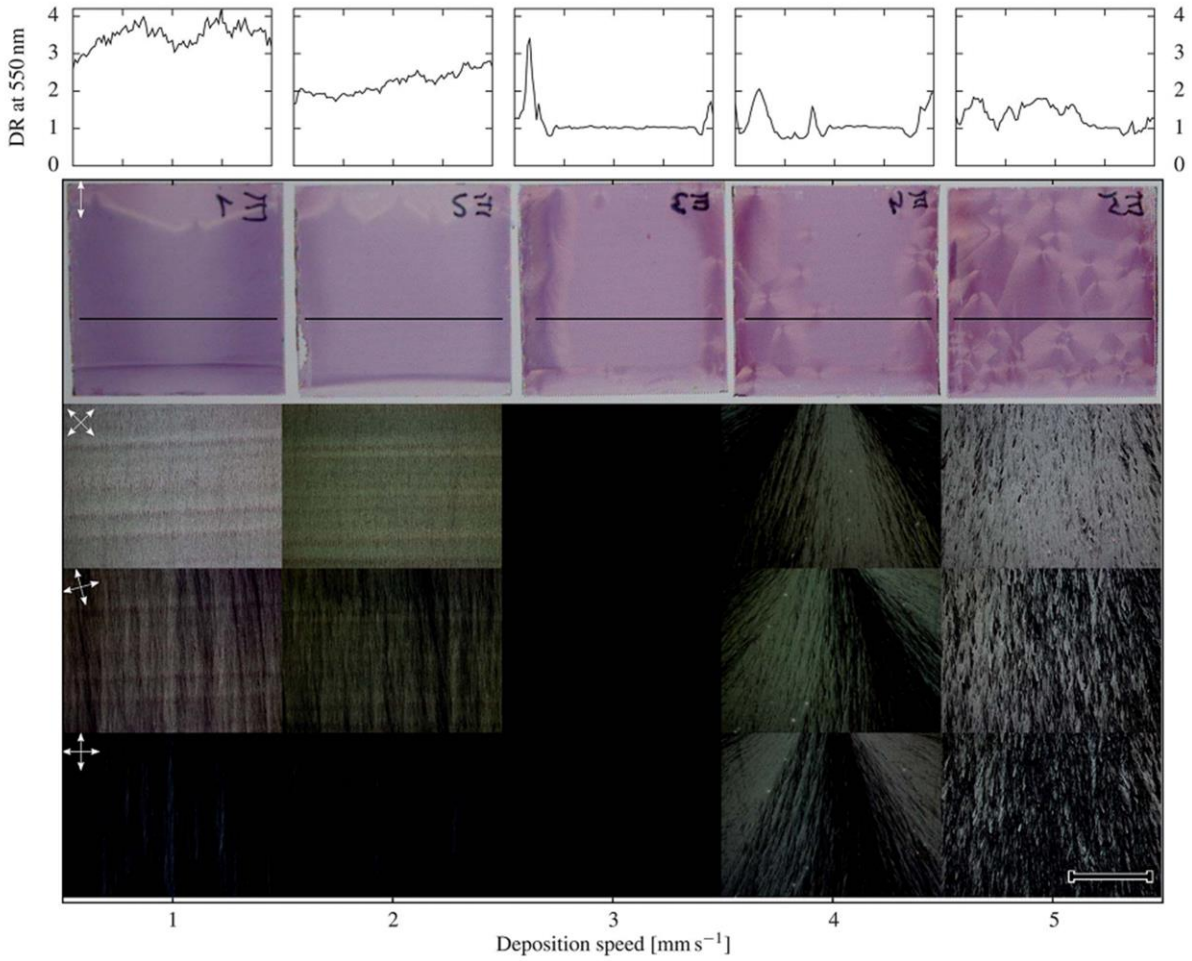

Figure 1.20 CP alignment through directional solidification done by blade coating. Polarized transmission images and cross-polarized micrographs of P3HT film deposited by different deposition speed under blade coating (solution: 20 mg·ml^{-1} P3HT and m_{TCB}/m_{P3HT}= 5). Dichroic ratio (DR) was measured at 550 nm. Scale bar= 500 μm.[76] (Reproduced with permission, copyright 2014 The Royal Society of Chemistry).

rrP3HT film fabricated by blade coating with CB solution containing TCB and rrP3HT (mass ratio 5:1) at the blade speed of 1 mm·s^{-1} (**Figure 1.20**).

1.3.2.8. CP Design for Directed Alignment

Certain degree of CP alignment has been achieved by developing processes that help to align the CPs so that they exhibit high anisotropic optical and electronic properties. However, the development of CP alignment methods without considering material design aspects cannot fully address this challenging issue. It is still unknown as to why some CPs can be aligned easily while others have much larger difficulties, and what causes the differences in the degree of alignment even when the same alignment strategies are applied. Investigation into the molecular design aspects for directed assembly and alignment of CPs has recently emerged.

Our research group recently reported a CP design principle for directed alignment.[37] The synthesized CP, CP1, is designed to have a lyotropic LC phase (**Figure 1.21a**). Drop casting CP1 solution on a flat substrate showed distinctive alignment along the direction of the flow field generated by solvent evaporation. This is a very interesting phenomenon as the alignment from drop casting implies that CP1 has an intrinsic propensity for alignment without the aid of any specific alignment strategies. A systematic investigation was conducted on the molecular design features essential for this alignment tendency of CP1. From the characterization of CP1 and three different control CPs with modified chemical structures, it was revealed that three molecular design features are essential for directed alignment of CPs: (1) a concentration-induced chain planarization unit together with (2) a bulky side chain on a (3) out-of-plane tetrahedral carbon linker (**Figure 1.21a**).

For a macroscopic alignment, CP chains should not form massive aggregations in the solution state, but should initiate gradual interchain interactions as the solvent evaporates. In a highly concentrated solution, the CP chains should form a lyotropic LC phase in which the CPs are still mobile so that they can be aligned along the direction of any shear flow due to the large aspect ratio of the CP chains. Applying a contact coating on a lyotropic LC CP, such as CP1, caused directed self-assembly and alignment of the CPs (**Figure 1.21**, **b** and **c**). During the contact coating, the three design requisites regulated the self-assembly of CP1 as follows (**Figure 1.21d**). The twisted phenyl ring of the main chain and the bulky side chain attached in an out-of-

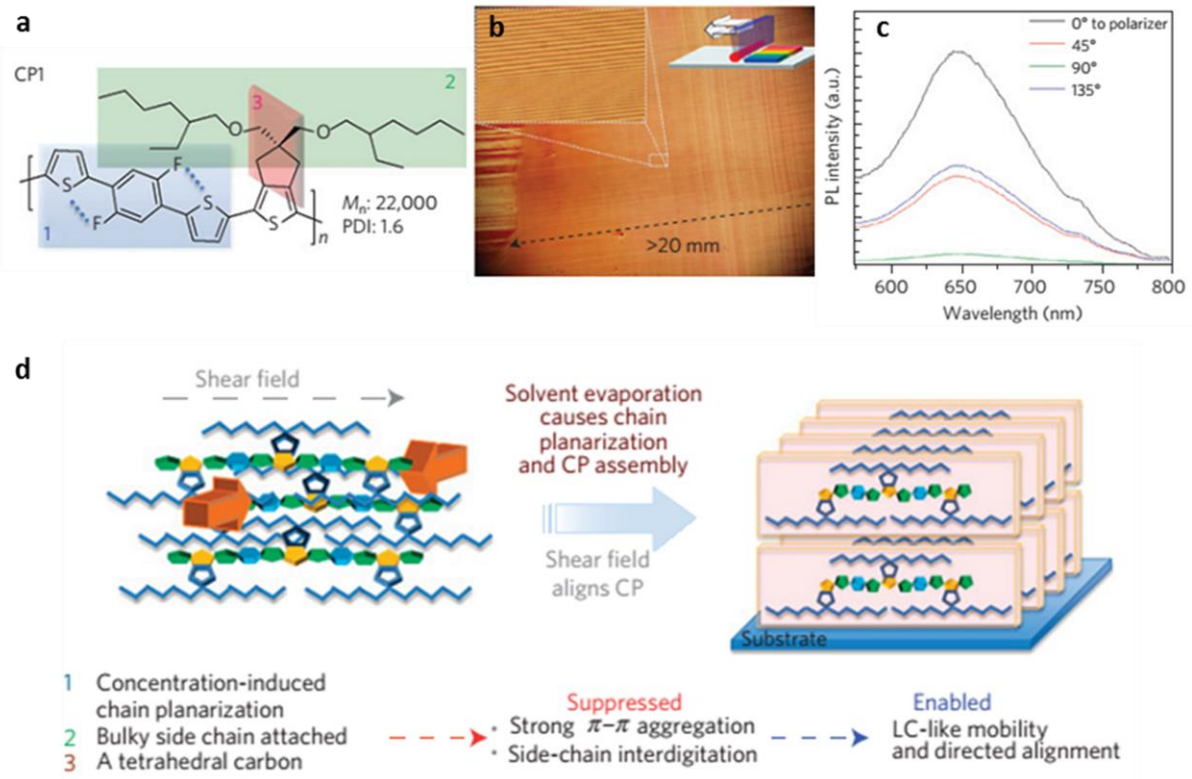

Figure 1.21 CP design for directed alignment. (a) Chemical structure of CP1 and three design requirements for directed alignment under shear flow. (b) Optical micrograph of an aligned CP1 film fabricated by contact coating (inset). (c) Emission spectra of aligned CP1 film through a linear polarizer (0^o= parallel to the alignment direction, 90^o= perpendicular to the alignment direction). (d) The suggested mechanism of CP1 alignment.[37] (Reproduced with permission, copyright 2013 Macmillan Publishers Limited).

plane configuration efficiently prevented massive aggregation of CP1 in the solution state. As the solvent evaporated throughout the contact coating process, the solution concentration steadily increases, which forces the CPs to be packed increasingly closer together. This increasing proximity causes the CPs to undergo a conformational change and a reorientation to reduce their steric hindrance. During the conformational change, the phenyl rotation triggers an intramolecular S-F interaction, resulting in a planar conformation of the CP1 main chain. The planarized main chains promote inter-chain assembly via π-π interaction. However, the bulky side chains attached on the out-of-plane tetrahedral carbon suppress massive aggregation, which causes the mobile lyotropic LC nature of the CP1 chains and results in macroscopic alignment to the direction of the flow field.[37]

Contact coating of CP1 solution on a Si substrate at 140 ^{o}C (gap 50 μm, blade speed 25 $\mu m \cdot s^{-1}$) produced an aligned CP1 film having highly anisotropic optical characteristic (dichroic ratio of 16.67 in emission) over a cm-scale area (**Figure 1.21**, **b** and **c**).[37] The alignment effect on the charge carrier mobility was tremendous. The aligned CP1 film exhibited ca. 1,600 times higher hole mobility parallel to the alignment direction ($\mu_h = 0.86\ cm^2 \cdot V^{-1} \cdot s^{-1}$) than the perpendicular to the alignment direction ($\mu_h = 0.00054\ cm^2 \cdot V^{-1} \cdot s^{-1}$).[37] The structural analysis of the aligned CP1 film, characterized by grazing-incidence X-ray diffraction equipped with a 2-D detector (2D GIXRD), revealed edge-on oriented lamellar packing of CP1 main chain aligned in parallel along the shear-flow direction.

1.4. Design of Organic Materials with Unique Supramolecular Assembly

In summary, to realize optimal properties of conjugated organic materials for various optoelectronic applications, it is critically important from the material designing step to consider

both intrinsic intramolecular properties that are mainly determined by the conjugated chemical structure of conjugated small molecules or polymers, and intermolecular properties, controlled by intermolecular interactions and molecular packing. Even though it is difficult to fully predict the whole properties of conjugated organic materials, a systematic investigation for the relationship between the chemical structure of organic conjugated materials and their properties will enable us to build valuable insight on the design of high performance organic conjugated materials. In this dissertation work, systematic and comprehensive investigations on the correlation between structural parameters and intrinsic intramolecular properties as well as intermolecular packing properties, which eventually determine the resulting properties in unique

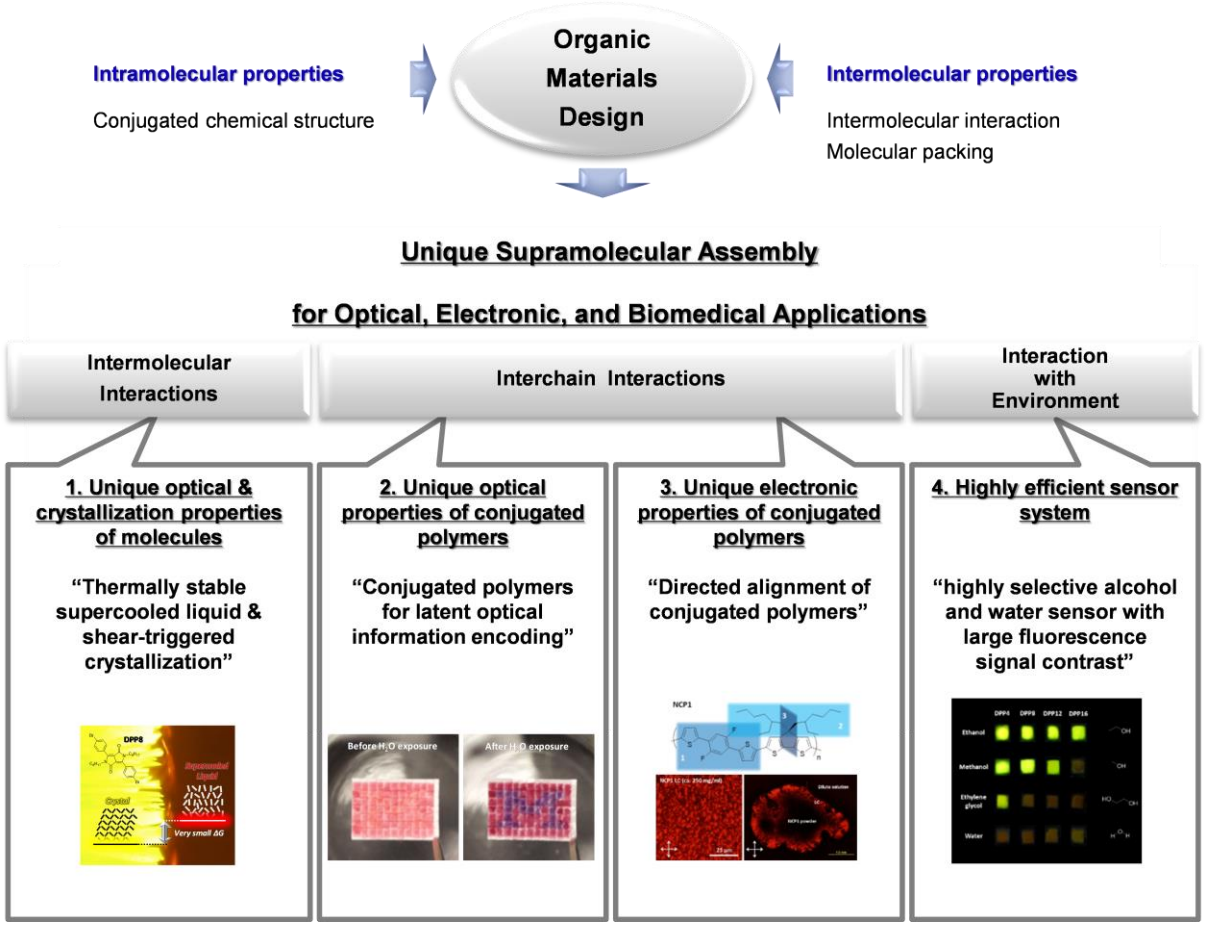

Figure 1.22 Schematic representation of the research in this dissertation.

organic conjugated molecular and polymer systems in the solid state, are demonstrated (**Figure 1.22**). Insightful material design considering both intramolecular and intermolecular properties of the conjugated organic material enables distinct optoelectronic properties through predictable supramolecular assembly for various applications such as optical, electronic, and biomedical applications.

In Chapter 2, through the intermolecular interaction control by molecular design, unique thermally stable supercooled liquid and its shear-triggered lighting-up crystallization are presented (**Figure 1.22**). Thermodynamics drive crystalline organic molecules to be crystallized at temperatures below their melting point. Even though molecules can form supercooled liquids by rapid cooling, crystalline organic materials readily undergo a phase transformation to an energetically favorable crystalline phase upon subsequent heat treatment. Opposite to this general observation, in Chapter 2, a molecular design of thermally stable supercooled liquid of diketopyrrolopyrrole (DPP) derivatives and their intriguing shear-triggered crystallization with dramatic optical property changes are presented. Molten DPP8, one of the DPP derivatives, remains as stable supercooled liquid without crystallization through subsequent thermal cycles. More interestingly, under shear condition, this supercooled liquid DPP8 transforms to its crystal phase accompanied by a 25-fold increase in photoluminescence (PL) quantum efficiency and a color change. By systematic investigation on supercooled liquid formation of crystalline DPP derivatives and their correlation with chemical structures, it is revealed that the origin of this thermally stable supercooled liquid is a subtle force balance between aromatic interactions among the core units and van der Waals interactions among the aliphatic side chains acting in opposite directions. Moreover, by applying shear force to a supercooled liquid DPP8 film at different temperatures, direct writing of fluorescent patterns and propagating fluorescence

amplification are demonstrated. Shear-triggered crystallization of DPP8 is further achieved even by living cell attachment and spreading, demonstrating the high sensitivity of the shear-triggered crystallization which is about six orders of magnitude more sensitive than typical mechanochromism observed in organic materials.[77]

Chapter 3 presents a unique latent optical information encoding application of CPs as security inks by means of their distinct optical properties through controlling intrachain and interchain properties (**Figure 1.22**). To date, most CP designs have focused on the conjugated main chain to control the intrachain properties, while the design of side chains is usually used to render CPs soluble, even though the side chains critically affect the interchain packing. In Chapter 3, a straightforward and effective design strategy is presented for modifying the optical and electrochemical properties of diketopyrrolopyrrole-based CPs by controlling both the intrachain and interchain properties in a single system. The synthesized polymers, P1, P2 and P3, show almost identical optical absorption spectra in solution, manifesting essentially the same intrachain properties of the three CPs having restricted effective conjugation along the main chain. However, the absorption spectra of CP films are gradually tuned by controlling the interchain packing through the side-chain design. Based on the tailored optical properties, encoding of latent optical information is demonstrated utilizing the CPs as security inks on a silica substrate, which reveals and conceals hidden information upon the reversible aggregation/deaggregation of CPs.[78]

Furthermore, in Chapter 4, CP design principles are thoroughly expanded and validated to realize directed alignment that are critically impact for the electronic application of CPs (**Figure 1.22**). Alignment of conjugated polymers (CPs) is essential to fully realize the anisotropic optical and electronic properties of CPs, originated from the one-dimensional p-orbital overlap along the

conjugated backbone. To realize polymer alignment, many CP processing approaches have been investigated. However, molecular origin to enable CP alignment has not been fully understood. In this chapter, universal applicability of the previous identified molecular design rules for directed CP alignment is examined. For that purpose a new series of CPs are designed by adapting the preliminary design principles with different building blocks. Moreover, additional design factors that have determinant effects on CP alignment characteristics, including structural factor of side chains, concentration-induced planarization unit, and surface free energy and wettability are discussed.

The characteristics of organic conjugated materials can also be influenced by environment of the molecules, such as applied substrate and surrounding solvent molecules. In Chapter 5, the interaction of conjugated organic molecule with its environment is investigated, and applied to the development of a highly selected alcohol and water sensor system based on the devised subtle difference in interactions between a series of sensory conjugated molecules, mesoporous silica substrates, and various alcohols and water molecules (**Figure 1.22**). When fluorescent organic molecules are dispersed onto a mesoporous silica substrate, they exhibit bright green fluorescence. However, upon exposure to highly polar (and/or hydrogen-bonding favorable) solvents, the fluorescence of the organic molecules on the silica substrate undergoes significant color change as well as emission intensity quenching. The characteristics of the fluorescence change, as a readable optical sensory signal, can be precisely controlled by molecular design of the fluorophores. A prototype sensor kit, composed of multiple fluorescent molecules having different thresholds of fluorescence signal change upon solvent exposure, is demonstrated as a new type of sensor system with a large fluorescence signal contrast and a high selectivity among physicochemically similar solvents; ethanol, methanol, ethylene glycol, and water.

1.5. References and Notes

1. H. Shirakawa, E. J. Louis, A. G. MacDiarmid, C. K. Chiang, A. J. Heeger, Synthesis of electrically conducting organic polymers: halogen derivatives of polyacetylene, (CH) x. *J. Chem. Soc. Chem. Commun.* 578-580 (1977).
2. M. Gross, D. Muller, H. Nothofer, U. Scherf, D. Neher, C. Brauchle, K. Meerholz, Improving the performance of doped pi-conjugated polymers for use in organic light-emitting diodes. *Nature* **405,** 661–665 (2000).
3. B. R. Lee, E. D. Jung, J. S. Park, Y. S. Nam, S. H. Min, B.-S. Kim, K.-M. Lee, J.-R. Jeong, R. H. Friend, J.-S. Kim, S. O. Kim, M. H. Song, Highly efficient inverted polymer light-emitting diodes using surface modifications of ZnO layer. *Nat. Commun.* **5,** 4840 (2014).
4. S. H. Lim, L. Feng, J. W. Kemling, C. J. Musto, K. S. Suslick, An optoelectronic nose for the detection of toxic gases. *Nat. Chem.* **1,** 562–567 (2009).
5. M. S. Kwon, J. H. Jordahl, A. W. Phillips, K. Chung, S. Lee, J. Gierschner, J. Lahann, J. Kim, Multi-luminescent switching of metal-free organic phosphors for luminometric detection of organic solvents. *Chem. Sci.* **7,** 2359–2363 (2016).
6. I. McCulloch, M. Heeney, C. Bailey, K. Genevicius, I. Macdonald, M. Shkunov, D. Sparrowe, S. Tierney, R. Wagner, W. Zhang, M. L. Chabinyc, R. J. Kline, M. D. McGehee, M. F. Toney, Liquid-crystalline semiconducting polymers with high charge-carrier mobility. *Nat. Mater.* **5,** 328–333 (2006).
7. H. Sirringhaus, P. J. Brown, R. H. Friend, M. M. Nielsen, K. Bechgaard, B. M. W. Langeveld-Voss, A. J. H. Spiering, R. A. J. Janssen, E. W. Meijer, P. Herwig, D. M. de Leeuw, Two-dimensional charge transport in self-organized, high-mobility conjugated polymers. *Nature* **401,** 685–688 (1999).
8. Y. Kim, S. Cook, S. M. Tuladhar, S. A. Choulis, J. Nelson, J. R. Durrant, D. D. C. Bradley, M. Giles, I. McCulloch, C.-S. Ha, M. Ree, A strong regioregularity effect in self-organizing conjugated polymer films and high-efficiency polythiophene:fullerene solar cells. *Nat. Mater.* **5,** 197–203 (2006).
9. H.-Y. Chen, J. Hou, S. Zhang, Y. Liang, G. Yang, Y. Yang, L. Yu, Y. Wu, G. Li, Polymer solar cells with enhanced open-circuit voltage and efficiency. *Nat. Photonics* **3,** 649–653 (2009).
10. S. H. Park, A. Roy, S. Beaupré, S. Cho, N. Coates, J. S. Moon, D. Moses, M. Leclerc, K. Lee, A. J. Heeger, Bulk heterojunction solar cells with internal quantum efficiency approaching 100%. *Nat. Photonics* **3,** 297–302 (2009).
11. O. Bubnova, Z. U. Khan, A. Malti, S. Braun, M. Fahlman, M. Berggren, X. Crispin, Optimization of the thermoelectric figure of merit in the conducting polymer poly(3,4-ethylenedioxythiophene). *Nat. Mater.* **10,** 429–433 (2011).
12. G.-H. Kim, L. Shao, K. Zhang, K. P. Pipe, Engineered doping of organic semiconductors for enhanced thermoelectric efficiency. *Nat. Mater.* **12,** 719–723 (2013).
13. J. Kim, D. T. McQuade, S. K. McHugh, T. M. Swager, Ion-Specific Aggregation in Conjugated Polymers: Highly Sensitive and Selective Fluorescent Ion Chemosensors. *Angew. Chemie* **112,** 4026–4030 (2000).
14. J. Lee, H. Jun, J. Kim, Polydiacetylene-Liposome Microarrays for Selective and Sensitive Mercury(II) Detection. *Adv. Mater.* **21,** 3674–3677 (2009).
15. H.-A. Ho, M. Boissinot, M. G. Bergeron, G. Corbeil, K. Doré, D. Boudreau, M. Leclerc,

Colorimetric and Fluorometric Detection of Nucleic Acids Using Cationic Polythiophene Derivatives. *Angew. Chemie Int. Ed.* **41,** 1548–1551 (2002).
16. M. Remmers, B. Müller, K. Martin, H.-J. Räder, W. Köhler, Poly(p -phenylene)s. Synthesis, Optical Properties, and Quantitative Analysis with HPLC and MALDI−TOF Mass Spectrometry. *Macromolecules* **32,** 1073–1079 (1999).
17. D. Neher, Polyfluorene Homopolymers: Conjugated Liquid-Crystalline Polymers for Bright Blue Emission and Polarized Electroluminescence. *Macromol. Rapid Commun.* **22,** 1365–1385 (2001).
18. V. Cimrová, M. Remmers, D. Neher, G. Wegner, Polarized light emission from LEDs prepared by the Langmuir-Blodgett technique. *Adv. Mater.* **8,** 146–149 (1996).
19. N. Banerji, S. Cowan, E. Vauthey, A. J. Heeger, Ultrafast Relaxation of the Poly(3-hexylthiophene) Emission Spectrum. *J. Phys. Chem. C* **115,** 9726–9739 (2011).
20. P. Chawla, S. Singh, S. N. Sharma, An insight into the mechanism of charge-transfer of hybrid polymer:ternary/quaternary chalcopyrite colloidal nanocrystals. *Beilstein J. Nanotechnol.* **5,** 1235–1244 (2014).
21. E. Bundgaard, F. Krebs, Low band gap polymers for organic photovoltaics. *Sol. Energy Mater. Sol. Cells* **91,** 954–985 (2007).
22. H. A. M. van Mullekom, J. A. J. M. Vekemans, E. W. Meijer, Band-Gap Engineering of Donor-Acceptor-Substituted π-Conjugated Polymers. *Chem. - A Eur. J.* **4,** 1235–1243 (1998).
23. B.-G. Kim, X. Ma, C. Chen, Y. Ie, E. W. Coir, H. Hashemi, Y. Aso, P. F. Green, J. Kieffer, J. Kim, Energy Level Modulation of HOMO, LUMO, and Band-Gap in Conjugated Polymers for Organic Photovoltaic Applications. *Adv. Funct. Mater.* **23,** 439–445 (2013).
24. L. Huo, J. Hou, H.-Y. Chen, S. Zhang, Y. Jiang, T. L. Chen, Y. Yang, Bandgap and Molecular Level Control of the Low-Bandgap Polymers Based on 3,6-Dithiophen-2-yl-2,5-dihydropyrrolo[3,4- c]pyrrole-1,4-dione toward Highly Efficient Polymer Solar Cells. *Macromolecules* **42,** 6564–6571 (2009).
25. T. Xu, L. Yu, How to design low bandgap polymers for highly efficient organic solar cells. *Mater. Today* **17,** 11–15 (2014).
26. H. J. Son, W. Wang, T. Xu, Y. Liang, Y. Wu, G. Li, L. Yu, Synthesis of fluorinated polythienothiophene-co-benzodithiophenes and effect of fluorination on the photovoltaic properties. *J. Am. Chem. Soc.* **133,** 1885–1894 (2011).
27. S. Albrecht, S. Janietz, W. Schindler, J. Frisch, J. Kurpiers, J. Kniepert, S. Inal, P. Pingel, K. Fostiropoulos, N. Koch, D. Neher, Fluorinated copolymer PCPDTBT with enhanced open-circuit voltage and reduced recombination for highly efficient polymer solar cells. *J. Am. Chem. Soc.* **134,** 14932–14944 (2012).
28. Y. Liang, D. Feng, Y. Wu, S.-T. Tsai, G. Li, C. Ray, L. Yu, Highly efficient solar cell polymers developed via fine-tuning of structural and electronic properties. *J. Am. Chem. Soc.* **131,** 7792–7799 (2009).
29. L. Huo, S. Zhang, X. Guo, F. Xu, Y. Li, J. Hou, Replacing alkoxy groups with alkylthienyl groups: a feasible approach to improve the properties of photovoltaic polymers. *Angew. Chem. Int. Ed. Engl.* **50,** 9697–9702 (2011).
30. J. S. Ha, K. H. Kim, D. H. Choi, 2,5-Bis(2-octyldodecyl)pyrrolo[3,4-c]pyrrole-1,4-(2H,5H)-dione-based donor-acceptor alternating copolymer bearing 5,5’-di(thiophen-2-

yl)-2,2'-biselenophene exhibiting 1.5 cm2·V(-1)·s(-1) hole mobility in thin-film transistors. *J. Am. Chem. Soc.* **133,** 10364–10367 (2011).
31. A. J. Kronemeijer, E. Gili, M. Shahid, J. Rivnay, A. Salleo, M. Heeney, H. Sirringhaus, A selenophene-based low-bandgap donor-acceptor polymer leading to fast ambipolar logic. *Adv. Mater.* **24,** 1558–1565 (2012).
32. H.-Y. Chen, J. Hou, A. E. Hayden, H. Yang, K. N. Houk, Y. Yang, Silicon atom substitution enhances interchain packing in a thiophene-based polymer system. *Adv. Mater.* **22,** 371–375 (2010).
33. E. Wang, L. Wang, L. Lan, C. Luo, W. Zhuang, J. Peng, Y. Cao, High-performance polymer heterojunction solar cells of a polysilafluorene derivative. *Appl. Phys. Lett.* **92,** 033307 (2008).
34. J. Hou, H.-Y. Chen, S. Zhang, G. Li, Y. Yang, Synthesis, characterization, and photovoltaic properties of a low band gap polymer based on silole-containing polythiophenes and 2,1,3-benzothiadiazole. *J. Am. Chem. Soc.* **130,** 16144–16145 (2008).
35. C. M. Amb, S. Chen, K. R. Graham, J. Subbiah, C. E. Small, F. So, J. R. Reynolds, Dithienogermole as a fused electron donor in bulk heterojunction solar cells. *J. Am. Chem. Soc.* **133,** 10062–10065 (2011).
36. V. López-Mejías, A. J. Matzger, Structure–Polymorphism Study of Fenamates: Toward Developing an Understanding of the Polymorphophore. *Cryst. Growth Des.* **15,** 3955–3962 (2015).
37. B.-G. Kim, E. J. Jeong, J. W. Chung, S. Seo, B. Koo, J. Kim, A molecular design principle of lyotropic liquid-crystalline conjugated polymers with directed alignment capability for plastic electronics. *Nat. Mater.* **12,** 659–664 (2013).
38. J.-P. Brog, C.-L. Chanez, A. Crochet, K. M. Fromm, Polymorphism, what it is and how to identify it: a systematic review. *RSC Adv.* **3,** 16905 (2013).
39. L. Yu, Polymorphism in molecular solids: an extraordinary system of red, orange, and yellow crystals. *Acc. Chem. Res.* **43,** 1257–1266 (2010).
40. M. J. Smith, Using Differential Scanning Calorimetry To Explore the Phase Behavior of Chocolate. *J. Chem. Educ.* (2016). doi:10.1021/acs.jchemed.5b00284
41. J. Bauer, S. Spanton, R. Henry, J. Quick, W. Dziki, W. Porter, J. Morris, Ritonavir: An Extraordinary Example of Conformational Polymorphism. *Pharm. Res.* **18,** 859–866
42. L. Yu, Color Changes Caused by Conformational Polymorphism: Optical-Crystallography, Single-Crystal Spectroscopy, and Computational Chemistry. *J. Phys. Chem. A* **106,** 544–550 (2002).
43. J. B. Birks, *Photophysics of Aromatic Molecules*. (John Wiley & Sons Ltd., London, 1970).
44. B.-K. An, S.-K. Kwon, S.-D. Jung, S. Y. Park, Enhanced Emission and Its Switching in Fluorescent Organic Nanoparticles. *J. Am. Chem. Soc.* **124,** 14410–14415 (2002).
45. B.-K. An, J. Gierschner, S. Y. Park, π-Conjugated cyanostilbene derivatives: a unique self-assembly motif for molecular nanostructures with enhanced emission and transport. *Acc. Chem. Res.* **45,** 544–554 (2012).
46. Y. Hong, J. W. Y. Lam, B. Z. Tang, Aggregation-induced emission. *Chem. Soc. Rev.* **40,** 5361–5388 (2011).
47. J. Luo, Z. Xie, J. W. Y. Lam, L. Cheng, B. Z. Tang, H. Chen, C. Qiu, H. S. Kwok, X. Zhan, Y. Liu, D. Zhu, Aggregation-induced emission of 1-methyl-1,2,3,4,5-

pentaphenylsilole. *Chem. Commun.* 1740–1741 (2001).
48. Y. Hong, J. W. Y. Lam, B. Z. Tang, Aggregation-induced emission: phenomenon, mechanism and applications. *Chem. Commun.* 4332–4353 (2009).
49. Reproduced with permission, copyright 2015 Materials Research Society: K. Chung, Y. Yu, M. S. Kwon, J. Swets, J. Kim, J. H. Youk, Assembly and alignment of conjugated polymers: materials design, processing, and applications. *MRS Commun.* **5,** 169–189 (2015).
50. J. Kim, S. K. McHugh, T. M. Swager, Nanoscale Fibrils and Grids: Aggregated Structures from Rigid-Rod Conjugated Polymers. *Macromolecules* **32,** 1500–1507 (1999).
51. T. Kanetake, K. Ishikawa, T. Koda, Y. Tokura, K. Takeda, Highly oriented polydiacetylene films by vacuum deposition. *Appl. Phys. Lett.* **51,** 1957 (1987).
52. H. Heil, T. Finnberg, N. von Malm, R. Schmechel, H. von Seggern, The influence of mechanical rubbing on the field-effect mobility in polyhexylthiophene. *J. Appl. Phys.* **93,** 1636–1641 (2003).
53. C. Y. Yang, C. Soci, D. Moses, A. J. Heeger, Aligned rrP3HT film: Structural order and transport properties. *Synth. Met.* **155,** 639–642 (2005).
54. L. Biniek, S. Pouget, D. Djurado, E. Gonthier, K. Tremel, N. Kayunkid, E. Zaborova, N. Crespo-Monteiro, O. Boyron, N. Leclerc, S. Ludwigs, M. Brinkmann, High-Temperature Rubbing: A Versatile Method to Align π-Conjugated Polymers without Alignment Substrate. *Macromolecules* **47,** 3871–3879 (2014).
55. Z. Zheng, K.-H. Yim, M. S. M. Saifullah, M. E. Welland, R. H. Friend, J.-S. Kim, W. T. S. Huck, Uniaxial alignment of liquid-crystalline conjugated polymers by nanoconfinement. *Nano Lett.* **7,** 987–992 (2007).
56. M. Aryal, K. Trivedi, W. W. Hu, Nano-confinement induced chain alignment in ordered P3HT nanostructures defined by nanoimprint lithography. *ACS Nano* **3,** 3085–3090 (2009).
57. G. Ding, Y. Wu, Y. Weng, W. Zhang, Z. Hu, Solvent-Assistant Room Temperature Nanoimprinting-Induced Molecular Orientation in Poly(3-hexylthiophene) Nanopillars. *Macromolecules* **46,** 8638–8643 (2013).
58. H. Sirringhaus, R. J. Wilson, R. H. Friend, M. Inbasekaran, W. Wu, E. P. Woo, M. Grell, D. D. C. Bradley, Mobility enhancement in conjugated polymer field-effect transistors through chain alignment in a liquid-crystalline phase. *Appl. Phys. Lett.* **77,** 406 (2000).
59. H.-R. Tseng, L. Ying, B. B. Y. Hsu, L. A. Perez, C. J. Takacs, G. C. Bazan, A. J. Heeger, High mobility field effect transistors based on macroscopically oriented regioregular copolymers. *Nano Lett.* **12,** 6353–6357 (2012).
60. H.-R. Tseng, H. Phan, C. Luo, M. Wang, L. A. Perez, S. N. Patel, L. Ying, E. J. Kramer, T.-Q. Nguyen, G. C. Bazan, A. J. Heeger, High-mobility field-effect transistors fabricated with macroscopic aligned semiconducting polymers. *Adv. Mater.* **26,** 2993–2998 (2014).
61. C. Luo, A. K. K. Kyaw, L. A. Perez, S. Patel, M. Wang, B. Grimm, G. C. Bazan, E. J. Kramer, A. J. Heeger, General strategy for self-assembly of highly oriented nanocrystalline semiconducting polymers with high mobility. *Nano Lett.* **14,** 2764–2771 (2014).
62. J. Wu, A. F. Gross, S. H. Tolbert, Host−Guest Chemistry Using an Oriented Mesoporous Host: Alignment and Isolation of a Semiconducting Polymer in the Nanopores of an Ordered Silica Matrix. *J. Phys. Chem. B* **103,** 2374–2384 (1999).
63. M W. C. Molenkamp, M. Watanabe, H. Miyata, S. H. Tolbert, Highly polarized

luminescence from optical quality films of a semiconducting polymer aligned within oriented mesoporous silica. *J. Am. Chem. Soc.* **126,** 4476–4477 (2004).
64. I. B. Martini, I. M. Craig, W. C. Molenkamp, H. Miyata, S. H. Tolbert, B. J. Schwartz, Controlling optical gain in semiconducting polymers with nanoscale chain positioning and alignment. *Nat. Nanotechnol.* **2,** 647–652 (2007).
65. D. Iacopino, P. Lovera, A. O'Riordan, G. Redmond, Highly polarized luminescence from β-phase-rich poly(9,9-dioctylfluorene) nanofibers. *J. Phys. Chem. A* **118,** 5437–5442 (2014).
66. T. W. Hagler, K. Pakbaz, K. F. Voss, A. J. Heeger, Enhanced order and electronic delocalization in conjugated polymers oriented by gel processing in polyethylene. *Phys. Rev. B* **44,** 8652–8666 (1991).
67. C. Weder, C. Sarwa, C. Bastiaansen, P. Smith, Highly polarized luminescence from oriented conjugated polymer/polyethylene blend films. *Adv. Mater.* **9,** 1035–1039 (1997).
68. Z. Zhu, T. M. Swager, Conjugated Polymer Liquid Crystal Solutions: Control of Conformation and Alignment. *J. Am. Chem. Soc.* **124,** 9670–9671 (2002).
69. C.-C. Kuo, C.-T. Wang, W.-C. Chen, Highly-Aligned Electrospun Luminescent Nanofibers Prepared from Polyfluorene/PMMA Blends: Fabrication, Morphology, Photophysical Properties and Sensory Applications. *Macromol. Mater. Eng.* **293,** 999–1008 (2008).
70. M. Campoy-Quiles, Y. Ishii, H. Sakai, H. Murata, Highly polarized luminescence from aligned conjugated polymer electrospun nanofibers. *Appl. Phys. Lett.* **92,** 213305 (2008).
71. K. Yin, L. Zhang, C. Lai, L. Zhong, S. Smith, H. Fong, Z. Zhu, Photoluminescence anisotropy of uni-axially aligned electrospun conjugated polymer nanofibers of MEH-PPV and P3HT. *J. Mater. Chem.* **21,** 444 (2011).
72. J. C. Wittmann, B. Lotz, Epitaxial crystallization of polymers on organic and polymeric substrates. *Prog. Polym. Sci.* **15,** 909–948 (1990).
73. De Rosa C, C. Park, E. Thomas, B. Lotz, Microdomain patterns from directional eutectic solidification and epitaxy. *Nature* **405,** 433–437 (2000).
74. M. Brinkmann, J.-C. Wittmann, Orientation of Regioregular Poly(3-hexylthiophene) by Directional Solidification: A Simple Method to Reveal the Semicrystalline Structure of a Conjugated Polymer. *Adv. Mater.* **18,** 860–863 (2006).
75. C. Müller, M. Aghamohammadi, S. Himmelberger, P. Sonar, M. Garriga, A. Salleo, M. Campoy-Quiles, One-Step Macroscopic Alignment of Conjugated Polymer Systems by Epitaxial Crystallization during Spin-Coating. *Adv. Funct. Mater.* **23,** 2368–2377 (2013).
76. B. Dörling, V. Vohra, T. T. Dao, M. Garriga, H. Murata, M. Campoy-Quiles, Uniaxial macroscopic alignment of conjugated polymer systems by directional crystallization during blade coating. *J. Mater. Chem. C* **2,** 3303 (2014).
77. K. Chung, M. S. Kwon, B. M. Leung, A. G. Wong-Foy, M. S. Kim, J. Kim, S. Takayama, J. Gierschner, A. J. Matzger, J. Kim, Shear-Triggered Crystallization and Light Emission of a Thermally Stable Organic Supercooled Liquid. *ACS Cent. Sci.* **1,** 94–102 (2015) - Published by American Chemical Society.
78. K. Chung, A. McAllister, D. Bilby, B.-G. Kim, M. S. Kwon, E. Kioupakis, J. Kim, Designing interchain and intrachain properties of conjugated polymers for latent optical information encoding. *Chem. Sci.* **6,** 6980–6985 (2015) - Published by The Royal Society of Chemistry.

CHAPTER 2

Shear-triggered Lighting-up Crystallization of a Thermally Stable Organic Supercooled Liquid

ACS Central Science, **1**, 94-102 (2015) – Published by American Chemical Society

2.1. Introduction

Rational material design, considering intramolecular properties as well as intermolecular properties, is very important to realize desired optimal characteristics of organic materials. Moreover, an insightful material design strategy can also enable us to achieve unique supramolecular assembly for interesting properties. In this chapter, it is demonstrated how molecular architectures can render a stable supercooled liquid, which generally considered as a metastable short-lived state, having a unique stimuli-responsive optical property, which may have great potential in optical and biomedical applications.

When molten organic crystalline materials are cooled below their melting temperature (T_m), exothermic crystallization is usually observed and the molecules revert to the energetically favorable crystalline phase. Even though some crystalline organic materials can stay in a supercooled liquid state (above glass transition temperature, T_g) or a glass state (below T_g) upon rapid cooling, these materials crystallize upon subsequent heating.[1–4] Only a few crystalline organic molecules exhibit thermally stable supercooled liquid without crystallization despite

their energetically more favorable crystalline phase and sufficient mobility of the molecule above T_g.[5–8] In fact, the thermal stability of amorphous organic materials including supercooled liquids and glasses is a subject of considerable commercial importance. For example, conjugated organic glasses without good thermal stability can derogate the reliability of organic electronic devices due to device failure by crystallization during the operation.[9–11] In the field of drug delivery, pharmaceutical organic glasses have been widely studied due to their advantageous solubility, bioavailability and consistent efficacy.[7,12] However, unlike those widely researched and exploited organic glasses, organic supercooled liquids have been investigated mainly in theoretical aspects such as glass transition phenomenon and structural relaxation dynamics.[2,13–16]

Diketopyrrolopyrrole (DPP) derivatives have been widely-used as high performance pigments[17] as well as one of the frequently used building blocks for conjugated polymers in electronic applications[18,19] due to strong intermolecular interactions between the DPP units. During the investigation on DPP derivatives as a monomeric unit of conjugated polymers, we observed that a DPP molecule, DPP8, formed both a crystalline solid and a stable supercooled liquid at room temperature. The stable supercooled liquid DPP8 did not transform back to crystalline solid even under subsequent heating and cooling cycles. It is an intriguing question what the origin of thermally stable supercooled liquid is and what chemical features make organic crystalline materials to form an extraordinarily stable supercooled liquid. We examined the mechanism and molecular features allowing the stable supercooled liquid formation. For a systematic investigation, a series of DPP derivatives by altering the alkyl chain length, DPP4, DPP8, DPP12 and DPP16, are synthesized and characterized in terms of supercooled liquid formation and theirs thermal stability (**Figure 2.1a**).

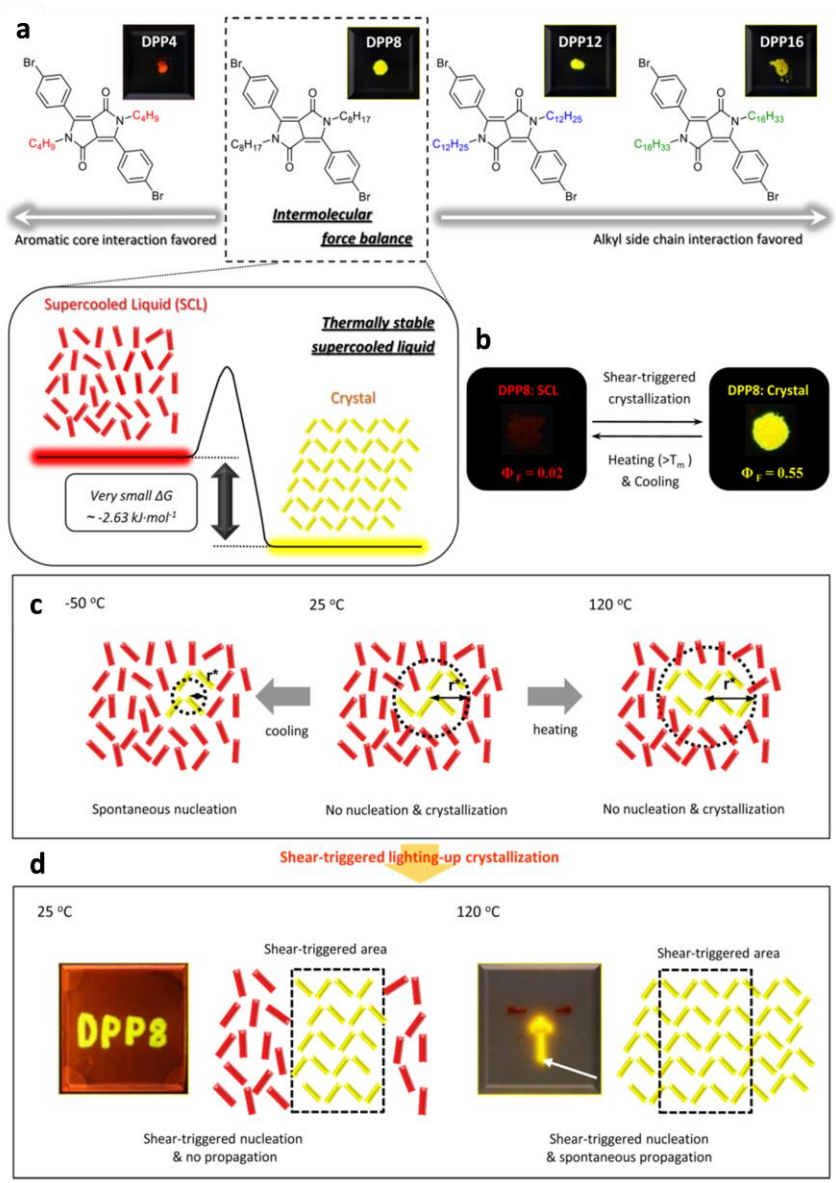

Figure 2.1 Schematic illustration of the thermally stable supercooled liquid and shear-triggered lighting-up crystallization of DPP8. (a) Chemical structure of DPP8 and its derivatives. A subtle force balance between two different intermolecular interactions acting in opposite directions makes DPP8 exhibit small ΔG between supercooled liquid and crystalline solid phases, resulting in intriguing thermally stable supercooled liquid. Fluorescence images are from crystalline solids of the derivatives. (b) Reversible phase transformation with large optical property change between the two forms by means of independent stimuli. (c) Nucleation is restricted in DPP8 supercooled liquid due to an unattainable yet required large critical radius (r^*), which results from small ΔG between two phases, at 25 ^{o}C and 120 ^{o}C. However, when molten DPP8 was cooled to -50 ^{o}C subsequent heating developed crystallization. (d) Shear-triggered lighting-up crystallization of DPP8. Photographs (a, b and d) were taken under 365 nm UV light.

Interestingly, the stable supercooled liquid DPP8 crystallizes by shear force accompanied by dramatic optical property changes. Even though the role of shear stress in crystallization has been investigated both experimentally and theoretically, the relationship is still not conclusive; several studies report shear-induced ordering with enhancing nucleation rate, while others report suppression of crystallization by shear force.[20–26] Macromolecules with a large aspect ratio such as isotactic polypropylene and polystyrene can be crystallized by shear force due to chain alignment.[27–29] However, the shear-triggered crystallization of DPP8 with a remarkable optical property change is an intriguing phenomenon observed from organic small molecules.

In a phenomenological view, shear-triggered lighting-up crystallization is quite similar to the mechanochromism of organic compounds.[30–34] Mechanochromic organic compounds show color and/or fluorescence change when external forces such as pressure and shear are applied. However, while mechanochromism is based on polymorphism or on an order-to-disorder transformation (i.e. breaking the crystalline structure towards amorphous or disrupting secondary bonding such as hydrogen bonding) by applied mechanical force, the shear-triggered crystallization reported here is a distinctive disorder-to-order transition.

Our investigation revealed that DPP8 has the highest thermal stability of supercooled liquid among the derivatives, and the thermal stability is ascribed to small Gibbs free energy difference between supercooled liquid and crystalline solid that is originated from a subtle force balance between aromatic interactions among the core units and van der Waals interactions among the aliphatic side chains working in opposite directions (**Figure 2.1a**). Furthermore, we demonstrate direct writing of fluorescent patterns and propagating fluorescence amplification, respectively, by applying shear to a supercooled liquid DPP8 film at different temperatures (**Figure 2.1d**). A threshold shear rate of 0.03 s^{-1} and the corresponding shear stress of 0.90 kPa for shear-triggered

crystallization were measured by rheometry, which is million times smaller than the typically required stress range for mechanochromism observed in organic materials (1 GPa).[35,36] The high sensitivity of the shear-triggered crystallization was further confirmed by crystallization of a supercooled DPP8 film even by living cell attachment and spreading.

2.2. Results and Discussion

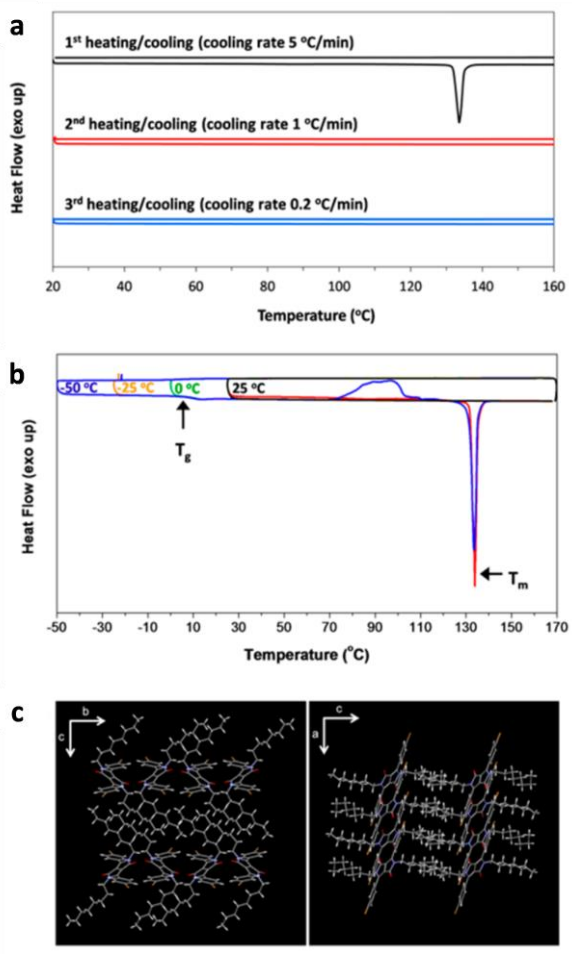

Figure 2.2 Thermal properties and single crystal structure of DPP8. (a) DSC trace at different cooling rates (heating rate: 10 $^{o}C \cdot min^{-1}$). (b) DSC trace with different cooling temperatures (Scan rate: heating 10 $^{o}C \cdot min^{-1}$, cooling 5 $^{o}C \cdot min^{-1}$). A glass transition (T_g) was observed at 5 ^{o}C. (c) Single crystal structure of DPP8.

We designed and synthesized DPP8 as a monomeric unit of a series of conjugated polymers. During the characterization of this compound, we observed an interesting phenomenon. While crystalline DPP8 powder, purified by recrystallization, melts at 134 ^{o}C as seen in the differential scanning calorimetry (DSC) trace in **Figure 2.2a**, subsequent cooling of the molten DPP8 results in a supercooled liquid phase stable down to 25 ^{o}C, equivalent to more than a range of 100 ^{o}C below the melting temperature. The supercooled liquid phase persists during the second and third DSC

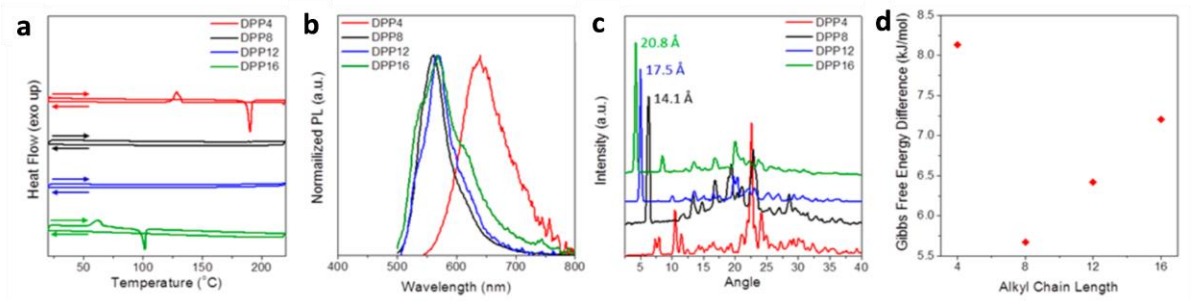

Figure 2.3 The effects of molecular design on thermal, optical, molecular packing properties, and ΔG characteristics. (a) DSC trace (2nd cycle) of DPP derivatives (scan rate 10 °C·min^{-1}). (b) Normalized PL of shear-triggered (DPP8 and DPP12) and thermally driven (DPP4 and DPP16) crystals. (c) Powder XRD traces. DPP8, 12, 16 have similar lamellar packing patterns in contrast to the drastically different diffraction pattern of DPP4.(d) ΔG between the crystalline solid and supercooled liquid phases of DPP derivatives (from the Hoffman equation, at 26 °C).

cycles without showing any crystallization peaks. No crystallization is observed even at a very slow cooling rate of 0.2 °C·min^{-1} (**Figure 2.2a**).

In order to investigate the chemical features that make DPP8 so special in forming such thermally stable supercooled liquid we synthesized three more DPP derivatives having butyl (DPP4), dodecyl (DPP12) and hexadecyl side chains (DPP16) (**Figure 2.1a**). The DPP core unit without alkyl chains is hardly soluble in organic solvents due to strong intermolecular interactions and consequently produces red fluorescent emission with negligible quantum yield due to the well-known concentration induced self-quenching. However, the introduction of the octyl chains in DPP8 makes DPP8 to form weakly coupled aromatic DPP cores together with lamellar-type octyl chain packing as evident from the X-ray crystal structure (**Figure 2.2c**). Strong hydrogen bonding, π-π interaction, or halogen bonding is not observed.

Different from DPP8, molten DPP4 crystallizes upon cooling (**Figure 2.3a**). The DPP4 crystal shows red fluorescence, which is largely red-shifted from the greenish yellow emission of the DPP8 crystal (**Figure 2.1a and Figure 2.3b**), and is ascribed to closely packed aromatic core units just like unsubstituted DPP core unit. DPP4 crystal shows strikingly different powder XRD

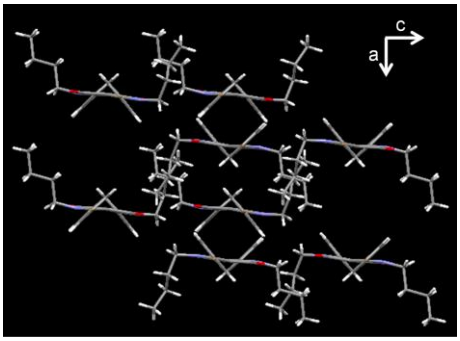

Figure 2.4 Single crystal structure of DPP4. Closely packed aromatic cores between nearest molecules are clearly observed.

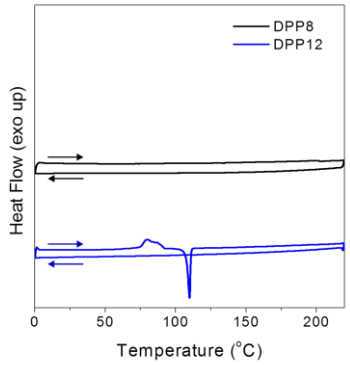

Figure 2.5 DSC trace (2nd cycle) of DPP8 and DPP12 (scan rate 10 °C·min^{-1} down to 0 °C). While DPP12 did not show any crystallization peak upon subsequent heating when it was cooled down to 20 °C (Figure 2.3a), onset of crystallization peak was observed at 57 °C upon subsequent heating when DPP12 was cooled down to 0 °C.

pattern and single crystal structure compared to DPP8 (**Figure 2.3c** and **Figure 2.4**); different from the weakly coupled DPP8 aromatic cores, the DPP4 cores are closely packed with a distance of ca. 3.5 Å (**Figure 2.4**). DPP12 and DPP16 on the other hand show identical PL emission (**Figure 2.1a** and **Figure 2.3b**) and similar powder XRD patterns as DPP8 (**Figure 2.3c**), implying similarly weakly coupled aromatic cores and lamellar-type packing of the side chains. The alkyl chain length represented in the lamellar distance increases linearly from *n* =8 to 12, 16 in steps of ca. 3.4 Å as calculated from the sharp peaks at ca. 5° in the powder XRD trace (**Figure 2.3C**). Even though the packing seems to be similar to DPP8, the thermal stability of the supercooled liquid of DPP12 and DPP16 is not the same as that of DPP8. While DPP8 did not show crystallization upon subsequent heating until the cooling temperature reached -50 °C (**Figure 2.2b**), DPP12 showed crystallization beginning at 57 °C and melting at 108 °C upon subsequent heating after it was cooled down to 0 °C (**Figure 2.5**). Moreover, DPP16 needed to be cooled to only 20 °C in order to show a broad crystallization peak followed by melting at 102 °C upon subsequent heating (**Figure 2.3a**).

Apparently, the different alkyl chain length of the DPP derivatives triggers a distinctive difference in the thermal stability of their supercooled liquids: DPP8 is most stable among the derivatives and when the alkyl chain is shorter (DPP4) or longer (DPP12 and 16) than octyl the thermal stability of the supercooled liquid diminishes. From these results, we attribute the origin of the thermally stable supercooled liquid of DPP8 to a delicate force balance between the aromatic interactions and aliphatic van der Waals forces acting in opposite directions (**Figure 2.1a**). If the alkyl chain is short (DPP4), strong interactions among the DPP cores induce crystallization upon cooling of the melt because the van der Waals interactions among the short alkyl chain cannot provide strong enough force to balance against the interactions. On the contrary, as the alkyl chain gets longer (DPP12 and DPP16) the van der Waals interactions among the lamellar packed alkyl side chains become stronger than the interactions between the weakly coupled DPP cores, resulting in less thermally stable supercooled liquid. Then, how does this delicate force balance built in DPP8 suppress the crystallization of DPP8?

According to homogeneous nucleation theory,[37] two processes should be accomplished for crystallization, i.e. nucleation and propagation. The Gibbs free energy of nucleation, $\Delta G^{nucleation}$, for a (spherical) nucleus with radius r in a supercooled liquid is expressed as the sum of the energy gain by generating an energetically more favorable crystalline nucleus and the energy loss by producing the interface, driven by surface tension (σ).

$$\Delta G^{nucleation} = \frac{4}{3}\pi r^3 \Delta G_v + 4\pi r^2 \sigma \qquad [1]$$

For $dG/dr = 0$, the critical radius of nucleation (r^*) is derived, corresponding to the minimum nucleus which can continue growing spontaneously and which is inversely proportional to the

Gibbs free energy difference (ΔG_v = G_v(crystal) – G_v(supercooled liquid)) between the supercooled liquid and the crystalline phase. ΔH_v is heat of transformation.

$$r^* = -\frac{2\sigma}{\Delta G_v} \sim -\frac{2\sigma T_m}{\Delta H_v (T_m - T)} \qquad [2]$$

If the radius of nuclei is larger than *r**, the mobility of the molecules in the liquid phase will determine the growth rate of the crystallization process. According to Equation 2, at small undercooling below T_m, a larger nucleus is necessary for crystallization, but the higher mobility of molecules is favorable for crystal growth. In contrast, as temperature goes further down, while the critical radius *r** decreases, which means that even a small nucleus can survive, the mobility of the molecules also decreases, slowing down crystal growth.

In order to achieve a thermally stable supercooled liquid, nucleation in the supercooled state should be forbidden. Otherwise, even though molten organic crystalline materials may remain as supercooled liquid at a reduced temperature due to the restricted molecular mobility and the ensuing retarded crystal growth, they will eventually crystallize upon subsequent heating. If ΔG between supercooled liquid and crystalline solid is very small, the critical radius of nucleation (*r**) largely increases so that nucleation is suppressed, promoting kinetically entrapped supercooled liquid formation. In other word, a small ΔG between the supercooled liquid and crystalline solid states results in unattainable yet required large critical radius *r** so as to restrict nucleation. We hypothesize that the supercooled liquid DPP8 is thermally stable because nucleation is forbidden over such a large supercooling temperature range (over 100 ^oC) due to very small ΔG between the supercooled liquid and the crystalline solid, which is originated from the subtle force balance between the two different intermolecular interactions acting opposite

direction as schematically illustrated in **Figure 2.1, a** and **c**. In other word, DPP8 is expected to have a particularly small value of ΔG.

The fact that nucleation is forbidden in the supercooled liquid DPP8 was proven by means of a seeding test with the crystalline powder.[38] When DPP8 crystalline powder was dropped onto the supercooled liquid at 120 ^{o}C, the crystallites serve as stable nuclei so that crystallization propagated through entire area of the connected supercooled liquid due to the sufficient molecular mobility. In contrast, the adjacent yet disconnected supercooled liquid domain did not show crystallization due to the absence of nuclei. Seeding at 25 ^{o}C on the other hand did not induce spontaneous propagation of crystallization due to limited molecular mobility. However, when the temperature was increased to ~70 ^{o}C crystallization began to propagate, which means that in pristine supercooled liquid state nuclei are absent even at 25 ^{o}C. Taken together with the thermal cycling experiments, these findings demonstrate that nucleation is the limiting step in DPP8 crystallization. If the required large critical radius r^* which results from small ΔG between two phases is responsible for the absent crystallization as suggested (**Figure 2.1c**), there should be a threshold temperature at which the required critical radius r^* can be extremely small due to large supercooling. Indeed, while the supercooled liquid was stable down to -25 ^{o}C, cooling to -50 ^{o}C and subsequent heating induced crystallization (**Figure 2.2b**). When the crystallized DPP8 was melted again and cooled to room temperature no crystallization was observed upon subsequent heating, implying that crystallization of DPP8 is independent of thermal history.

Now, the question is whether ΔG between the supercooled liquid and the crystalline solid is indeed small. The single crystal structure of DPP8 does not show close packing but only weakly coupled aromatic DPP cores and lamellar-type octyl chain packing (**Figure 2.2c**). ΔG between the two phases of DPP8 was estimated to be -2.63 kJ·mol^{-1} (-0.63 kcal·mol^{-1}) at 26 ^{o}C by means

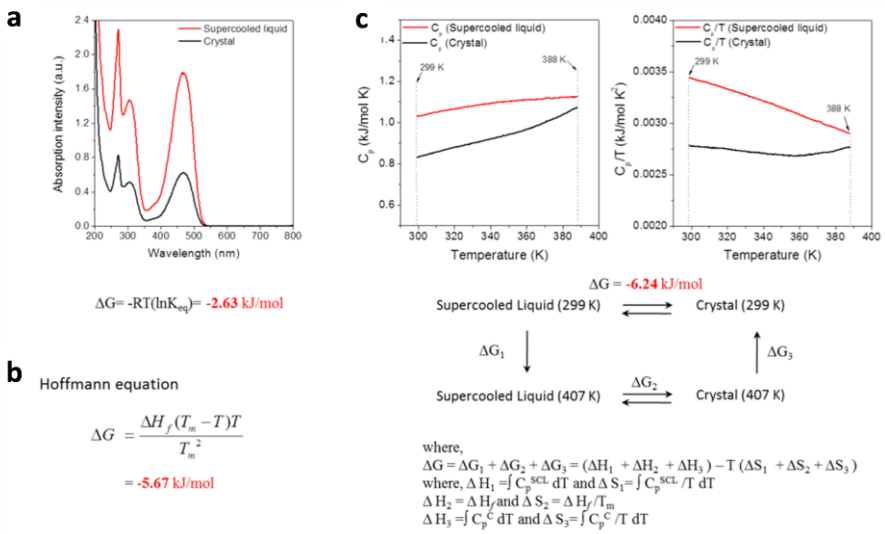

Figure 2.6 Methods for calculation of ΔG between supercooled liquid and crystalline solid of DPP8. (a) Relative solubility measurement for ΔG calculation. UV-vis absorption spectra of crystal solution and supercooled liquid solution at equilibrium were collected for ΔG calculation (Solvent: water in methanol (1:7)). The ratio of the absorption intensities represents the equilibrium constant (K_{eq}) in the following equation: $\Delta G = -RT(\ln K_{eq})$. The calculated ΔG between supercooled liquid state and crystalline solid state is -2.63 kJ·mol^{-1} at 26 ^{o}C (-0.63 kcal·mol^{-1}). This value may be slightly underestimated due to the observed crystallization of small fraction of supercooled liquid under the experimental conditions. (b) ΔG calculation from Hoffmann equation. T_m and ΔH_f were measured by means of Discovery DSC. Calculated ΔG is -5.67 kJ·mol^{-1} at 26 ^{o}C (-1.35 kcal·mol^{-1}). This value may slightly deviate from the real value because heat capacity is not considered in the equation. (c) ΔG calculation considering heat capacity (C_p) of supercooled liquid and crystalline solid. The calculation procedure is presented in the figure. The calculated ΔG is -6.24 kJ·mol^{-1} at 26 ^{o}C (-1.49 kcal·mol^{-1}) may be slightly overestimated due to additional heat capacity contribution from 388 K (115 ^{o}C) to melting temperature 407 K (134 ^{o}C).

of relative solubility measurements (**Figure 2.6a**).[39] We also used Hoffman equation to calculate ΔG = -5.67 kJ·mol^{-1} (-1.35 kcal·mol^{-1}) at 26 ^{o}C (**Figure 2.6b**).[40] ΔG can also be estimated from a thermodynamic cycle (Hess's law) utilizing ΔG = ΔH -TΔS, where ΔH and ΔS can be deduced from heat capacity via Kirchhoff's law, giving ΔG = -6.24 kJ·mol^{-1} (-1.49 kcal·mol^{-1}) at 26 ^{o}C from this third method (**Figure 2.6c**). Hence, the three methods consistently gave a small ΔG value (2.63 – 6.24 kJ·mol^{-1}), which is comparable to the ΔG between polymorphs[39] and is even much smaller than 50.21 kJ·mol^{-1} (12 kcal·mol^{-1}) of the ΔG between *cis*- and *trans*-azobenzene,

a well-known photo-isomerizable compound.[41] Therefore, the thermally stable supercooled liquid state of DPP8 is due to the unattainable yet required large critical radius r^* originating from a small ΔG between the supercooled liquid and crystalline solid states.

The calculated ΔG between supercooled liquid and crystalline solid clearly represent the trend of thermal stability of supercooled liquid of the derivatives (**Figure 2.3d**). ΔG of the derivatives were calculated from the Hoffman equation.[40] DPP4 with the highest ΔG value from Hoffman equation shows crystallization upon cooling of melt because the crystal is much more stable than the supercooled liquid state (**Figure 2.3a**). DPP16 shows crystallization upon subsequent heating after cooling to 25 ^{o}C (**Figure 2.3a**). DPP12 shows crystallization upon subsequent heating after cooling to 0 ^{o}C (**Figure 2.5**). DPP8 with the lowest ΔG exhibit most stable supercooled liquid compared to the rest of derivatives, which again implies that the small ΔG of DPP8 provides the smallest driving force for crystallization, whereas larger van der Waals interactions between molecules (DDP12 and DDP16) or stronger core interactions (DPP4) increase the driving force. Therefore, the subtle force balance between the aliphatic side chains and the aromatic core of DPP8 is the key feature to make its ΔG small enough to suppress crystallization and ensuing a thermally stable supercooled liquid.[42]

Although the Gibbs free energy difference between supercooled liquid and crystalline solid of DPP8 is very small, the differences in the optical properties are dramatic (**Figure 2.7a**). The PL emission of the crystal is bright greenish yellow with emission at λ_{max}=562 nm and a PL quantum yield of Φ_{PL}=0.55 in contrast to the dim orange-red emission of the supercooled liquid having λ_{max}=629 nm and Φ_{PL}=0.02. The PL lifetime, τ_{PL}, and the radiative rate constant ($k_r=\Phi_{PL}/\tau_{PL}$) of the crystalline DPP8 are similar to the solution values (**Table 2.1**), which implies a weakly coupled system with no preferential H-or J-type coupling in the solid state.[43] The

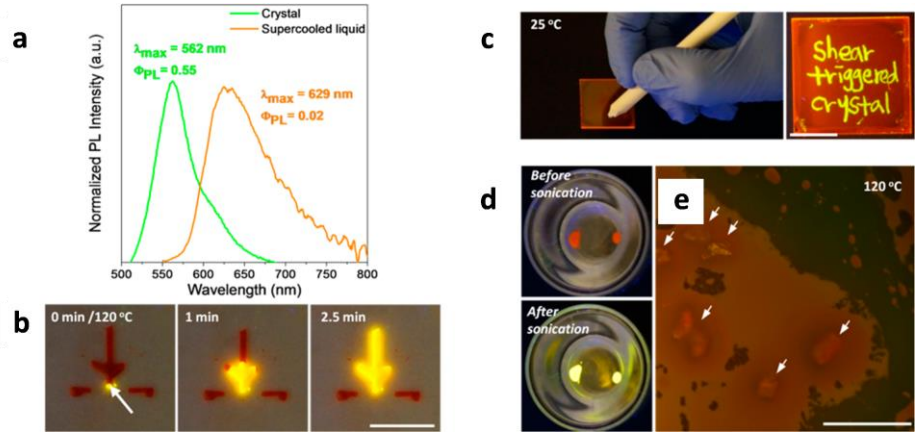

Figure 2.7 Different optical property of the two phases and shear-triggered lighting-up crystallization of DPP8: Role of shear and dual mode crystallization. (a) Normalized fluorescence emission spectra and quantum yields of DPP8 crystal and supercooled liquid at room temperature. (b) Shear at the tip (white arrow) of the tree-shape supercooled DPP8 pattern triggered crystallization and propagation through entire tree pattern at 120 ^{o}C. However, the two disconnected horizontal lines stayed at the supercooled liquid state (scale bar: 1 cm). (c) Direct writing of fluorescent patterns at 25 ^{o}C. The only shear-applied area turned into greenish yellow crystal (scale bar: 1 cm). (d) Supercooled liquid DPP8 before sonication and after sonication followed by heating to 120 ^{o}C. Sonic wave was applied as a source of molecular agitation. (e) In order to study the effects of intentionally introduced heterogeneous nucleation sites, sea sands (white arrows) were mixed with DPP8 melt followed by cooling to 25 ^{o}C and subsequent heating to 120 ^{o}C. Fluorescence image under optical microscope was taken after 5 min at 120 ^{o}C (scale bar: 0.5 mm). Photographs (b, c and d) were taken under 365 nm UV light.

emission is red-shifted by ca. 700 cm^{-1} (22 nm) against solution (**Figure 2.8a**), which can be ascribed to the higher polarizability in the crystalline state compared to solution.[44,45] The single crystal structure analysis shows molecular layers kept effectively apart by the long alkyl chains (**Figure 2.2c**). Within a layer, nearest neighbors are substantially shifted along the long molecular axis, suggesting weak J-coupling, while second nearest neighbors are side-by-side oriented, giving rise to some H-coupling, so that the effects should cancel each other in a first approximation. This was examined by quantum chemical calculations of an assembly of four DPP8 molecules, which indicates indeed very weak H-aggregation (**Figure 2.8b**).[46] Such weakly coupled systems are known to be highly luminescent even in the polycrystalline state,[33]

Table 2.1 Optical and photophysical data of DPP8. Absorption and emission maxima, PL lifetimes (τ_{PL}) and quantum yields (Φ_{PL}), rate constants for radiative (k_r) and non-radiative deactivation (k_{nr}), calculated from $\Phi_{PL} = k_r \cdot \tau_{PL} = k_r \cdot (k_r + k_{nr})^{-1}$

System		λ_{abs} / nm	λ_{em} / nm	Stokes shift / cm^{-1}	Φ_{PL}	τ_{PL} / ns	k_r / ns^{-1}	k_{nr} / ns^{-1}
Solution	$CHCl_3$	479	540	2358	0.71[a]	6.05	0.117	0.049
Crystalline solid	powder		562[c]		0.55[b]	4.58	0.120	0.098
	shear (393 K)		562[c]		0.50[b]			
Supercooled liquid	powder		629[c]		0.02[b]	2.13	0.011	0.460
	Powder (77K)				0.18	7.82	0.023	0.105
	film	493	623	4233	0.02[b]	2.35	0.008	0.418

[a] from relative quantum yield measurement against Rhodamine 6G. [b] from absolute measurements in an integrating sphere. [c] subject to reabsorption

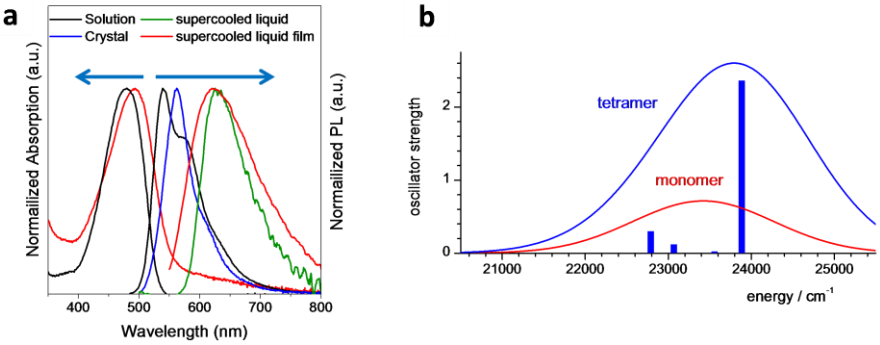

Figure 2.8 Measured and calculated optical properties of DPP8. (a) Normalized absorption and emission spectra of solution, crystalline solid and supercooled liquid of DPP8. (b) Calculated absorption spectra (ZINDO//DFT) of DPP8 molecule (red) and an assembly of four DPP8 molecules (as taken from the crystal structure; blue).

essentially due to reduced exciton diffusion.[47]

In contrast to the crystalline phase, the supercooled liquid DPP8 effectively quenches emission, exhibiting a weak, unstructured and strongly red-shifted excimer-like PL spectrum with a large Stokes shift of 3800 cm^{-1} (130 nm; see **Figure 2.8a**).[48] According to our photophysical analysis (**Table 2.1**), PL quenching caused by two factors; (i) a low radiative rate k_r, reduced by a factor of 10 compared to solution, and (ii) a large rate constant for non-radiative deactivation (k_{nr}), enhanced by a factor of 10 against solution. While these features could be interpreted as typical characteristics of H-aggregation in polycrystalline samples,[47] the

absorption spectrum of the supercooled liquid does not support such interpretation. For strong H-aggregates a substantial hypsochromic shift relative to solution is expected,[47] while in the current case a red-shift against solution by ca. 600 cm^{-1} (**Figure 2.8a**) is observed, which agrees with the expected polarizability effect. In the supercooled liquid, all possible intermolecular orientations may be realized which should enhance effective trapping by exciton migration through a multitude of structural trap states.[47] While the majority of traps might deactivate non-radiatively causing the strong increase of k_{nr}, stacks with strong π-π overlap act as deep traps which give rise to the small radiative rate k_r, and the faint excimeric emission.[47]

Interestingly, upon applying shear force, the dim orange-red fluorescent supercooled liquid transforms to bright greenish yellow fluorescent crystals (**Figure 2.7, b and c**, **Figure 2.1, b and d**). We hypothesized that the shear force might induce rearrangement and density fluctuation of DPP8 molecules and thereby help embryos surpass the critical radius of nucleation (r*) to become active nuclei.[15] To verify the proposed role of shear force in the shear-triggered crystallization of DPP, we investigated the effect of molecular agitation on the crystallization of supercooled liquid DPP8. In this experiment, sonic wave was applied as an external energy source to induce rearrangement and density fluctuation of DPP8 molecules through simple agitation of DPP8 molecules in the supercooled liquid. Applied sonic wave helps nucleation in supercooled liquid DPP8 and develops crystallization upon subsequent heating as shown in **Figure 2.7d**, supporting the hypothesis that rearrangement and density fluctuation of DPP8 by external energy, such as shear force and sonic wave, can stimulate nucleation.

The role of shearing in the shear-triggered crystallization was further verified by adding sea sand, as a heterogeneous nucleation site, to supercooled liquid DPP8. It has been well known that

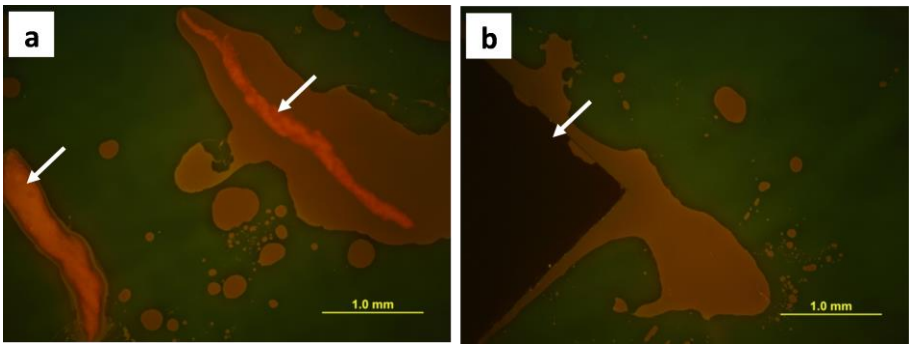

Figure 2.9 Heterogeneous nucleation test with hydrophobic foreign interfaces. (a) Eraser powders (white arrows) and (b) a piece of polyimide film (white arrow) were mixed with DPP8 melt followed by cooling to 25 ^{o}C and subsequent heating to 120 ^{o}C. Fluorescence images under optical microscope were taken after 5 min at 120 ^{o}C.

the nucleation is promoted when heterogeneous nucleation sites, such as rough or scratched surface, are provided in the system.[49–51] Sea sand was mixed with molten DPP8 and the mixture was cooled to room temperature followed by subsequent heating to 120 ^{o}C. Even though DPP8 molecules have enough mobility at this temperature and even in the presence of interfaces provided by sea sand, no crystallization was observed (**Figure 2.7e**). Similarly, no crystallization was observed even hydrophobic particles, including rubber powders from the same eraser used for the fluorescence pattern writing on a DPP8 supercooled liquid film (see below and **Figure 2.7c**), were added as foreign interfaces to induce heterogeneous nucleation (**Figure 2.9**). Therefore, heterogeneous nucleation possibility by physical contact with the shearing tool is unlikely in the shear-triggered crystallization of DPP8. It should be noted that, under heterogeneous nucleation conditions, the provided interface promotes stable nuclei formation by reducing the surface energy term (second term of Equation 1). In supercooled liquid DPP8, however, crystallization is absent even when such a rough hydrophobic interface is provided. Therefore, it is highly plausible to attribute the restricted nucleation to small ΔG between the two phases, resulting in a small driving force for crystallization (first term in Equation 1) as suggested.

Consequently, shear force is acting as a trigger for crystallization via molecular agitation in this system. Both, crystal structure and PL features of the shear-triggered crystal essentially resemble the original crystal powder of DPP8 (**Figure 2.10**). Because the crystal growth rate varies at different temperatures, the shear-triggered lighting-up crystallization propagates in a very different way depending on temperature. At 120 ^{o}C, crystallization propagated through the entire connected area of supercooled liquid and gave corresponding large fluorescence amplification even though the shear was applied only at the tip of the supercooled liquid domain (**Figure 2.7b**).[38] The shear-triggered crystallization is observed as well for the supercooled highly viscous liquid DPP8 film at 25 ^{o}C. However, the propagation of crystallization is restricted due to the limited molecular mobility at 25 ^{o}C, and thus fluorescent patterning by direct writing on the supercooled liquid DPP8 film was accomplished. In this case, only the shear-applied area showed bright greenish yellow emission (**Figure 2.7c**). In addition, the transformation between the supercooled liquid and the crystalline solid is completely reversible. Shear-triggered crystals can be transformed to supercooled liquid by simple heating over its T_m

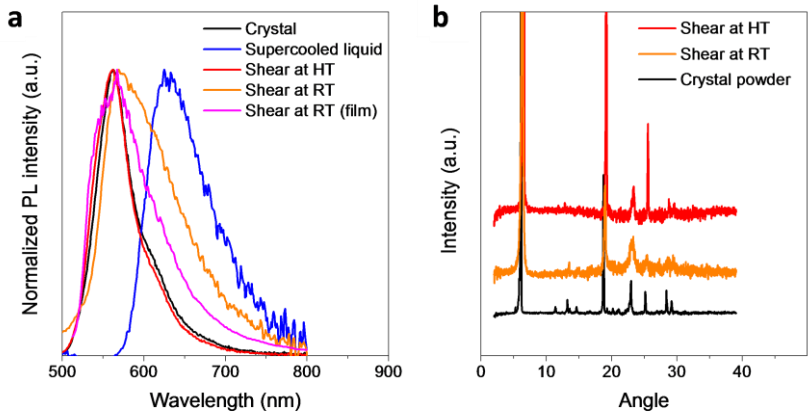

Figure 2.10 PL spectrum and X-ray diffraction (XRD) patterns of supercooled liquid, crystalline powder and shear-triggered crystal of DPP8. (a) PL spectrum. (b) XRD patterns. (HT= 120 ^{o}C, RT= 25 ^{o}C).

and subsequent cooling. Upon heating, the crystalline part disappears with vanishing bright fluorescence in a few seconds,[38] and the transformed supercooled liquid is crystallized again by applying shear force.

Unlike the mechanochromism of organic materials, this shear-triggered crystallization is a disorder-to-order transition. In this system, the applied shear force does not change an energetically favorable structure to another structure but triggers crystallization which propagates spontaneously afterwards. To test the sensitivity of the shear-triggered crystallization, we used living cells as a shear force source. When cells are seeded on a substrate, they spread and establish focal contacts on the substrate.[52] These focal adhesions transmit intracellular tension generated by the actin cytoskeleton into traction force against extracellular substrate.[53] In case of fibroblast cells, such as NIH-3T3 embryonic fibroblast and dermal fibroblast, average cell traction force (CTF) per unit area has been reported in the range of 0.1 – 0.3 kPa over compliant polyacrylamide gel,[54] but local CTF per unit area can be in the 1 – 5 kPa range.[53,55,56] In this experiment, we used HS-5 bone marrow fibroblast cells, which belong to the larger family of stromal fibroblast, seeded on DPP8 to induce local crystallization. After 2-day incubation, the HS-5 cells attached and spread over a supercooled liquid DPP8 film (**Figure 2.11a**) and produced clear greenish yellow fluorescent marks against the orange fluorescent supercooled liquid area without cells (**Figure 2.11b**). In order to visualize the alignment of cell positions relative to the greenish yellow fluorescent signals from the induced DPP8 crystals by cell adhesion, bright field image (**Figure 2.11a**) and fluorescence image (**Figure 2.11b**) were processed and merged in **Figure 2.11c**. The greenish yellow crystalline fluorescent signals were isolated from **Figure 2.11b** and labeled as green, followed by merging with grey bright field image, **Figure 2.11a**. In the resulting **Figure 2.11c**, the location of crystalline fluorescence

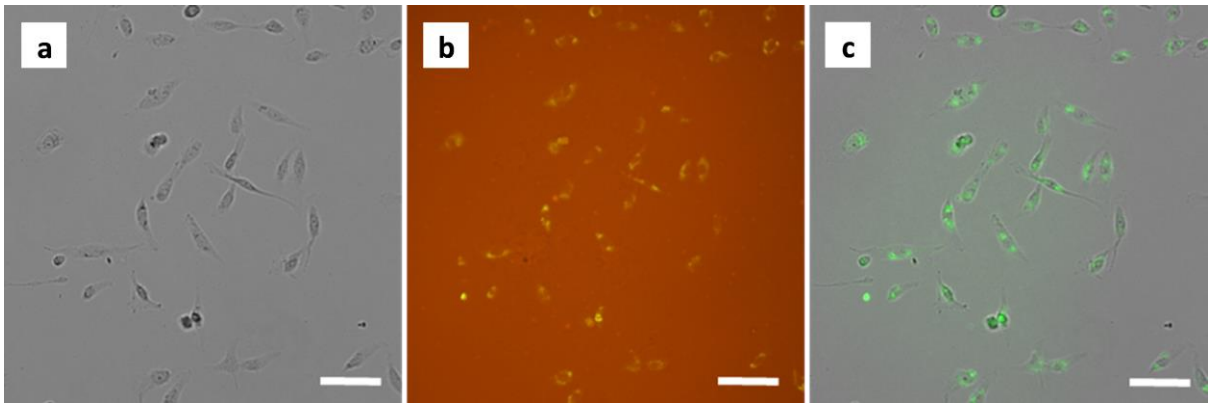

Figure 2.11 Shear-triggered crystallization by living cell attachment. (a) Bright field image and (b) Fluorescence image of HS-5 cells on the supercooled liquid DPP8 film after 2-day incubation. The background orange fluorescence in (b) originated from the supercooled liquid phase of DPP8, and traction force produced by cell focal adhesion complex on a supercooled liquid DPP8 film triggered crystallization resulting in greenish yellow fluorescence in (b). (c) In order to visualize the alignment of cell positions relative to the fluorescent signals from the induced DPP8 crystals by cell adhesion, the greenish yellow crystalline fluorescent signals were isolated from (b) and labeled as green, and overlaid with (a) (scale bar: 100 μm).

perfectly matches within the cell boundary of HS-5 cells, which demonstrates that the shear-triggered crystallization of supercooled liquid DPP8 is sensitive enough to detect cell attachment and cell contraction.[57]

In order to provide more quantitative information, we additionally conducted analysis on the threshold shear rate and shear stress of the shear-triggered crystallization by using a rheometer. In this experiment, the supercooled liquid DPP8 sample was sandwiched between two parallel plates, and the nucleation in the supercooled liquid DPP8 was examined under different applied shear rates, from 0.001 to 10 s^{-1} (shear stress from 0.03 to 273.84 kPa), at ca. 29 ^{o}C (**Figure 2.12, a and b**). Under each shear rate condition, nucleation was confirmed by observing crystallization propagation upon subsequent heating to 100 ^{o}C immediately after the shearing process. As presented in **Figure 2.12c**, the shear rates up to 0.025 s^{-1} (shear stresses up to 0.74 kPa) do not induce any crystallization but retain the thermally stable supercooled liquid phase. The nucleation in the DPP8 supercooled liquid phase is firstly confirmed at the shear rate of 0.03 s^{-1}

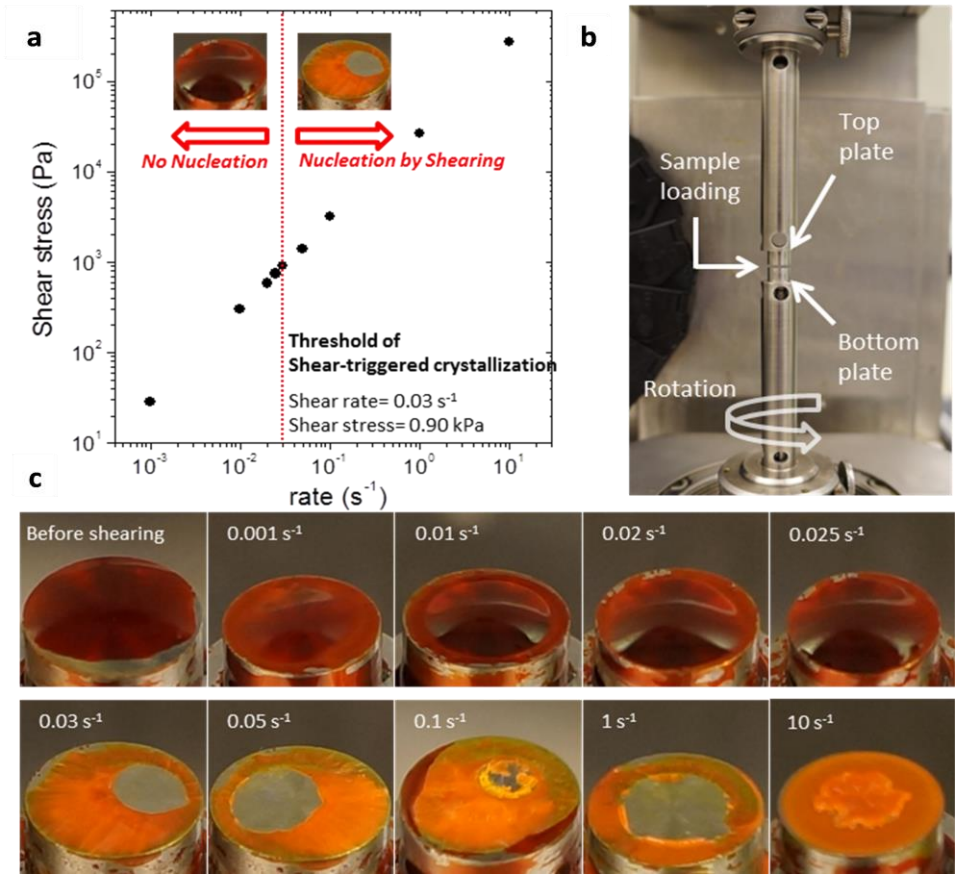

Figure 2.12 Sensitivity of the shear-triggered crystallization. (a) Applied shear rate and stress on the supercooled liquid DPP8 under a rheometer (ca. 29^{o}C). Nucleation by shearing was firstly observed at the applied shear rate of 0.03 s^{-1} (shear stress of 0.90 kPa). (b) Experimental rheometer setup to quantitatively analyze the threshold shear rate to trigger nucleation. (c) Images of DPP8 sample on the bottom plate after applying each shear rate followed by heating to 100 ^{o}C. No crystallization was observed up to the shear rate of 0.025 s^{-1} (shear stress 0.74 kPa). At the shear rate 0.03 s^{-1} and above, crystallization was clearly observed due to crystal nucleation induced by the applied shearing. Photographs (b and c) were taken under room light.

(shear stress of 0.90 kPa) by massive crystallization propagation upon subsequent heating. In the higher shear rate range (0.05 – 10 s^{-1}), shear-triggered crystallization is similarly observed. We note that this threshold shear stress value (0.90 kPa) is comparable to the fibroblast cells' traction force per unit area (1 – 5 kPa), and implies that the shear-triggered crystallization is about six orders of magnitude more sensitive than the mechanochromism observed in organic materials; in

the literatures these organic materials show color and/or fluorescence change at around 1 GPa.[35,36]

2.3. Conclusion

In summary, we have presented that a subtle force balance between core interactions and side chain interactions acting in opposite directions can be a molecular design strategy to achieve a thermally stable supercooled liquid of conjugated organic molecules. Applying shear force on the thermally stable supercooled liquid can trigger spontaneous crystallization with large optical property changes. We demonstrated these findings by investigating rationally designed DPP derivatives. A crystalline organic compound, DPP8, formed thermally stable supercooled liquid state even over a 100 ^{o}C supercooling range because of a small Gibbs free energy difference, ΔG, between its supercooled liquid and the crystalline solid states. Our investigation shows that this phenomenon is derived from a subtle force balance between aromatic core interactions and van der Waals interactions among the aliphatic side chains. The supercooled liquid DPP8 was readily transformed to its original crystal structure by means of applied shear force accompanied with 25-times fluorescence enhancement and color change. By adjusting the crystal growth rate through temperature control, we demonstrated shear-triggered fluorescent fine patterning at room temperature and propagating fluorescence amplification at 120 ^{o}C, respectively, in a completely reversible manner, which can be potentially adapted to a novel optical storage system. The lighting-up crystallization of the supercooled liquid DPP8 film by living cell attachment and spreading demonstrates the possibility of applying the phenomena to fluorescence sensor development having sensitive turn-on signaling.

2.4. Experimental Section

2.4.1. Methods

2.4.1.1. Spectroscopic Characterization

^{1}H-NMR spectrum was characterized by a Varian, Inova 500 (500 MHz) in $CDCl_3$ solution. ^{13}C-NMR spectrum was recorded on a Varian, MR400 (400 MHz) in $CDCl_3$ solution. Chemical shift values were recorded as parts per million relative to tetramethylsilane as an internal standard. Coupling constants were recorded in Hertz. Mass spectra were recorded on an Agilent Q-TOF 6520 system using electrospray in positive ion detection (ESI+) mode. Photoluminescence, absolute quantum yield and time-resolved fluorescence lifetime were obtained using PTI QuantaMasterTM spectrofluorometers equipped with an integrating sphere and a Laser excitation system. The relative fluorescence quantum yield was measured using Rhodamine 6G in ethanol as a standard reference (1×10^{-7} mol·L^{-1}, Φ_{PL} = 95%).[58] UV-visible absorption spectra were measured on a Varian Cary50 UV/Vis spectrophotometer.

2.4.1.2. Computational Details

The compounds were geometry optimized in *vacuo* by density functional theory (DFT) imposing C_i symmetry. Dimer pair calculations were done by replacing the dimer pairs of adjacent molecules in the x-ray analysis by density functional theory (DFT)-optimized ones. Vertical transition energies of the single molecules, dimer and tetramer configurations were calculated at the time-dependent (TD-)DFT level of theory. All calculations were done employing the standard B3LYP functional and 6-311G* basis set as defined in the Gaussian09 program package. Alternatively, vertical transitions were calculated by the semiempirical intermediate neglect of differential overlap (INDO) method as parameterized by Zerner for

spectroscopic applications ZINDO/S, taking into account full single configuration interaction (SCI) over the occupied and unoccupied π-type molecular orbitals (MOs).

Gaussian 09, Revision A.02, M. J. Frisch, G. W. Trucks, H. B. Schlegel, G. E. Scuseria, M. A. Robb, J. R. Cheeseman, G. Scalmani, V. Barone, B. Mennucci, G. A. Petersson, H. Nakatsuji, M. Caricato, X. Li, H. P. Hratchian, A. F. Izmaylov, J. Bloino, G. Zheng, J. L. Sonnenberg, M. Hada, M. Ehara, K. Toyota, R. Fukuda, J. Hasegawa, M. Ishida, T. Nakajima, Y. Honda, O. Kitao, H. Nakai, T. Vreven, J. A. Montgomery, Jr., J. E. Peralta, F. Ogliaro, M. Bearpark, J. J. Heyd, E. Brothers, K. N. Kudin, V. N. Staroverov, R. Kobayashi, J. Normand, K. Raghavachari, A. Rendell, J. C. Burant, S. S. Iyengar, J. Tomasi, M. Cossi, N. Rega, J. M. Millam, M. Klene, J. E. Knox, J. B. Cross, V. Bakken, C. Adamo, J. Jaramillo, R. Gomperts, R. E. Stratmann, O. Yazyev, A. J. Austin, R. Cammi, C. Pomelli, J. W. Ochterski, R. L. Martin, K. Morokuma, V. G. Zakrzewski, G. A. Voth, P. Salvador, J. J. Dannenberg, S. Dapprich, A. D. Daniels, Ö. Farkas, J. B. Foresman, J. V. Ortiz, J. Cioslowski, and D. J. Fox, Gaussian, Inc., Wallingford CT, 2009.

2.4.1.3. Cell Experiments Details

For phenyltrichlorosilane (PTS) treatment, glass substrates were cleaned by sonication in a sequence of water, acetone, chloroform and isopropanol. Cleaned glass substrates were dipped in the piranha solution for 6 min at 100 ^{o}C followed by sonication in water and isopropanol. After baking in vacuum oven (60 ^{o}C, 1 hr), substrates were under UV/O_3 treatment for 20 min (UV/Ozone ProCleaner, BioForce Nanosciences). Substrates were dipped into PTS (1.5 ml) solution in toluene (60 ml) for 30 min at 60 ^{o}C, followed by sonication in toluene and isopropanol. PTS treated substrates were stored under vacuum oven for 1 hr before spin-casting of DPP8 in chlorobenzene solution. Prepared supercooled liquid DPP8 films were annealed at

150 ^{o}C to remove residual solvents before cell seeding. Human bone marrow fibroblast (HS-5) were purchased from the American Type Culture Collection (ATCC# CRL-11882). Cells were cultured in Dulbecco's Modified Eagle's Medium (Gibco cat#11995-065) supplemented with 10% fetal bovine serum (Gibco cat#16000044) and 1% antibiotic-antimycotic (Gibco cat#15240-062). Stock culture and subsequent cell seeded samples were maintained in a humidified (100%), 37 ^{o}C, CO_2 incubator (5% CO_2, 95% air). At time of seeding, HS-5 cells were trypsinized and seeded on supercooled liquid DPP8 film at a density of ca, 10^3 cells·cm^{-2}. Prior to seeding, supercooled liquid DPP8 films were treated with fibronectin solution (10 μg·mL^{-1}) to enhance cell attachment. After 2-day incubation, cells were visualized using an Olympus BX51 microscope equipped with a UV/vis excitation system for bright field and fluorescence imaging.

2.4.1.4. Powder X-ray Diffraction and Thermal Analysis

Powder X-ray diffraction (PXRD) patterns of DPP derivatives (**Figure 2.3c**) were collected at ambient temperature using a Rigaku R-AXIS SPIDER diffractometer with an imaging plate detector using graphite monochromated Cu-Kα radiation (λ=1.54 Å). Samples were mounted on a nylon cryoloop. To obtain powder patterns with minimized preferred orientation, images were collected for 5 minutes while rotating the sample about the φ-axis at 10°·s^{-1} while oscillating ω between 120° and 180° at 1°·s^{-1} with χ set at 45°. Images were integrated in AreaMax (2.0.0.4 ed., Rigaku, 2005) software package with a step size of 0.1° to generate 2θ versus intensity data. The resulting powder patterns were processed in Jade 9+ (Ver. 9.5.0) to calculate peak positions and intensities. PXRD patterns in **Figure 2.10b** were collected at room temperature using a Rigaku rotating anode x-ray diffractometer. Powder samples were securely placed into a special quartz holder. Cu-Kα radiation (λ=1.54 Å) source generated from a 12 kW Rigaku rotating

anode generator that was operated at 40 kV and 100 mA. The powder diffraction profiles were measured in the 2θ range from 2º to 40º (step size 0.02º). The resulting powder patterns were analyzed using Origin software (OriginPro 8, OriginLab Corp., Northampton, MA, USA) to define peak positions and intensities. The thermal properties of samples were measured using differential scanning calorimetry (DSC) of TA Instruments Discovery DSC (**Figure 2.2** and **Figure 2.3d**) and Perkin Elmer DSC7 (**Figure 2.3a** and **Figure 2.5**).

2.4.1.5. Single Crystal Structure Analysis for DPP8

Orange blocks of DPP8 were grown from an acetonitrile solution of the compound at 23 ^{o}C. A crystal of dimensions 0.14 × 0.10 × 0.02 mm was mounted on a Rigaku AFC10K Saturn 944+ CCD-based X-ray diffractometer equipped with a low temperature device and Micromax-007HF Cu-target micro-focus rotating anode (λ =1.54187 Å) operated at 1.2 kW power (40 kV, 30 mA). The X-ray intensities were measured at 85(1) K with the detector placed at a distance 42.00 mm from the crystal. A total of 4224 images were collected with an oscillation width of 1.0^{o} in ω. The exposure time was 5 sec. for the low angle images, 35 sec. for high angle. The integration of the data yielded a total of 92579 reflections to a maximum 2θ value of 136.48^{o} of which 5914 were independent and 5496 were greater than 2σ(I). The final cell constants (**Table 2.2**) were based on the xyz centroids 55569 reflections above 10σ(I). Analysis of the data showed negligible decay during data collection; the data were processed with CrystalClear 2.0 and corrected for absorption. The structure was solved and refined with the Bruker SHELXTL (version 2008/4) software package, using the space group P2(1)/c with Z = 4 for the formula $C_{34}H_{42}N_2O_2Br_2$. All non-hydrogen atoms were refined anisotropically with the hydrogen atoms placed in idealized positions. Full matrix least-squares refinement based on F^2 converged at R_1 =

0.0431 and wR_2 = 0.1090 [based on I > 2σ(I)], R_1 = 0.0453 and wR_2 = 0.1107 for all data. Additional details are presented in **Table 2.2.**

Sheldrick, G.M. SHELXTL, v. 2008/4; Bruker Analytical X-ray, Madison, WI, 2008.

CrystalClear Expert 2.0 r12, Rigaku Americas and Rigaku Corporation (2011), Rigaku Americas, 9009, TX, USA 77381-5209, Rigaku Tokyo, 196-8666, Japan.

Table 2.2 Crystal data and structure refinement for DPP8

Identification code	DPP8
Empirical formula	$C_{34}H_{42}Br_2N_2O_2$
Formula weight	670.52
Temperature	85(2) K
Wavelength	1.54178 Å
Crystal system, space group	Monoclinic, P2(1)/c
Unit cell dimensions	a = 8.9169(2) Å alpha = 90 deg.
	b = 13.1897(2) Å beta = 92.083(7) deg.
	c = 27.4851(19) Å gamma = 90 deg.
Volume	3230.4(2) $Å^3$
Z, Calculated density	4, 1.379 Mg/m^3
Absorption coefficient	3.422 mm^{-1}
F(000)	1384
Crystal size	0.14 x 0.10 x 0.02 mm
Theta range for data collection	3.72 to 68.24 deg.
Limiting indices	-10<=h<=10, -15<=k<=15, -32<=l<=33
Reflections collected / unique	92579 / 5914 [R(int) = 0.0834]
Completeness to theta = 68.24	100.00%
Absorption correction	Semi-empirical from equivalents
Max. and min. transmission	0.934 and 0.703
Refinement method	Full-matrix least-squares on F^2
Data / restraints / parameters	5914 / 0 / 363
Goodness-of-fit on F^2	1.072
Final R indices [I > 2σ(I)]	R_1 = 0.0431, wR_2 = 0.1090
R indices (all data)	R_1 = 0.0453, wR_2 = 0.1107
Largest diff. peak and hole	1.097 and -1.195 $e.A^{-3}$

2.4.1.6. Single Crystal Structure Analysis for DPP4

Orange prismatic crystals of DPP4 were grown from an ethanol solution of the compound at 22 ^{o}C. A crystal of dimensions 0.14 × 0.09 × 0.08 mm was mounted on a Rigaku AFC10K Saturn 944+ CCD-based X-ray diffractometer equipped with a low temperature device and Micromax-007HF Cu-target micro-focus rotating anode (λ=1.54187 A) operated at 1.2 kW power (40 kV, 30 mA). The X-ray intensities were measured at 85(1) K with the detector placed at a distance 42.00 mm from the crystal. A total of 4031 images were collected with an oscillation width of 1.0^{o} in ω. The exposure time was 2 sec. for the low angle images, 12 sec. for high angle. The integration of the data yielded a total of 66066 reflections to a maximum 2θ value of 136.44^{o} of which 4382 were independent and 4207 were greater than 2σ(I). The final cell constants (**Table 2.3**) were based on the xyz centroids 47236 reflections above 10σ(I). Analysis of the data showed negligible decay during data collection; the data were processed with CrystalClear 2.0 and corrected for absorption. The structure was solved and refined with the Bruker SHELXTL (version 2008/4) software package, using the space group I2/a with Z = 8 for the formula $C_{26}H_{26}N_2O_2Br_2$. All non-hydrogen atoms were refined anisotropically with the hydrogen atoms placed in idealized positions. Full matrix least-squares refinement based on F^2 converged at R_1 = 0.0241 and wR_2 = 0.0641 [based on I > 2σ(I)], R_1 = 0.0249 and wR_2 = 0.0649 for all data. Additional details are presented in **Table 2.3**.

Table 2.3 Crystal data and structure refinement for DPP4

Identification code	**DPP4**
Empirical formula	**$C_{26}H_{26}Br_2N_2O_2$**
Formula weight	**558.31**
Temperature	**85(2) K**
Wavelength	**1.54178 Å**
Crystal system, space group	**Monoclinic, I2/a**
Unit cell dimensions	**a = 15.3997(3) Å alpha = 90 deg.**
	b = 18.3154(3) Å beta = 91.348(6) deg.
	c = 16.9365(12) Å gamma = 90 deg.
Volume	**4775.6(4) $Å^3$**
Z, Calculated density	**8, 1.553 Mg/m^3**
Absorption coefficient	**4.508 mm^{-1}**
F(000)	**2256**
Crystal size	**0.14 x 0.09 x 0.08 mm**
Theta range for data collection	**3.55 to 68.22 deg.**
Limiting indices	**-18<=h<=18, -22<=k<=21, -20<=l<=20**
Reflections collected / unique	**66066 / 4382 [R(int) = 0.0550]**
Completeness to theta = 68.22	**100.00%**
Absorption correction	**Semi-empirical from equivalents**
Max. and min. transmission	**0.7144 and 0.5710**
Refinement method	**Full-matrix least-squares on F^2**
Data / restraints / parameters	**4382 / 0 / 291**
Goodness-of-fit on F^2	**1.058**
Final R indices [$I > 2\sigma(I)$]	**$R_1 = 0.0241, wR_2 = 0.0641$**
R indices (all data)	**$R_1 = 0.0249, wR_2 = 0.0649$**
Largest diff. peak and hole	**0.343 and -0.485 $e.A^{-3}$**

2.4.1.7. Free Energy Difference

ΔG between supercooled liquid and crystalline solid of DPP8 was calculated with three different methods; i.e. by [1] relative solubility measurement,[39] [2] via the Hoffman equation,[40] [3] via a thermodynamic cycle (Hess's law) using Kirchhoff's law inserting the heat capacity (C_p) of supercooled liquid and crystalline solid (**Figure 2.6**).

[1] Relative solubility measurements were performed in a previously described manner.[39] The optical absorbance of supercooled liquid and crystal powder in water and methanol mixture solvent (1:7) was measured using Varian Cary50 UV/Vis spectrophotometer. By monitoring the time-dependent absorbance curve, the absorbance at equilibrium was determined. At equilibrium, the ratio of absorption intensity represents equilibrium constant (K_{eq}) in the following equation: $\Delta G = -RT(\ln K_{eq})$. R is gas constant and T is temperature in Kelvin. Inserting K_{eq}=2.883, the calculated ΔG between supercooled liquid state and crystalline solid state is ΔG= -2.63 kJ·mol^{-1} (-0.63 kcal·mol^{-1}) at 26 ^{o}C. This free energy difference may represent a slight underestimation due to a conversion of supercooled liquid to crystal form under the experimental conditions.

[2] The Hoffmann equation, $\Delta G = \Delta H_f(T_m-T)T \cdot T_m^{-2}$, was used for the calculation of ΔG between the two phases of DPP8.[40] T_m = 133.62 ^{o}C and ΔH_f =29.13 kJ·mol^{-1} were measured by means of Discovery DSC, to give ΔG = -5.67 kJ·mol^{-1} (-1.35 kcal·mol^{-1}) at 26 ^{o}C. This value may slightly deviate from the real value because heat capacity is not considered in the equation.[59]

[3] ΔG was calculated via a thermodynamic cycle (Hess's law) using $\Delta G = \Delta H - T\Delta S$ and Kirchhoff's law by inserting the C_p of the supercooled liquid and the crystalline solid. The calculation procedure is presented in **Figure 2.6**. The calculated ΔG = -6.24 kJ·mol^{-1} (-1.49 kcal·mol^{-1}) at 26 ^{o}C may be slightly overestimated due to additional heat capacity contribution from 388 K (115 ^{o}C) to melting temperature 407 K (134 ^{o}C).

2.4.1.8. Sonication-Triggered Nucleation

A probe sonicator controlled by Cole Parmer ultrasonic processor and a vial having supercooled liquid DPP8 on the bottom were placed in a water bath as shown in **Figure 2.13**. Sonication was conducted for 10 minutes at 29 ^{o}C. To reduce temperature increase of water bath

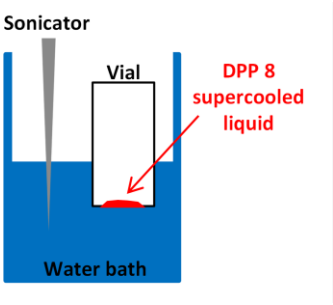

Figure 2.13 Schematic illustration of the sonication experiment setting in order to verify molecular agitation effect on nucleation and crystallization of supercooled liquid DPP8.

by sonication, sonicator was stopped for 20 sec after every 40 sec sonication. After sonication, the temperature of the water bath was 31 ^{o}C. Supercooled liquid sample treated under sonication was annealed on a hot plate (120 ^{o}C) for 5 minutes and observed under 365 nm UV light to examine nucleation and crystallization.

2.4.1.9. Heterogeneous Nucleation Test

Sea sand (Fisher Sci.), rubber powders (eraser), or polyimide film (Kapton film, CS Hyde Company) was mixed with molten DPP8 on a glass substrate. To check heterogeneous nucleation and crystallization propagation, the sample was cooled down to room temperature and subsequently heated to 120 ^{o}C. After holding at 120 ^{o}C for 5 minutes, a fluorescence image of the sample was taken. During the whole process the sample was observed using an Olympus BX51 microscope equipped with a UV/vis excitation system for bright field and fluorescence imaging.

2.4.1.10. Sensitivity of Shear-Triggered Crystallization

Threshold shear rate and shear stress were characterized using ARES Rheometer (TA instruments) equipped with an air forced convection oven. DPP8 crystalline powder was sandwiched between 8 mm diameter parallel plates, and melted at 150 ^{o}C. After cooling down to room temperature, the gap between the two plates was finely adjusted to fill the space between

the two plates completely. Under each shear rate from 0.001 to 10 s^{-1}, steady single point test was conducted and corresponding applied shear stress was measured, followed by heating to 100 ^{o}C to confirm nucleation by the shearing. Photographs were taken after subsequent heating under room light.

2.4.2. Materials and Synthesis

All starting materials and solvents for the synthesis were purchased from commercial suppliers (Sigma-Aldrich Chemical Co. and Fisher Sci.).

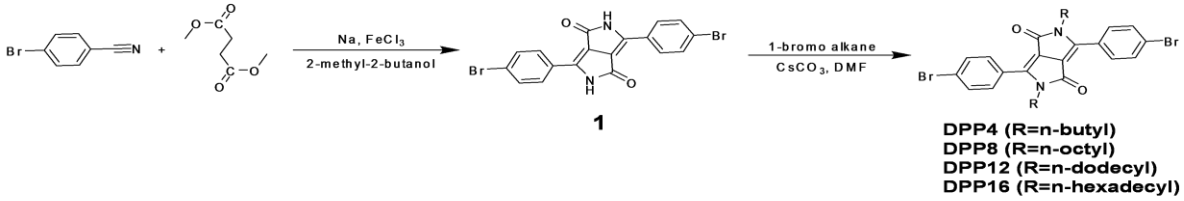

Figure 2.14 Synthetic route of DPP derivatives.

2.4.2.1. Synthesis of 3,6-bis(4-bromophenyl)pyrrolo[3,4-c]pyrrole-1,4(2H,5H)-dione [1]

Synthesis of [1] was performed in a previously described manner.[60] Under Ar condition, Sodium (1.26 g, 54.94 mmol) and $FeCl_3$ (0.06 g) was added to dry 2-methyl-2-butanol (27.5 ml) (at room temperature), and the mixture was stirred at 90 ^{o}C. After Sodium is completely dissolved, 4-bromobenzonitrile (5 g, 27.47 mmol) was added at 50 ^{o}C. At 90 ^{o}C, dimethyl succinate (2.22 g, 10.99 mmol) in 11.5 ml of 2-methyl-2-butanol was added drop wise. The mixture was stirred at 90 ^{o}C for 24 hr. Acetic acid (11.5 ml) was added drop wise to the mixture and was stirred at 120 ^{o}C for 1hr. The reaction mixture was cooled down to room temperature

and filtered. The filtered dark red solid was washed with hot water and hot methanol several times and used for next reaction without further purification. Product 2.29 g, (47%).

2.4.2.2. Synthesis of 3,6-bis(4-bromophenyl)-2,5-dioctylpyrrolo[3,4-c]pyrrole-1,4(2H,5H)-dione (DPP8)

Under Ar condition, 3,6-bis(4-bromophenyl)pyrrolo[3,4-c]pyrrole-1,4(2H,5H)-dione (1 g, 2.24 mmol), Cs_2CO_3 (2.191 g, 6.72 mmol) and 1-bromooctane (1.73 g, 8.97 mmol) was added in dry dimethylformamide (25 ml). The mixture was stirred at 40 ^oC for 24 hr. After cooling to room temperature, the mixture was poured into water and extracted with chloroform. The organic phase was dried over $MgSO_4$ and the solvent was evaporated in *vacuo*. Column chromatography (dichloromethane as eluent) and multiple recrystallizations (methanol or ethanol) were performed. Orange crystal of DPP8 was obtained. Product 0.65 g (43%). ^1H NMR (500 MHz, CDCl3): δ 7.71 – 7.65 (m, 8 H), 3.72 (t, J=9.3 Hz, 4 H), 1.58 (m, 4H), 1.26 – 1.19 (m, 20H), 0.86 (t, J=8.4 Hz, 6 H). ^{13}C NMR (400 MHz, CDCl3): δ 162.6, 147.6, 132.3, 130.3, 127.1, 126.0, 110.0, 42.0, 31.9, 29.5, 29.3, 29.2, 26.8, 22.8, 14.3. MS m/z (ESI+, relative intensity): 671 (M^++1, 100), 520 (6), 409 (19), 312 (25). HRMS (ESI+) calcd. for $C_{34}H_{42}Br_2N_2O_2$ (M^++1) 669.1686, found 669.1665.

2.4.2.3. Synthesis of 3,6-bis(4-bromophenyl)-2,5-dibutylpyrrolo[3,4-c]pyrrole-1,4(2H,5H)-dione (DPP4)

Same procedure with DPP8 was performed. Replacing 1-bromooctane, 1-bromobutane was used. Product 0.46 g (37%). ^1H NMR (500 MHz, CDCl3): δ 7.71 – 7.65 (m, 8 H), 3.74 (t, J=9.3 Hz, 4 H), 1.56 (m, 4H), 1.29 – 1.23 (m, 4H), 0.85 (t, J=9.0 Hz, 6 H). ^{13}C NMR (400 MHz,

CDCl3): δ 162.5, 147.6, 132.3, 130.3, 127.0, 126.0, 110.0, 41.7, 31.6, 20.1, 13.8. MS m/z (ESI+, relative intensity): 559 (M^++1, 100), 409 (5). HRMS (ESI+) calcd. for $C_{26}H_{26}Br_2N_2O_2$ (M^++1) 557.0434, found 557.0424.

2.4.2.4. Synthesis of 3,6-bis(4-bromophenyl)-2,5-didodecylpyrrolo[3,4-c]pyrrole-1,4(2H,5H)-dione (DPP12)

Same procedure with DPP8 was performed. Replacing 1-bromooctane, 1-bromododecane was used. Product 0.52 g (30%). ^{1}H NMR (500 MHz, CDCl3): δ 7.71 – 7.65 (m, 8 H), 3.72 (t, J=9.0 Hz, 4 H), 1.56 (m, 4H), 1.29 – 1.19 (m, 36H), 0.88 (t, J=8.4 Hz, 6 H). ^{13}C NMR (400 MHz, CDCl3): δ 162.6, 147.6, 132.4, 130.3, 127.1, 126.0, 110.0, 42.0, 32.1, 29.8, 29.7, 29.6, 29.5, 29.2, 26.9, 22.9, 14.3. MS m/z (ESI+, relative intensity): 783 (M^++1, 45), 576 (23), 409 (100), 298 (24), 186 (19). HRMS (ESI+) calcd. for $C_{42}H_{58}Br_2N_2O_2$ (M^++1) 781.2938, found 781.2911.

2.4.2.5. Synthesis of 3,6-bis(4-bromophenyl)-2,5-dihexadecylpyrrolo[3,4-c]pyrrole-1,4(2H,5H)-dione (DPP16)

Same procedure with DPP8 was performed. Replacing 1-bromooctane, 1-bromohexadecane was used. Product 0.56 g (28%). ^{1}H NMR (500 MHz, CDCl3): δ 7.71 – 7.65 (m, 8 H), 3.72 (t, J=9.3 Hz, 4 H), 1.56 (m, 4H), 1.30 – 1.19 (m, 52H), 0.88 (t, J=8.4 Hz, 6 H). ^{13}C NMR (400 MHz, CDCl3): δ 162.6, 147.6, 132.4, 130.3, 127.1, 126.0, 110.1, 42.0, 32.1, 29.9, 29.9, 29.8, 29.7, 29.6, 29.6, 29.2, 26.9, 22.9, 14.3. MS m/z (ESI+, relative intensity): 895 (M^++1, 49), 752 (28), 708 (45), 664 (57), 576 (68), 532 (60), 488 (38), 408 (100), 298 (66), 242 (85). HRMS (ESI+) calcd. for $C_{50}H_{74}Br_2N_2O_2$ (M^++1) 893.4190, found 893.4166.

2.5. Author Contribution

K. Chung, M. S. Kwon, B. M. Leung, A. G. Wong-Foy, M. S. Kim, J. Kim, S. Takayama, J. Gierschner, A. J. Matzger, J. Kim, Shear-Triggered Crystallization and Light Emission of a Thermally Stable Organic Supercooled Liquid. *ACS Cent. Sci.* **1**, 94–102 (2015)

Kyeongwoon Chung and Jinsang Kim designed the project, and Jinsang Kim directed the project. Kyeongwoon Chung and Min Sang Kwon synthesized the series of molecules. Optical, thermal, and crystallization property analyses on the molecules were conducted by Kyeongwoon Chung and partly by Min Sang Kwon, Min Su Kim and Jeongyong Kim. Kyeongwoon Chung, Brendan M. Leung and Shuichi Takayama performed cell experiments. Antek G. Wong-Foy and Adam J. Matzger performed X-ray measurements and analysis. Johannes Gierschner analyzed the photophysical properties with help of TD-DFT calculations. Kyeongwoon Chung and Jinsang Kim wrote the manuscript for publication, and all other authors had input.

2.6. References and Notes

1. K. Naito, A. Miura, Molecular design for nonpolymeric organic dye glasses with thermal stability: relations between thermodynamic parameters and amorphous properties. *J. Phys. Chem.* **97,** 6240–6248 (1993).
2. P. G. Debenedetti, F. H. Stillinger, Supercooled liquids and the glass transition. *Nature* **410,** 259–267 (2001).
3. L. Chen, G. Dong, L. Duan, L. Wang, J. Qiao, D. Zhang, Y. Qiu, Liquid-Formed Glassy Film of N,N’-Diphenyl-N,N'-bis(3-methylphenyl)benzidine: Formation, Carrier Transporting Ability, Photoluminescence, and Stability. *J. Phys. Chem. C* **111,** 18376–18380 (2007).
4. A. C. Arias, J. D. MacKenzie, I. McCulloch, J. Rivnay, A. Salleo, Materials and applications for large area electronics: solution-based approaches. *Chem. Rev.* **110,** 3–24 (2010).
5. N. Okamoto, M. Oguni, Discovery of crystal nucleation proceeding much below the glass transition temperature in a supercooled liquid. *Solid State Commun.* **99,** 53–56 (1996).
6. N. Okamoto, M. Oguni, Y. Sagawa, Generation and extinction of a crystal nucleus below the glass transition temperature. *J. Phys. Condens. Matter* **9,** 9187–9198 (1997).
7. J. A. Baird, B. Van Eerdenbrugh, L. S. Taylor, A classification system to assess the

crystallization tendency of organic molecules from undercooled melts. *J. Pharm. Sci.* **99,** 3787–3806 (2010).
8. C. M. Whitaker, R. J. McMahon, Synthesis and Characterization of Organic Materials with Conveniently Accessible Supercooled Liquid and Glassy Phases: Isomeric 1,3,5-Tris(naphthyl)benzenes. *J. Phys. Chem.* **100,** 1081–1090 (1996).
9. N. C. Greenham, R. H. Friend, Semiconductor Device Physics of Conjugated Polymers. *Solid State Phys.* **49,** 1–149 (1996).
10. J. G. C. Veinot, T. J. Marks, Toward the ideal organic light-emitting diode. The versatility and utility of interfacial tailoring by cross-linked siloxane interlayers. *Acc. Chem. Res.* **38,** 632–643 (2005).
11. L. Duan, L. Hou, T.-W. Lee, J. Qiao, D. Zhang, G. Dong, L. Wang, Y. Qiu, Solution processable small molecules for organic light-emitting diodes. *J. Mater. Chem.* **20,** 6392–6407 (2010).
12. B. C. Hancock, M. Parks, What is the True Solubility Advantage for Amorphous Pharmaceuticals? *Pharm. Res.* **17,** 397–404 (2000).
13. M. D. Ediger, C. A. Angell, S. R. Nagel, Supercooled Liquids and Glasses. *J. Phys. Chem.* **100,** 13200–13212 (1996).
14. L.-M. Wang, C. A. Angell, R. Richert, Fragility and thermodynamics in nonpolymeric glass-forming liquids. *J. Chem. Phys.* **125,** 074505 (2006).
15. S. M. Dounce, J. Mundy, H.-L. Dai, Crystallization at the glass transition in supercooled thin films of methanol. *J. Chem. Phys.* **126,** 191111 (2007).
16. T. Hecksher, A. I. Nielsen, N. B. Olsen, J. C. Dyre, Little evidence for dynamic divergences in ultraviscous molecular liquids. *Nat. Phys.* **4,** 737–741 (2008).
17. O. Wallquist, R. Lenz, 20 years of DPP pigments – future perspectives. *Macromol. Symp.* **187,** 617–630 (2002).
18. Y. Li, P. Sonar, L. Murphy, W. Hong, High mobility diketopyrrolopyrrole (DPP)-based organic semiconductor materials for organic thin film transistors and photovoltaics. *Energy Environ. Sci.* **6,** 1684–1710 (2013).
19. D. Chandran, K.-S. Lee, Diketopyrrolopyrrole: A versatile building block for organic photovoltaic materials. *Macromol. Res.* **21,** 272–283 (2013).
20. B. Ackerson, P. Pusey, Shear-Induced Order in Suspensions of Hard Spheres. *Phys. Rev. Lett.* **61,** 1033–1036 (1988).
21. R. Amos, J. Rarity, P. Tapster, T. Shepherd, S. Kitson, Fabrication of large-area face-centered-cubic hard-sphere colloidal crystals by shear alignment. *Phys. Rev. E* **61,** 2929–2935 (2000).
22. A. V. Mokshin, J.-L. Barrat, Shear-induced crystallization of an amorphous system. *Phys. Rev. E* **77,** 021505 (2008).
23. S. Karasawa, R. Hagihara, Y. Abe, N. Harada, J. Todo, N. Koga, Crystal Structures, Thermal Properties, and Emission Behaviors of N , N -R-Phenyl-7-amino-2,4-trifluoromethylquinoline Derivatives: Supercooled Liquid-to-Crystal Transformation Induced by Mechanical Stimuli. *Cryst. Growth Des.* **14,** 2468–2478 (2014).
24. T. Palberg, W. Mönch, J. Schwarz, P. Leiderer, Grain size control in polycrystalline colloidal solids. *J. Chem. Phys.* **102,** 5082 (1995).
25. T. Okubo, H. Ishiki, Kinetic Analyses of Colloidal Crystallization in a Wide Range of Sphere Concentrations as Studied by Reflection Spectroscopy. *J. Colloid Interface Sci.*

228, 151–156 (2000).
26. R. Blaak, S. Auer, D. Frenkel, H. Löwen, Crystal Nucleation of Colloidal Suspensions under Shear. *Phys. Rev. Lett.* **93,** 068303 (2004).
27. D. T. Grubb, A. Keller, Crystallization induced by simple shear of molten isotactic polystyrene. *J. Polym. Sci. Polym. Lett. Ed.* **12,** 419–425 (1974).
28. T C. Tribout, B. Monasse, J. M. Haudin, Experimental study of shear-induced crystallization of an impact polypropylene copolymer. *Colloid Polym. Sci.* **274,** 197–208 (1996).
29. R. H. Somani, L. Yang, L. Zhu, B. S. Hsiao, Flow-induced shish-kebab precursor structures in entangled polymer melts. *Polymer* **46,** 8587–8623 (2005).
30. Y. Sagara, T. Kato, Mechanically induced luminescence changes in molecular assemblies. *Nat. Chem.* **1,** 605–610 (2009).
31. X. Luo, J. Li, C. Li, L. Heng, Y. Q. Dong, Z. Liu, Z. Bo, B. Z. Tang, Reversible switching of the emission of diphenyldibenzofulvenes by thermal and mechanical stimuli. *Adv. Mater.* **23,** 3261–3265 (2011).
32. M. S. Kwon, J. Gierschner, S.-J. Yoon, S. Y. Park, Unique piezochromic fluorescence behavior of dicyanodistyrylbenzene based donor-acceptor-donor triad: mechanically controlled photo-induced electron transfer (eT) in molecular assemblies. *Adv. Mater.* **24,** 5487–5492 (2012).
33. S.-J. Yoon, J. W. Chung, J. Gierschner, K. S. Kim, M.-G. Choi, D. Kim, S. Y. Park, Multistimuli two-color luminescence switching via different slip-stacking of highly fluorescent molecular sheets. *J. Am. Chem. Soc.* **132,** 13675–83 (2010).
34. Z.-H. Guo, Z.-X. Jin, J.-Y. Wang, J. Pei, A donor-acceptor-donor conjugated molecule: twist intramolecular charge transfer and piezochromic luminescent properties. *Chem. Commun.* **50,** 6088–6090 (2014).
35. Y. Dong, B. Xu, J. Zhang, X. Tan, L. Wang, J. Chen, H. Lv, S. Wen, B. Li, L. Ye, B. Zou, W. Tian, Piezochromic luminescence based on the molecular aggregation of 9,10-bis((E)-2-(pyrid-2-yl)vinyl)anthracene. *Angew. Chem. Int. Ed. Engl.* **51,** 10782–5 (2012).
36. C. H. Woodall, S. K. Brayshaw, S. Schiffers, D. R. Allan, S. Parsons, R. Valiente, P. R. Raithby, High-pressure crystallographic and spectroscopic studies on two molecular dithienylethene switches. *CrystEngComm* **16,** 2119–2128 (2014).
37. F. F. Abraham, *Homogeneous Nucleation Theory*. (Academic Press, New York, 1974).
38. See the supporting movies; K. Chung, M. S. Kwon, B. M. Leung, A. G. Wong-Foy, M. S. Kim, J. Kim, S. Takayama, J. Gierschner, A. J. Matzger, J. Kim, Shear-Triggered Crystallization and Light Emission of a Thermally Stable Organic Supercooled Liquid. *ACS Cent. Sci.* **1,** 94–102 (2015).
39. V. López-Mejías, J. W. Kampf, A. J. Matzger, Polymer-induced heteronucleation of tolfenamic acid: structural investigation of a pentamorph. *J. Am. Chem. Soc.* **131,** 4554–4555 (2009).
40. J. D. Hoffman, Thermodynamic Driving Force in Nucleation and Growth Processes. *J. Chem. Phys.* **29,** 1192 (1958).
41. A. Cembran, F. Bernardi, M. Garavelli, L. Gagliardi, G. Orlandi, On the mechanism of the cis-trans isomerization in the lowest electronic states of azobenzene: S0, S1, and T1. *J. Am. Chem. Soc.* **126,** 3234–3243 (2004).
42. In the crystallization experiment of DPP12, supercooled liquid DPP12 exhibit similar

shear-triggered crystallization at 85 ^{o}C compared to DPP8. See Figure 2.1a for the fluorescence image of shear-triggered DPP12.
43. J. Gierschner, S. Y. Park, Luminescent distyrylbenzenes: tailoring molecular structure and crystalline morphology. *J. Mater. Chem. C* **1,** 5818–5832 (2013).
44. H.-J. Egelhaaf, J. Gierschner, D. Oelkrug, Polarizability effects and energy transfer in quinquethiophene doped bithiophene and OPV films. *Synth. Met.* **127,** 221–227 (2002).
45. Absorption spectra of the crystalline solid could not be obtained because of the inhomogeneity of the samples.
46. It should be noted however, that for such weakly coupled systems, quantum-chemical calculations are usually ambiguous; thus, the results will depend sensitively on the method applied.
47. J. Gierschner, L. Lüer, B. Milián-Medina, D. Oelkrug, H.-J. Egelhaaf, Highly Emissive H-Aggregates or Aggregation-Induced Emission Quenching? The Photophysics of All-Trans para -Distyrylbenzene. *J. Phys. Chem. Lett.* **4,** 2686–2697 (2013).
48. J. Gierschner, H.-G. Mack, D. Oelkrug, I. Waldner, H. Rau, Modeling of the Optical Properties of Cofacial Chromophore Pairs: Stilbenophane. *J. Phys. Chem. A* **108,** 257–263 (2004).
49. J. L. Gay-Lussac, De l' influence de la pression de l' air sur la cristallisation des sels. *Ann. Chim.* **87,** 225–236 (1813).
50. L Y.-X. Liu, X.-J. Wang, J. Lu, C.-B. Ching, Influence of the roughness, topography, and physicochemical properties of chemically modified surfaces on the heterogeneous nucleation of protein crystals. *J. Phys. Chem. B* **111,** 13971–13978 (2007).
51. Y. Zhang, M. Wang, X. Lin, W. Huang, Effect of Substrate Surface Microstructure on Heterogeneous Nucleation Behavior. *J. Mater. Sci. Technol.* **28,** 67–72 (2012).
52. M. Chrzanowska-Wodnicka, K. Burridge, Rho-stimulated contractility drives the formation of stress fibers and focal adhesions. *J. Cell Biol.* **133,** 1403–1415 (1996).
53. J. L. Tan, J. Tien, D. M. Pirone, D. S. Gray, K. Bhadriraju, C. S. Chen, Cells lying on a bed of microneedles: an approach to isolate mechanical force. *Proc. Natl. Acad. Sci. U. S. A.* **100,** 1484–1489 (2003).
54. J. Chen, H. Li, N. SundarRaj, J. H.-C. Wang, Alpha-smooth muscle actin expression enhances cell traction force. *Cell Motil. Cytoskeleton* **64,** 248–257 (2007).
55. C. A. Reinhart-King, M. Dembo, D. A. Hammer, D. A. Endothelial Cell Traction Forces on RGD-Derivatized Polyacrylamide Substrate. *Langmuir* **19,** 1573–1579 (2003).
56. N. Q. Balaban, U. S. Schwarz, D. Riveline, P. Goichberg, G. Tzur, I. Sabanay, D. Mahalu, S. Safran, A. Bershadsky, L. Addadi, B. Geiger, Force and focal adhesion assembly: a close relationship studied using elastic micropatterned substrates. *Nat. Cell Biol.* **3,** 466–472 (2001).
57. We note that the suggested CTF of fibroblast cells may be underestimated compared to the CTF in our experimental condition because experiments in literatures were performed on deformable substrates, and because, even within the same cell type, the exerted CTF on a substrate may increase as the substrate stiffness increase. See reference: L. Qin, H. K. Genant, J. F. Griffith, K. S. Leung, *Advanced Bioimaging Technologies in Assessment of the Quality of Bone and Scaffold Materials*. pp 227-235 (Springer, Berlin Heidelberg, 2007).
58. R. F. Kubin, A. N. Fletcher, Fluorescence quantum yields of some rhodamine dyes. *J.*

Lumin. **27,** 455–462 (1982).
59. V. Andronis, G. Zografi, Crystal nucleation and growth of indomethacin polymorphs from the amorphous state. *J. Non. Cryst. Solids* **271,** 236–248 (2000).
60. G. Zhang, K. Liu, Y. Li, M. Yang, Novel poly(phenylene ethynylene)-type conjugated polymers containing diketopyrrolopyrrole or triphenylpyrazoline units in the main chain: synthesis, characterization and photophysical properties. *Polym. Int.* **58,** 665–673 (2009).

CHAPTER 3

Designing Interchain and Intrachain Properties of Conjugated Polymers for Latent Optical Information Encoding

Chemical Science, **6**, 6980-6985 (2015) – Published by The Royal Society of Chemistry

3.1. Introduction

Insightful molecular design consideration to interchain properties realized through molecular packing as well as intrinsic intrachain properties is highly demanding yet inevitable to fully utilize conjugated polymers' optoelectronic properties in the solid state. In this chapter, unique latent optical information encoding through a straightforward and effective conjugated polymer (CP) design strategy for security ink application is demonstrated.

CPs are key materials for various optoelectronic applications, including chemical and bio sensors[1–9] that detect from ions, biomolecules to dangerous chemical gases, and security inks[10–12] for hidden information delivery or anti-counterfeiting. The optoelectronic properties of CPs are determined by both the intrachain (intrinsic) and the interchain (packing) properties of the polymer chains. While the intrachain properties are mainly determined by the chemical structure of the main chain, the interchain properties are driven by the polymer packing, which is influenced by various design factors. Therefore, the rational design of both the intrachain and the

interchain properties of CPs is important for realizing CP applications with optimal characteristics.

Various strategies for regulating the intrachain properties of CPs through the design of the conjugated main chain have been investigated, including atom substitution,[13–15] addition of functional groups,[16,17] and the modification of CP building blocks.[18,19] These main chain design strategies also partly affect the interchain properties of CPs: for example, introducing planar building blocks and linkages, such as thiophene linked diketopyrrolopyrrole (DPP), promote close co-facial packing of CPs' main chain, which results in enhanced hole mobility in CP films.[13]

However, unlike the widely investigated main chain design of CPs, the effects of flexible side chains on the interpolymer assembly and packing are rather unexplored. Flexible side chains are often introduced mainly to provide solubility to the rigid-rod like CPs. For this purpose, long and branched side chains are usually adapted into CPs without a thorough consideration of their effects on the interchain packing. However, recent work has emphasized the role of the side chain and discusses it as an important design parameter to tune the properties of CPs. For instance, by investigating different side chains on the same conjugated main chain backbone, the side chain design has proven to be critical to the interchain properties.[20–23] Our research group recently showed an increase in hole mobility of three orders of magnitude in aligned lyotropic liquid crystalline CPs by rationally designing the molecular architecture of side chains together with the main chain conformation and form factor, which rendered directed self-assembly and packing of CPs.[24] Therefore, the optimization of CP characteristics requires a careful control for both intrachain and interchain properties: For this purpose, simultaneous design of conjugated main chain as well as flexible side chain is essential.

With recent development of high-end scanning and copying technologies, counterfeiting has become a serious problem due to easy accessibility as well as its high quality.[10] In this trend, security inks for anti-counterfeiting or hidden information delivery have become a research field of great interest.[10–12,25–28] Security inks provide invisible information in the initial stage which is not possible to read or photocopy; the hidden information such as color, pattern or letters are programed to be revealed under certain circumstances. Various functional organic molecules have been developed for security inks.[25–28] In these molecular systems the hidden information was encoded based on fluorescence or color changes upon specific treatment (heat, chemical, or photoirradiation), and the concealed information was readable under irradiation of UV light. On the other hand, in case of CPs, polydiacetylenes that are prepared from unique molecular assembly of diacetylene monomers have mostly been investigated for security ink application, based on colorimetric change upon heat treatment.[10–12] However, CPs with aromatic conjugated main chains have not been fully investigated for security ink application despite its great potential based on the readily tunable optical properties through systematic molecular design.

In this work, we demonstrate the modification of the optical and electrochemical properties of diketopyrrolopyrrole (DPP)-based CPs by controlling both the interchain and intrachain properties with effective but simple polymer-design strategies. We synthesized three CPs having an alternating donor-acceptor structure (P1, P2 and P3 in **Figure 3.1**) using a phenyl linker connecting the electron-withdrawing DPP unit and an electron-donating building block. Regardless of three different electron-donating building blocks, all three CPs have almost identical absorption in diluted solutions and deep highest occupied molecular orbitals (HOMOs). This is caused by the large dihedral angle of the phenyl linker, which ensures a restricted effective conjugation length. In contrast, the interchain packing of the three CPs in the

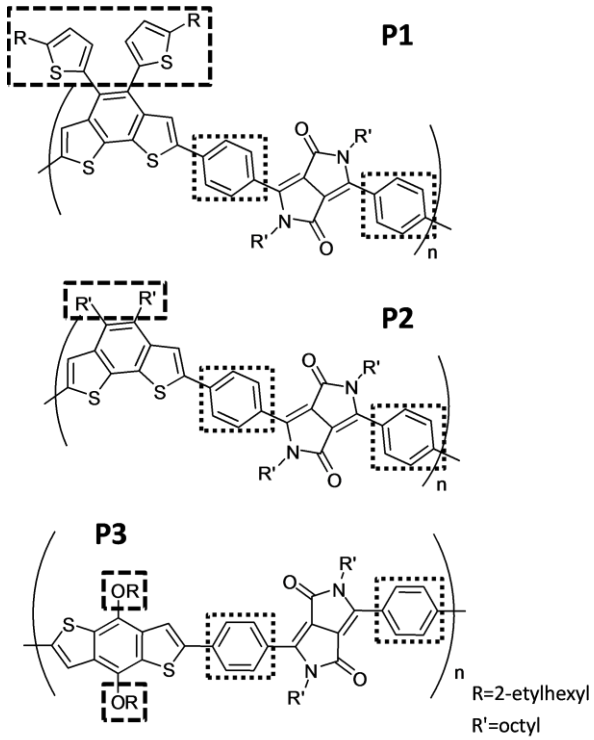

Figure 3.1 Chemical structures of the designed CPs: P1, P2 and P3. All three polymers have a phenyl linker between the electron-donating and electron-withdrawing building blocks to control the intrachain properties of CPs. Side chains with different bulkiness and direction are implemented to control the interchain interactions between CP chains.

aggregated-film state was gradually adjusted by changing the bulkiness and linking directions of the side chains (**Figure 3.1**) to control the optical absorbance and HOMO levels. The color gradation of CPs in the aggregated state, in contrast to their identical color in solution, enables us to demonstrate the encoding of covert information utilizing CP solutions as security inks on a silica substrate, which immediately develop hidden information by water dipping.

3.2. Results and Discussion

The three designed CPs in **Figure 3.1** have distinct side chains, which differ in bulkiness and linking direction. Each CP also has a phenyl linker between the electron-donor and electron-acceptor building blocks. In comparison to CPs having the commonly used planar thienyl linkers

for the DPP unit,[18,29] the phenyl linker induces a large dihedral angle between building blocks, and hence the twisted conformation is expected to reduce the effective conjugation length. As a result, we anticipate largely blue-shifted absorption and deeper HOMO levels due to the enlarged band gap of the phenyl-linked CPs. This is similar to the cases of poly(*p*-phenylene) or polyfluorene, which exhibit a large band gap with bluish emission even in the high-molecular-weight regime because of the non-planar conformation of the phenyl linkage.[30–32]

The optical properties of the three CPs are characterized by UV-vis spectrophotometry in diluted polymer solutions (10^{-5} M based on the repeating unit). Compared to the analogous CPs

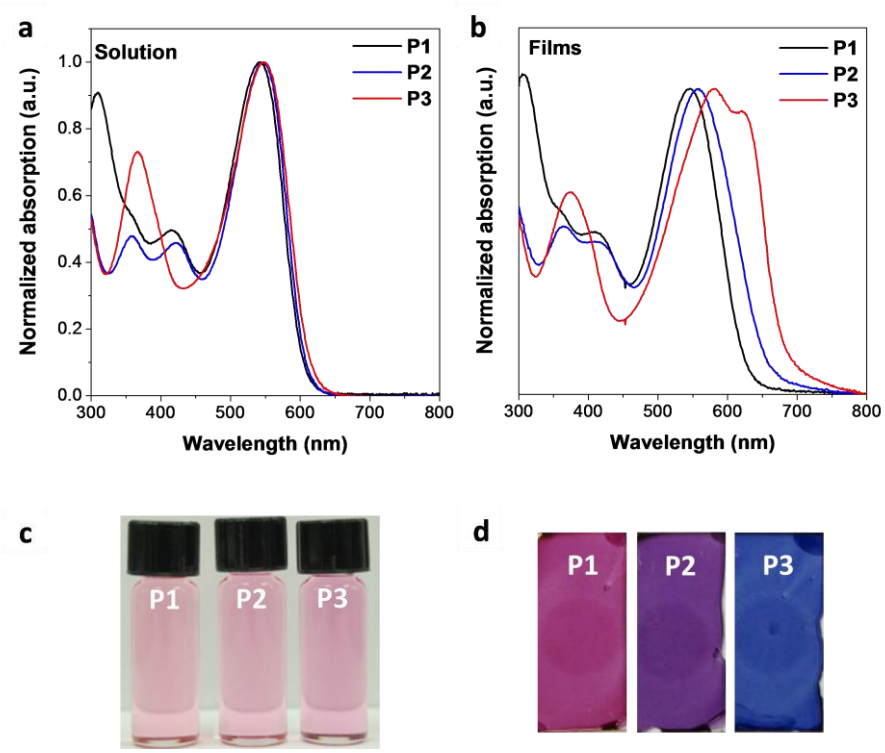

Figure 3.2 Optical properties of the synthesized CPs. (a) UV-vis absorption spectra of diluted CP solution samples in chloroform. The spectra for all three CPs are nearly identical, especially in λ_{max} and optical band edge, because the CPs have essentially the same intrachain properties. (b) UV-vis absorption spectra of CP films, thermally annealed at 130 ^{o}C. The choice of side chains controls the interchain packing and modifies the optical properties among CPs. (c) Optical images of the CP solutions under room light. (d) Optical images of the CP films under room light.

having the thienyl linker, whose optical band edge is around 800~950 nm,[18,29] the optical band edge of the diluted solution of all three CPs is shifted to ca. 600 nm (**Figure 3.2a**). This is a result of the modification of the intrachain properties by the phenyl linker incorporation. Interestingly, even though the three CPs are composed of different electron-donating building blocks (**Figure 3.1**), the color of each CP solution is almost identical (**Figure 3.2c**). This implies that the phenyl linker insertion effectively reduces the intramolecular charge transfer effect between the electron-donating and electron-withdrawing building blocks as well as the effective conjugation length. The identical intrachain properties, independent of the choice of electron-donating blocks, enables us to systematically investigate the effects of side chains on the interchain packing of CPs and, consequently, the alteration of their optoelectronic properties of P1, P2 and P3.

To further probe the role of the phenyl versus thienyl linkers on the structural and optical properties of the synthesized CPs, we performed structural-relaxation and electronic-structure calculations using Guassian09.[33] The molecules were relaxed using density functional theory (DFT) with the B3LYP hybrid functional and the 6-31G** basis set. We started by investigating the dihedral angle of the monomer unit (**Figure 3.3**). In the case of the thienyl linker, the dihedral angle between the electron-donating/

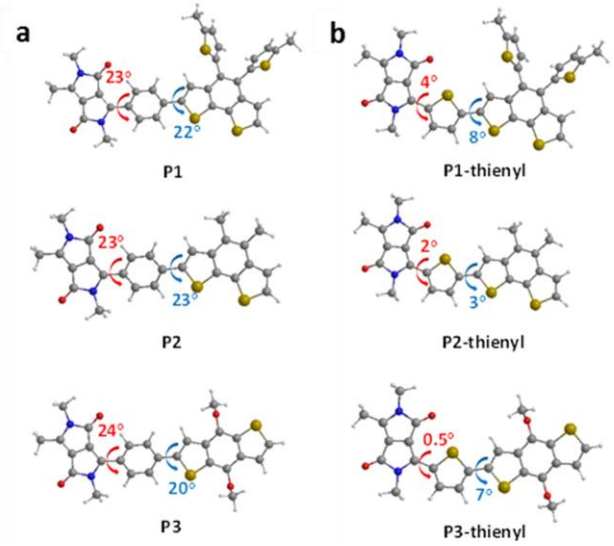

Figure 3.3 Calculated dihedral angles of the monomeric units of P1 (top), P2 (middle), P3 (bottom) with (a) a phenyl linker and (b) a thienyl linker.

withdrawing building blocks and the thienyl linker varies between 0.45° to 8.02°, which implies an almost planar chain conformation (**Figure 3.3b**). On the other hand, the phenyl linker shows a much larger dihedral angle, between 20.42° to 23.65°, which is expected by the CP design (**Figure 3.3a**). Using the optimized conformation of the monomeric units with phenyl or thienyl linker, we investigated the band gaps of the monomer, dimer, and trimer structures. It is revealed that the phenyl linked CPs do exhibit a larger band gap than the thienyl-linked CPs (**Table 3.1**). For the P1, P2 and P3 analogues, trimers bearing a phenyl linker have band gaps of 2.28, 2.27,

Table 3.1 Calculated HOMO, LUMO, and band gap energies of the monomer, dimer, and trimer units of the CPs

Monomers	HOMO (eV)	LUMO (eV)	Band Gap (eV)
P1	-5.1	-2.33	2.77
P1 – Thienyl	-4.97	-2.44	2.53
P2	-5.09	-2.32	2.77
P2 – Thienyl	-4.95	-2.43	2.52
P3	-5.11	-2.35	2.76
P3 – Thienyl	-4.99	-2.48	2.51

Dimers	HOMO (eV)	LUMO (eV)	Band Gap (eV)
P1	-4.99	-2.62	2.37
P1 – Thienyl	-4.79	-2.76	2.03
P2	-4.97	-2.61	2.36
P2 – Thienyl	-4.78	-2.76	2.02
P3	-5.00	-2.66	2.34
P3 – Thienyl	-4.81	-2.85	1.96

Trimers	HOMO (eV)	LUMO (eV)	Band Gap (eV)
P1	-4.96	-2.68	2.28
P1 – Thienyl	-4.75	-2.85	1.9
P2	-4.96	-2.69	2.27
P2 – Thienyl	-4.74	-2.8	1.94
P3	-4.96	-2.74	2.22
P3 – Thienyl	-4.81	-2.97	1.84

2.22 eV respectively, which is larger than those of thienyl-linked trimers (1.90, 1.94, 1.84 eV). Furthermore, the band gap decreases faster in thienyl-linker analogues as the chain length increases from the monomer to the trimer. This difference in band gaps supports the idea that the effective conjugation is more restricted in twisted phenyl linker analogues compared to planar thienyl linker analogues. In addition, the phenyl linker insertion shifts the calculated HOMO levels of the CPs deeper (**Table 3.1**). The deep HOMO level is highly plausible to be advantageous when CPs are utilized in energy device application in terms of open circuit voltage (V_{oc}).

Even though the three CPs show almost identical optical properties in dilute solutions, their solid-state optical properties differ significantly (**Figure 3.2, b and d**). The variation of the solid-state properties is originated from the molecular design, as each CPs has a different side chain with distinct bulkiness and orientation, which affects the interchain packing. P1 has two branched 2-ethylhexyl side chains connected through a bulky thienyl ring to the CP main chain. Our calculations show that the thienyl rings of the side chains are not in the same plane as the electron-donating benzo[2,1-b:3,4-b']dithiophene that they are connected to, but have instead adopted a largely twisted conformation (ca. 69^{o}) to minimize steric hindrance (P1 in **Figure 3.3a**). Because of the branched bulky 2-ethylhexyl chains together with the twisted thienyl rings, the main chains of P1 are anticipated to have minimal co-facial π-π stacking. On the other hand, P2 has two linear octyl side chains connected on the same side of the benzo[2,1-b:3,4-b']dithiophene unit but without the thienyl linkage, which is expected to have a mediocre propensity for interchain packing. The n-octyl side chains of P2 might stretch out to the opposite out-of-plane directions of the main chain plane due to steric hindrance as shown in **Figure 3.4**. In case of P3, the two 2-ethylhexyloxy side chains are not bulky enough to prevent P3 from

aggregating.[24] Moreover, they are attached on the opposite sides of the benzo[1,2-b:4,5-b']dithiophene donor unit such that the side chains do not have steric repulsion either. As a result, P3 is expected to have strong π-π stacking between the main chains.

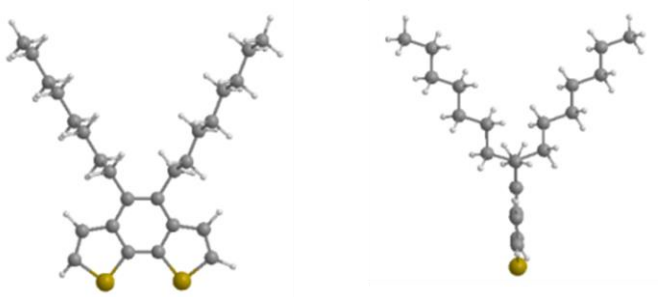

Figure 3.4 Computation on side chain conformation: electron donating building blocks of P2.

Indeed, the colors and the UV-vis absorption spectra of the thermally annealed CP films show distinct gradation despite the similar absorption spectra in solution (**Figure 3.2**). The absorption λ_{max} of the P3 film (583 nm) is red-shifted by 36 nm compared to that of the P3 solution (547 nm) and a new aggregation band appears at 620 nm (**Figure 3.2b**). The red-shifted new absorption band in P3 film may also be ascribed to an extended effective conjugation length caused by planarization of the conjugated main chain in the aggregated film state. In contrast, P1 essentially shows very similar absorption in the solid film (λ_{max}= 547 nm) and in solution (λ_{max}= 543 nm) due to weak interchain interactions, while the absorption λ_{max} of the P2 film is red-shifted by 9 nm compared to the P2 solution (**Figure 3.2, a** and **b**). The grazing incidence X-ray diffraction (GIXRD) analysis also revealed the same trend in the interpolymer packing:

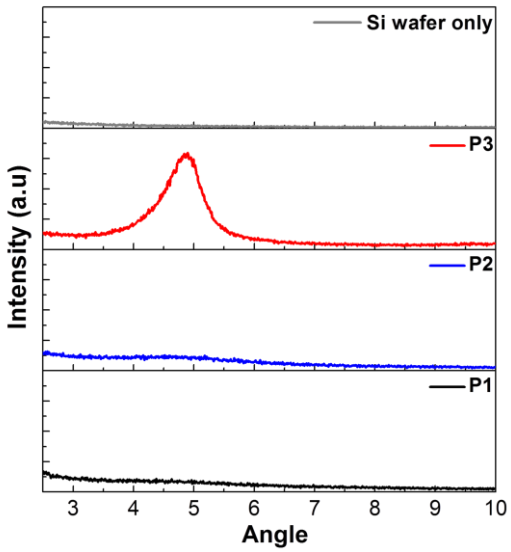

Figure 3.5 GIXRD of thermally annealed CP films and background Si wafer.

P3 shows a distinct peak at about 5^{o} corresponding to the developed interchain packing, while P1 shows amorphous packing due to the out-of-plane bulky side chains (**Figure 3.5**).

We further demonstrate the encoding of covert optical information on a silica substrate using the three CPs as security inks by exploiting the subtle difference among their interpolymer packing. A highly polar silica gel is likely to interact strongly with the CPs in the dry-state due to polar-polar interactions, which can prevent the aggregation of CPs. When dilute solutions of the CPs (ca. 5×10^{-4} M based on the repeating unit) were painted on polar silica gel substrates, the

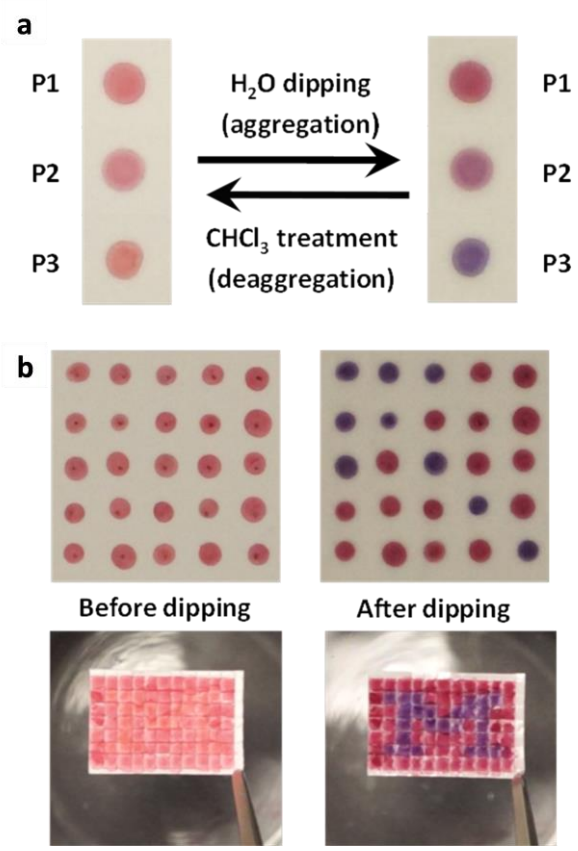

Figure 3.6 Encoding latent optical information on a silica substrate using the CPs as a security ink. (a) Reversible color change of CP on a silica substrate upon water and chloroform treatment. The color change is particularly prominent for P2 and P3. (b) The latent pattern appears upon water-induced aggregation. Before dipping in water, the colors of P1 and P3 on a silica substrate are undistinguishable (left panels). Only P3 clearly changes its color from red to bluish purple upon aggregation by water treatment, revealing the covert arrow pattern or the hidden letter "M" (right panels).

CPs retained identical solution-like colors even after evaporation of the chloroform solvent (**Figure 3.6a**). However, because water molecules are highly polar and favorable for hydrogen bonding, they interact strongly with the silica substrates and break the CP-substrate interaction. The different aggregation tendencies of the CPs caused by the side chains were manifested by a vivid color difference among the CP films when the substrate was dipped into water: P1 is red, P2 is purple, and P3 is bluish purple (**Figure 3.6a**). By using P1 and P3 as inks, we demonstrated the encoding of latent patterns and messages. An array of 5 × 5 dots of P1 and P3 inks with identical colors were patterned on a silica substrate (**Figure 3.6b**). When the dot array was immersed into water, the latent arrow image was developed immediately.[34] By increasing the array size to 11 × 7, we could demonstrate the covert letter "M" (**Figure 3.6b**).[34] Moreover, this phenomenon is completely reversible: the patterns developed by water are completely erased by chloroform dipping or under chloroform vapor treatment (**Figure 3.6a**).[34]

The design strategies to control the intrachain and interchain properties of CPs also essentially link to the electrochemical properties of the CP films. Each CP shares the same phenyl linker so as to has a deeper HOMO than the conventional analogous CPs with thienyl linkers. Cyclic voltammetry (CV) measurements were conducted to measure the energy levels of the three CPs. CP films for the measurements were spin cast onto ITO substrates, followed by thermal annealing. The energy levels of Regioregular poly(3-hexylthiophene) (P3HT) and [6,6]-Phenyl-C_{61}-butyric acid methyl ester (PCBM) are presented together with the CPs for comparison (**Figure 3.7b**). The three CPs indeed have deep HOMO energy levels (-5.34 ~ -5.69 eV) (**Figure 3.7**), which are deeper by about 0.3 eV than the HOMO levels of the analogous CPs with thienyl linkers reported in the literature.[18,35] Furthermore, the interpolymer packing propensity difference of the three CPs also affects the electrochemical properties of CP films.

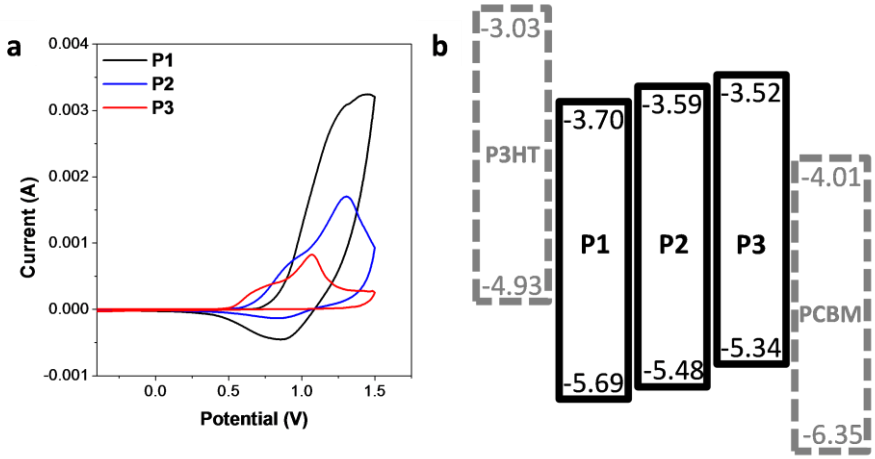

Figure 3.7 Electrochemical properties of P1, P2, and P3. (a) CV measurement of CPs. (b) The energy level diagram of the synthesized CPs, P3HT, and PCBM.

Similar to the variation of the optical properties, the different interchain properties of the CPs result in a gradual change of the HOMO levels: The restricted interchain interaction via the side chain design results in deeper HOMO levels. As a result, P1 with an amorphous nature has the deepest HOMO level (-5.69 eV), while P3 with a relatively high interpolymer packing propensity exhibits the shallowest HOMO level (-5.34 eV) among the three CPs. A similar trend of the HOMO levels were reported in recent publications, emphasizing the role of side chains in designing the electrochemical properties.[20,21,36]

3.3. Conclusion

In summary, we present an effective but simple design strategy for controlling the optical and electrochemical properties of CPs. Controlling the dihedral angle along the CP main chain with a phenyl linker combined with side chains of varying bulkiness and orientation can modulate both the intrachain and interchain properties of CPs. Regardless of the difference in electron-donating building blocks, the synthesized CPs, P1, P2 and P3, exhibit almost identical absorption with deep HOMO energy levels, due to a restricted effective conjugation length resulting from the

large dihedral angle of the phenyl linker. The side chain design decisively affects the interpolymer packing of the CPs and renders gradual shifts in optical properties and HOMO energy levels in the aggregated state. We further demonstrate the encoding of latent optical information on a silica substrate by exploiting the subtle interpolymer packing difference of the three CPs. Hidden patterns recorded in the dry state are immediately revealed upon water treatment in a completely reversible manner.

3.4. Experimental Section

3.4.1. Methods

3.4.1.1. Molecular Weight of CPs

The molecular weights of the CPs are measured by gel permeation chromatography (GPC, Waters 515 HPLC Pump) coupled with an RI detector (Waters 2410) and three columns (Waters Styragel) using chloroform as an eluent (flow rate 1 $ml \cdot min^{-1}$). The polystyrene standards were used for the calibration.

3.4.1.2. Computational Details

Hybrid density functional theory calculations were performed using Gaussian Revision C.01. All calculations were performed with the B3LYP functional and the 6-31G** basis set. The initial geometries of the monomer structures were constructed in Avogadro[37] and subsequently relaxed in Gaussian. The relaxed monomer structures were then chained together to generate the dimer and trimer structures, which were subsequently relaxed in Gaussian.

3.4.1.3. Grazing Incident X-ray Diffraction (GIXRD)

Grazing incidence small angle X-ray diffraction for thermally annealed P1, P2, and P3 thin films was carried out by a Rigaku Rotating Anode X-Ray Diffractometer (λ=1.54 Å). For minimal background signal at the used grazing angle (1^{o}), single-crystalline silicon substrates were used for the sample preparation.

3.4.1.4. Spectroscopic Characterization

The ^{1}H-NMR spectrum was obtained by a Varian, Inova 500 (500 MHz) with solution samples in $CDCl_3$. Chemical shift values were recorded as parts per million, relative to tetramethylsilane as an internal standard. Coupling constants were recorded in Hertz. UV-visible absorption spectra were characterized with a Varian Cary50 UV/Vis spectrophotometer. The optical band gaps of CPs were determined from the absorption band edge.

3.4.1.5. Cyclic Voltammetry (CV)

HOMO levels of CPs were measured by cyclic voltammetry using platinum wire counter electrode, with Ag/Ag^{+} as a reference electrode and 0.1 M tetrabutylammonium hexafluorophosphate solution in acetonitrile as electrolyte. The CP films for the measurement were spin-cast onto ITO (working electrode) substrates, followed by thermal annealing (130 ^{o}C). Ferrocene was utilized as a reference.

3.4.2. Materials and Synthesis

All chemicals and solvents for the synthesis were purchased from commercial suppliers (Sigma-Aldrich, TCI, Acros, and Fisher Sci.). The syntheses of monomers were performed following previously described synthetic routes.[23,38–40]

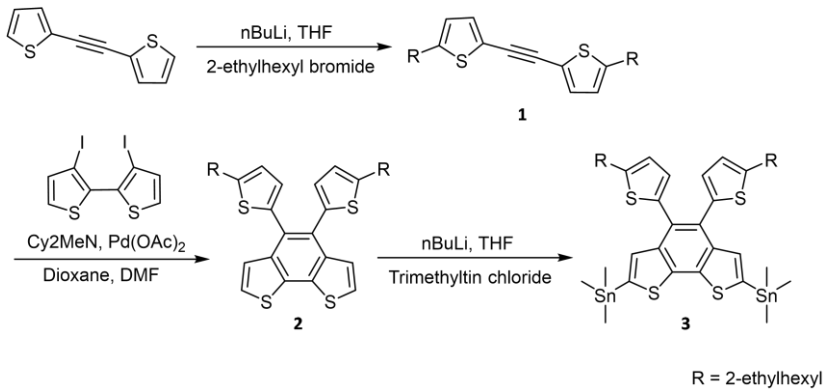

Figure 3.8 Synthetic route of the monomer for P1.

3.4.2.1. Synthesis of 1,2-bis(5-(2-ethylhexyl)thiophen-2-yl)ethyne [1]

Under Ar condition, 1,2-di(thiophen-2-yl)ethyne[41] (2.21 g, 11.62 mmol) was dissolved in anhydrous tetrahydrofuran. The solution was cooled down to -78 ^{o}C, and a 2.5 M solution of n-butyl lithium (10.22 ml, 25.55 mmol) was added dropwise. After stirring for 1hr, 2-ethylhexyl bromide (4.54 ml, 25.55 mmol) was added, and the reaction mixture was stirred at room temperature overnight. The mixture was poured into water and extracted with hexane. The organic phase was dried over $MgSO_4$ and the solvent was removed in *vacuo*. Column chromatography was conducted with hexane as an eluent. A light yellow liquid was obtained as a product (15%). ^{1}H NMR (500 MHz, $CDCl_3$, δ): 7.06 (d, *J* = 3.5 Hz, 2H), 6.64 (d, *J* = 3.5 Hz, 2H), 2.72 (d, *J* = 7.0 Hz, 4H), 1.60 – 1.52 (m, 2H), 1.38 – 1.24 (m, 16H), 0.94 – 0.84 (m, 12H); MS m/z (EI, relative intensity): 414.1 (M^+, 83.3), 315.0 (100), 302.0 (19.6), 215.9 (35.8), 202.9 (48.6).

3.4.2.2. Synthesis of 4,5-bis(5-(2-ethylhexyl)thiophen-2-yl)benzo[2,1-b:3,4-b']dithiophene [2]

Under Ar condition, compound **1** (0.78 g, 1.88 mmol), palladium(II) acetate (0.021 g, 0.094 mmol), N,N-dicyclohexylmethylamine (0.63 ml, 2.82 mmol), and 3,3'-diiodo-2,2'-bithiophene[39]

(0.393 g, 0.94 mmol) were added into anhydrous dioxane and N,N-dimethylformamide mixed solvent (1:1). The reaction mixture was heated up to 130 ^{o}C and stirred for 2 hours. After cooling down to room temperature, diethyl ether was added. The mixture was poured into water and extracted with diethyl ether. The organic phase was dried over $MgSO_4$ and the solvent was removed in *vacuo*. Column chromatography was conducted with hexane as an eluent. A colorless liquid was obtained as a product (61%). ^{1}H NMR (500 MHz, $CDCl_3$, δ): 7.43 (d, *J* = 5.5 Hz, 2H), 7.36 (d, *J* = 5.5 Hz, 2H), 6.78 (d, *J* = 3.5 Hz, 2H), 6.64 (d, *J* = 3.5 Hz, 2H), 2.70 (d, *J* = 7.0 Hz, 4H), 1.58 – 1.50 (m, 2H), 1.38 – 1.24 (m, 16H), 0.94 – 0.84 (m, 12H); MS m/z (EI, relative intensity): 578.2 (M^+, 100), 479.1 (35.0), 381.0 (23.6), 347.0 (26.9), 333.0 (19.39), 57.0 (32.3). HRMS (EI) calcd. for $C_{34}H_{42}S_4$ (M^+) 578.2169, found 578.2172.

3.4.2.3. Synthesis of (4,5-bis(5-(2-ethylhexyl)thiophen-2-yl)benzo[2,1-b:3,4-b']dithiophene-2,7-diyl)bis(trimethylstannane) [3]

Under Ar condition, compound **2** (0.19 g, 0.328 mmol) was dissolved in anhydrous tetrahydrofuran. A 2.5 M solution of n-butyl lithium (0.328 ml, 0.820 mmol) was added dropwise at 0 ^{o}C, and stirred for 30 min at room temperature. A 1 M solution of trimethyltin chloride (0.984 ml, 0.984 mmol) was added into the reaction mixture and was stirred overnight. The mixture was poured into water, extracted with diethyl ether, and washed multiple times with water. The washed organic phase was dried over $MgSO_4$ followed by solvent removal under high vacuum. The product was used without further purification as previously described.[38,39] A pale greenish yellow viscous liquid was obtained as a product. ^{1}H NMR (500 MHz, CDCl3): δ 7.44 (s, 2H), 6.76 (d, *J* = 3.5 Hz, 2H), 6.64 (d, *J* = 3.5 Hz, 2H), 2.72 (d, *J* = 7.0 Hz, 4H), 1.60 – 1.50 (m, 2H), 1.36 – 1.19 (m, 16H), 0.91 – 0.83 (m, 12H), 0.41 (s, 18H).

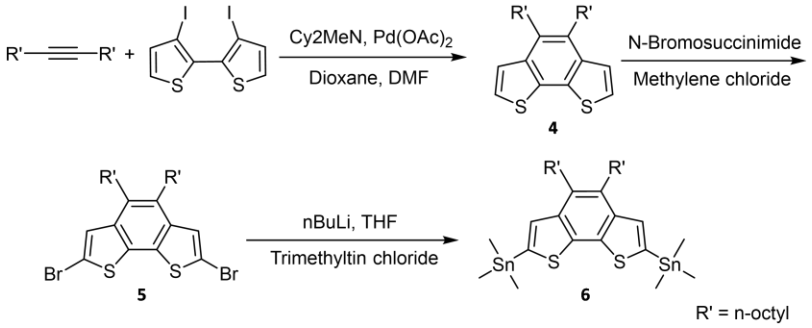

Figure 3.9 Synthetic route of the monomer for P2.

3.4.2.4. Synthesis of 4,5-dioctylbenzo[2,1-b:3,4-b']dithiophene [4]

The same procedure as with compound **2** was performed. Octadec-9-yne[42] was used (61%) to replace compound **1**. ^{1}H NMR (500 MHz, CDCl3): 7.46 (d, *J* = 5.0 Hz, 2H), 7.37 (d, *J* = 5.5 Hz, 2H), 3.03 – 2.99 (m, 4H), 1.68 – 1.61 (m, 4H), 1.51 – 1.44 (m, 4H), 1.40 –1.24 (m, 16 H), 0.91 – 0.86 (m, 6H).

3.4.2.5. Synthesis of 2,7-dibromo-4,5-dioctylbenzo[2,1-b:3,4-b']dithiophene [5]

Compound **4** (0.3 g, 0.72 mmol) was dissolved in methylene chloride, and N-bromosuccinimide (0.309 g, 1.73 mmol) was added at 0 ^{o}C. The reaction mixture was stirred overnight at room temperature. The mixture was poured into water and extracted. The organic phase was dried over $MgSO_4$ followed by solvent removal in *vacuo*. Column chromatography was conducted with hexane as an eluent. A white powder was obtained as a product (61%). ^{1}H NMR (500 MHz, CDCl3): δ 7.40 (s, 2H), 2.91 – 2.86 (m, 4H), 1.63 – 1.54 (m, 4H), 1.49 – 1.42 (m, 4H), 1.40 –1.24 (m, 16 H), 0.92 – 0.86 (m, 6H). MS m/z (EI, relative intensity): 572.0 (M^+, 100), 394.0 (14.2), 374.8 (65.8), 296.9 (8.7), 69.1(10.8).

3.4.2.6. Synthesis of (4,5-dioctylbenzo[2,1-b:3,4-b']dithiophene-2,7-diyl)bis(trimethylstannane) [6]

Under Ar condition, compound **5** (0.25 g, 0.436 mmol) was dissolved in anhydrous tetrahydrofuran. A 2.5 M solution of n-butyl lithium (0.4 ml, 1 mmol) was added dropwise at -78 ^{o}C, and stirred for 30 min. A 1 M solution of trimethyltin chloride (1 ml, 1 mmol) was added into the reaction mixture. After warming up to room temperature, the reaction mixture was stirred overnight. The mixture was poured into water, extracted with diethyl ether, and washed multiple times with water. The washed organic phase was dried over $MgSO_4$ followed by solvent removal under high vacuum. The product was used without further purification as previously described.[38,39] A pale greenish yellow viscous liquid was obtained as a product (84%). ^{1}H NMR (500 MHz, CDCl3): δ 7.48 (s, 2H), 3.08 – 2.98 (m, 4H), 1.70 – 1.62 (m, 4H), 1.52 – 1.45 (m, 4H), 1.43 – 1.23 (m, 16H), 0.94 – 0.85 (m, 6H), 0.44 (s, 18H).

3.4.2.7. General Procedure of Stille Type Polymerization for P1, P2, and P3

Under inert conditions, the prepared monomers (1:1 in equivalent) were dissolved into an anhydrous toluene and N,N-dimethylformamide mixed solvent (5:1 in volume). After adding 5 mol% of tetrakis(triphenylphosphine)palladium (0), the reaction mixture was heated up to 120 ^{o}C and stirred for 12 hours. Then, end-capping was conducted by adding 2-tributylstannyl thiophene and stirring for 6 hours, followed by adding 2-bromothiophene and stirring for another 6 hours. The final conjugated polymers were collected via reprecipitation of the reaction mixture into methanol. The precipitated polymers were collected through a 0.45 μm nylon filter. After washing the collected polymers with hexane, methanol, and acetone in a soxhlet apparatus to remove the oligomers and catalyst residue, the part soluble to chloroform was obtained. The

molecular weights of the synthesized polymers were measured by means of gel permeation chromatography (GPC): **P1** (M_n: 16047, M_w: 29214, PDI:1.82), **P2** (M_n: 17849, M_w: 34030, PDI:1.91), and **P3** (M_n: 8603, M_w: 15023, PDI:1.74).

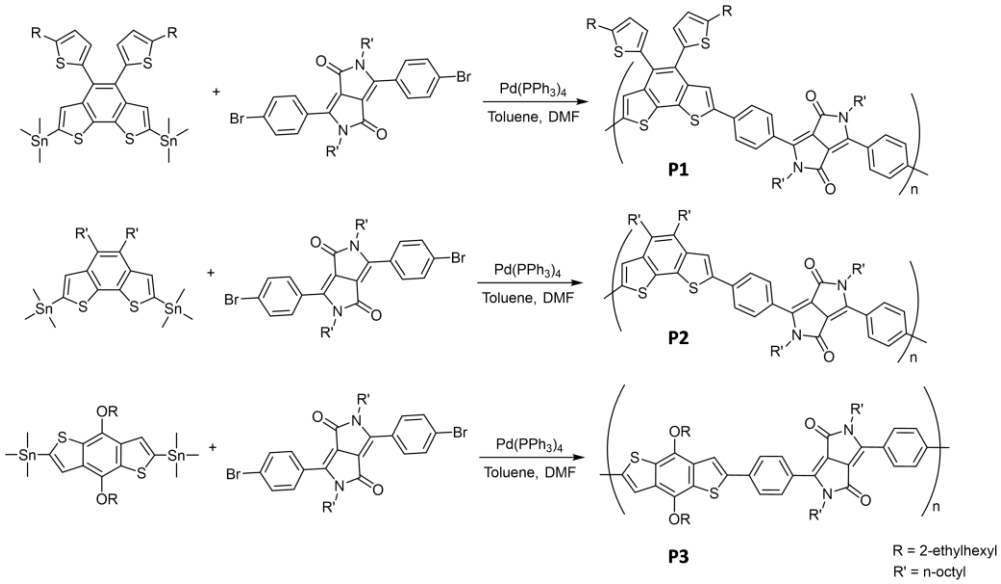

Figure 3.10 Synthetic scheme for polymerization.

3.5. Author Contribution

K. Chung, A. McAllister, D. Bilby, B.-G. Kim, M. S. Kwon, E. Kioupakis, J. Kim, Designing interchain and intrachain properties of conjugated polymers for latent optical information encoding. *Chem. Sci.* **6**, 6980–6985 (2015) - Published by The Royal Society of Chemistry.

Kyeongwoon Chung and Jinsang Kim designed the project, and Jinsang Kim directed the project. Kyeongwoon Chung and Bong-Gi Kim synthesized the series of CPs. Optical and electrochemical analyses on the CPs were conducted by Kyeongwoon Chung and partly by Min Sang Kwon and David Bilby. Kyeongwoon Chung performed latent optical information encoding demonstration. Computational work was conducted by Andrew McAllister and

Emmanouil Kioupakis. Kyeongwoon Chung and Jinsang Kim wrote the manuscript for publication, and all other authors had input.

3.6. References and Notes

1. J. Kim, D. T. McQuade, S. K. McHugh, T. M. Swager, Ion-Specific Aggregation in Conjugated Polymers: Highly Sensitive and Selective Fluorescent Ion Chemosensors. *Angew. Chemie* **112,** 4026–4030 (2000).
2. J. Lee, H. Jun, J. Kim, Polydiacetylene-Liposome Microarrays for Selective and Sensitive Mercury(II) Detection. *Adv. Mater.* **21,** 3674–3677 (2009).
3. H.-A. Ho, M. Boissinot, M. G. Bergeron, G. Corbeil, K. Doré, D. Boudreau, M. Leclerc, Colorimetric and Fluorometric Detection of Nucleic Acids Using Cationic Polythiophene Derivatives. *Angew. Chemie Int. Ed.* **41,** 1548–1551 (2002).
4. K. Lee, J.-M. Rouillard, B.-G. Kim, E. Gulari, J. Kim, Conjugated Polymers Combined with a Molecular Beacon for Label-Free and Self-Signal-Amplifying DNA Microarrays. *Adv. Funct. Mater.* **19,** 3317–3325 (2009).
5. K. Lee, L. K. Povlich, J. Kim, Recent advances in fluorescent and colorimetric conjugated polymer-based biosensors. *Analyst* **135,** 2179–2189 (2010).
6. G. Jang, J. Kim, D. Kim, T. S. Synthesis of triphenylamine-containing conjugated polyelectrolyte and fabrication of fluorescence color-changeable, paper-based sensor strips for biothiol detection. *Polym. Chem.* **6,** 714–720 (2015).
7. S. J. Toal, W. C. Trogler, Polymer sensors for nitroaromatic explosives detection. *J. Mater. Chem.* **16,** 2871 (2006).
8. L. O. Péres, J. Gruber, The use of block copolymers containing PPV in gas sensors for electronic noses. *Mater. Sci. Eng. C* **27,** 67–69 (2007).
9. J. Lee, S. Seo, J. Kim, Colorimetric Detection of Warfare Gases by Polydiacetylenes Toward Equipment-Free Detection. *Adv. Funct. Mater.* **22,** 1632–1638 (2012).
10. B. Yoon, J. Lee, I. S. Park, S. Jeon, J. Lee, J.-M. Kim, Recent functional material based approaches to prevent and detect counterfeiting. *J. Mater. Chem. C* **1,** 2388 (2013).
11. B. Yoon, H. Shin, O. Yarimaga, D.-Y. Ham, J. Kim, I. S. Park, J.-M. Kim, An inkjet-printable microemulsion system for colorimetric polydiacetylene supramolecules on paper substrates. *J. Mater. Chem.* **22,** 8680 (2012).
12. B. Yoon, D.-Y. Ham, O. Yarimaga, H. An, C. W. Lee, J.-M. Kim, Inkjet printing of conjugated polymer precursors on paper substrates for colorimetric sensing and flexible electrothermochromic display. *Adv. Mater.* **23,** 5492–5497 (2011).
13. J. S. Ha, K. H. Kim, D. H. Choi, 2,5-Bis(2-octyldodecyl)pyrrolo[3,4-c]pyrrole-1,4-(2H,5H)-dione-based donor-acceptor alternating copolymer bearing 5,5’-di(thiophen-2-yl)-2,2'-biselenophene exhibiting 1.5 cm2·V(-1)·s(-1) hole mobility in thin-film transistors. *J. Am. Chem. Soc.* **133,** 10364–10367 (2011).
14. A. J. Kronemeijer, E. Gili, M. Shahid, J. Rivnay, A. Salleo, M. Heeney, H. Sirringhaus, A selenophene-based low-bandgap donor-acceptor polymer leading to fast ambipolar logic. *Adv. Mater.* **24,** 1558–1565 (2012).

15. C. M. Amb, S. Chen, K. R. Graham, J. Subbiah, C. E. Small, F. So, J. R. Reynolds, Dithienogermole as a fused electron donor in bulk heterojunction solar cells. *J. Am. Chem. Soc.* **133,** 10062–10065 (2011).
16. L. Huo, S. Zhang, X. Guo, F. Xu, Y. Li, J. Hou, Replacing alkoxy groups with alkylthienyl groups: a feasible approach to improve the properties of photovoltaic polymers. *Angew. Chem. Int. Ed. Engl.* **50,** 9697–9702 (2011).
17. J. You, L. Dou, K. Yoshimura, T. Kato, K. Ohya, T. Moriarty, K. Emery, C.-C. Chen, J. Gao, G. Li, Y. Yang, A polymer tandem solar cell with 10.6% power conversion efficiency. *Nat. Commun.* **4,** 1446 (2013).
18. L. Huo, J. Hou, H.-Y. Chen, S. Zhang, Y. Jiang, T. L. Chen, Y. Yang, Bandgap and Molecular Level Control of the Low-Bandgap Polymers Based on 3,6-Dithiophen-2-yl-2,5-dihydropyrrolo[3,4- c]pyrrole-1,4-dione toward Highly Efficient Polymer Solar Cells. *Macromolecules* **42,** 6564–6571 (2009).
19. M. Yuan, A. H. Rice, C. K. Luscombe, Benzo[2,1-b;3,4-b′]dithiophene-based low-bandgap polymers for photovoltaic applications. *J. Polym. Sci. Part A Polym. Chem.* **49,** 701–711 (2011).
20. J. Mei, Z. Bao, Side Chain Engineering in Solution-Processable Conjugated Polymers. *Chem. Mater.* **26,** 604–615 (2014).
21. L. Yang, H. Zhou, W. You, Quantitatively Analyzing the Influence of Side Chains on Photovoltaic Properties of Polymer−Fullerene Solar Cells. *J. Phys. Chem. C* **114,** 16793–16800 (2010).
22. J. M. Szarko, J. Guo, Y. Liang, B. Lee, B. S. Rolczynski, J. Strzalka, T. Xu, S. Loser, T. J. Marks, L. Yu, L. X. Chen, When function follows form: Effects of donor copolymer side chains on film morphology and BHJ solar cell performance. *Adv. Mater.* **22,** 5468–5472 (2010).
23. K. Chung, M. S. Kwon, B. M. Leung, A. G. Wong-Foy, M. S. Kim, J. Kim, S. Takayama, J. Gierschner, A. J. Matzger, J. Kim, Shear-Triggered Crystallization and Light Emission of a Thermally Stable Organic Supercooled Liquid. *ACS Cent. Sci.* **1,** 94–102 (2015).
24. B.-G. Kim, E. J. Jeong, J. W. Chung, S. Seo, B. Koo, J. Kim, A molecular design principle of lyotropic liquid-crystalline conjugated polymers with directed alignment capability for plastic electronics. *Nat. Mater.* **12,** 659–664 (2013).
25. D. R. Whang, Y. You, W.-S. Chae, J. Heo, S. Kim, S. Y. Park, Solid-state phosphorescence-to-fluorescence switching in a cyclometalated Ir(III) complex containing an acid-labile chromophoric ancillary ligand: implication for multimodal security printing. *Langmuir* **28,** 15433–15437 (2012).
26. X. Zhu, R. Liu, Y. Li, H. Huang, Q. Wang, D. Wang, X. Zhu, S. Liu, H. Zhu, An AIE-active boron-difluoride complex: multi-stimuli-responsive fluorescence and application in data security protection. *Chem. Commun.* **50,** 12951–12954 (2014).
27. A. Kishimura, T. Yamashita, K. Yamaguchi, T. Aida, Rewritable phosphorescent paper by the control of competing kinetic and thermodynamic self-assembling events. *Nat. Mater.* **4,** 546–549 (2005).
28. S. Kobatake, H. Imagawa, H. Nakatani, S. Nakashima, The irreversible thermo-bleaching function of a photochromic diarylethene having trimethylsilyl groups. *New J. Chem.* **33,** 1362 (2009).
29. L. Dou, J. You, J. Yang, C.-C. Chen, Y. He, S. Murase, T. Moriarty, K. Emery, G. Li, Y.

Yang, Tandem polymer solar cells featuring a spectrally matched low-bandgap polymer. *Nat. Photonics* **6,** 180–185 (2012).
30. M. Remmers, B. Müller, K. Martin, H.-J. Räder, W. Köhler, Poly(p -phenylene)s. Synthesis, Optical Properties, and Quantitative Analysis with HPLC and MALDI−TOF Mass Spectrometry. *Macromolecules* **32,** 1073–1079 (1999).
31. D. Neher, Polyfluorene Homopolymers: Conjugated Liquid-Crystalline Polymers for Bright Blue Emission and Polarized Electroluminescence. *Macromol. Rapid Commun.* **22,** 1365–1385 (2001).
32. V. Cimrová, M. Remmers, D. Neher, G. Wegner, Polarized light emission from LEDs prepared by the Langmuir-Blodgett technique. *Adv. Mater.* **8,** 146–149 (1996).
33. Gaussian 09, Revision C.01, M. J. Frisch, G. W. Trucks, H. B. Schlegel, G. E. Scuseria, M. A. Robb, J. R. Cheeseman, G. Scalmani, V. Barone, B. Mennucci, G. A. Petersson, H. Nakatsuji, M. Caricato, X. Li, H. P. Hratchian, A. F. Izmaylov, J. Bloino, G. Zheng, J. L. Sonnenberg, M. Hada, M. Ehara, K. Toyota, R. Fukuda, J. Hasegawa, M. Ishida, T. Nakajima, Y. Honda, O. Kitao, H. Nakai, T. Vreven, J. A. Montgomery, Jr., J. E. Peralta, F. Ogliaro, M. Bearpark, J. J. Heyd, E. Brothers, K. N. Kudin, V. N. Staroverov, R. Kobayashi, J. Normand, K. Raghavachari, A. Rendell, J. C. Burant, S. S. Iyengar, J. Tomasi, M. Cossi, N. Rega, J. M. Millam, M. Klene, J. E. Knox, J. B. Cross, V. Bakken, C. Adamo, J. Jaramillo, R. Gomperts, R. E. Stratmann, O. Yazyev, A. J. Austin, R. Cammi, C. Pomelli, J. W. Ochterski, R. L. Martin, K. Morokuma, V. G. Zakrzewski, G. A. Voth, P. Salvador, J. J. Dannenberg, S. Dapprich, A. D. Daniels, Ö. Farkas, J. B. Foresman, J. V. Ortiz, J. Cioslowski, and D. J. Fox, Gaussian, Inc., Wallingford CT, 2009.
34. See the supporting movies; K. Chung, A. McAllister, D. Bilby, B.-G. Kim, M. S. Kwon, E. Kioupakis, J. Kim, Designing interchain and intrachain properties of conjugated polymers for latent optical information encoding. *Chem. Sci.* **6,** 6980–6985 (2015).
35. C. Kanimozhi, P. Balraju, G. D. Sharma, S. Patil, Synthesis of diketopyrrolopyrrole containing copolymers: a study of their optical and photovoltaic properties. *J. Phys. Chem. B* **114,** 3095–3103 (2010).
36. C. Piliego, T. W. Holcombe, J. D. Douglas, C. H. Woo, P. M. Beaujuge, J. M. J. Fréchet, Synthetic control of structural order in N-alkylthieno[3,4-c]pyrrole-4,6-dione-based polymers for efficient solar cells. *J. Am. Chem. Soc.* **132,** 7595–7597 (2010).
37. M. D. Hanwell, D. E. Curtis, D. C. Lonie, T. Vandermeersch, E. Zurek, G. R. Hutchison, Avogadro: an advanced semantic chemical editor, visualization, and analysis platform. *J. Cheminform.* **4,** 17 (2012).
38. S. Xiao, A. C. Stuart, S. Liu, W. You, Conjugated polymers based on benzo[2,1-b:3,4-b']dithiophene with low-lying highest occupied molecular orbital energy levels for organic photovoltaics. *ACS Appl. Mater. Interfaces* **1,** 1613–1621 (2009).
39. T. Harschneck, N. Zhou, E. F. Manley, S. J. Lou, X. Yu, M. R. Butler, A. Timalsina, R. Turrisi, M. A. Ratner, L. X. Chen, R. P. H. Chang, A. Facchetti, T. J. Marks, Substantial photovoltaic response and morphology tuning in benzo[1,2-b:6,5-b']dithiophene (bBDT) molecular donors. *Chem. Commun.* **50,** 4099–4101 (2014).
40. Y. Liang, D. Feng, Y. Wu, S.-T. Tsai, G. Li, C. Ray, L. Yu, Highly efficient solar cell polymers developed via fine-tuning of structural and electronic properties. *J. Am. Chem. Soc.* **131,** 7792–7799 (2009).
41. M. J. Mio, L. C. Kopel, J. B. Braun, T. L. Gadzikwa, K. L. Hull, R. G. Brisbois, C. J.

Markworth, P. A. Grieco, One-Pot Synthesis of Symmetrical and Unsymmetrical Bisarylethynes by a Modification of the Sonogashira Coupling Reaction. *Org. Lett.* **4,** 3199–3202 (2002).

42. J.-S. Wu, C.-T. Lin, C.-L. Wang, Y.-J. Cheng, C.-S. Hsu, New Angular-Shaped and Isomerically Pure Anthradithiophene with Lateral Aliphatic Side Chains for Conjugated Polymers: Synthesis, Characterization, and Implications for Solution-Prossessed Organic Field-Effect Transistors and Photovoltaics. *Chem. Mater.* **24,** 2391–2399 (2012).

CHAPTER 4

Molecular design principles for directed alignment of conjugated polymers

4.1. Introduction

Directed macroscopic alignment of conjugated polymers (CPs) is crucial yet challenging to maximize the potential optoelectronic properties of CPs in various device applications. In this chapter, molecular design factors for directed self-assembly and alignment of CPs are systematically investigated, which can decidedly impact on the optoelectronic applications of CPs.

Conjugated polymers (CPs) are materials of interest for various optical and electronic applications, including optical sensors,[1–5] security inks,[6–9] and electronic devices.[10–12] Generally, CPs have a rigid conjugated backbone and flexible solubilizing side chains. Because of their long rigid rod-like structure and one-dimensional (1-D) p-orbital overlap, CPs exhibit one dimensional anisotropy in their characteristics such as absorption, emission, and charge mobility. Therefore, alignment of CPs is essential to maximize their interesting 1-D properties in applications. To quantify degree of CP alignment, the dichroic ratio, a ratio of absorption or emission intensity between the values from parallel and perpendicular to the alignment direction (dichroic ratio = $I_{//}/I_{\perp}$), has been conventionally employed. In case of isotropic (not aligned) CP film, the dichroic ratio is around 1, which means no directional deviation of absorption and/or

emission intensity. However, the dichroic ratio increases if effective alignment of CPs develops in the CP film.

To fully utilize CPs' potential optoelectronic properties, various CP processing methods for alignment have been researched[13] including Langmuir-Blodgett (LB) technique,[14,15] mechanical rubbing,[16–18] nanoimprinting,[19–21] directional solidification,[22–25] electrospinning,[26–28] and pre-patterned substrate[29–32] or matrix[33–39] induced CP alignment (see **Chapter 1.3.2.**). Nevertheless the cutting-edge processing methods have enabled decent CP alignments for specific types of CPs, the molecular feature to accomplish CP alignment had not been understood. Recently, our group investigated molecular design for directed alignment of CPs, and realized anisotropic optoelectronic properties from aligned CP films.[40] The CP1 (**Figure 4.1a**) chains are readily aligned to the direction of flow field and exhibited a high dichroic ratio of ca. 16 by satisfying three design requirements to be a lyotropic liquid crystalline polymer; (1) concentration-induced planarization unit (S-F interaction), and (2) bulky side chains linked to (3) a tetrahedral carbon.[40] The hole mobility of the aligned CP1 film is increased by more than two orders of magnitude compared to that of a randomly oriented CP1 film.[40]

The most important qualification for a molecular design principle is an universal applicability, since it is a foundation for future design and application. Even though CP1 showed efficient alignment by satisfying three design rules, the universal applicability of the established design rules were not studied in the previous report.[40] Therefore, in this chapter, the applicability of the design parameters for directed CP alignment are systematically examined by means of various polymer building blocks. For this purpose, three new polymers, NCP1, NCP2 and NCP3, are designed and synthesized (**Figure 4.1a**). NCP1 satisfies all three design rules and clearly shows directed alignment under shear flow while NCP2 and NCP3 do not exhibit alignment of CP

chains due to the lack of one design requirement each. Furthermore, a systematic investigation is conducted to additionally identify other design factors that can also largely affect the alignment properties of CPs. For this purpose, a series of CPs are designed, synthesized, and characterized; (1) CP with different type of bulky side chains (NCP4, **Figure 4.3a**), (2) CPs without concentration-induced planarization unit (NCP5 and NCP6, **Figure 4.4a**), and (3) CP with different concentration-induced planarization unit (NCP7, **Figure 4.5a**).

4.2. Results and Discussion

Generally, CPs have a strong propensity to aggregate due to π-π interaction between conjugated backbones. However, to realize directed alignment, CP chains should self-assemble but also be mobile to be aligned under an applied external force field. The three design requisites, (1) concentration-induced planarization unit, and (2) bulky side chains linked to (3) a tetrahedral carbon endow the CPs in a concentrated solution with certain interchain interactions as well as mobility, properties characteristic of a lyotropic liquid crystal (LC), so that the CPs can be effectively aligned under an applied shear flow. In the diluted solution, the twisted phenyl rings in CP backbone together with bulky side chains prevent massive aggregation of CP chains. As solvent evaporates under the alignment condition (at 140 ^{o}C), the intramolecular S-F interaction induces the conjugated backbone to be planarized,[41] which promotes interpolymer π-π interactions. Still, the large side chains on the out-of-plain tetrahedral carbon linker prevent too strong aggregation, and as a consequence mobile CP chains are then aligned to the direction of applied field. Indeed, CP1 (**Figure 4.1a**) showed a birefringent texture and lyotropic LC characteristics, only at a high concentration.[40]

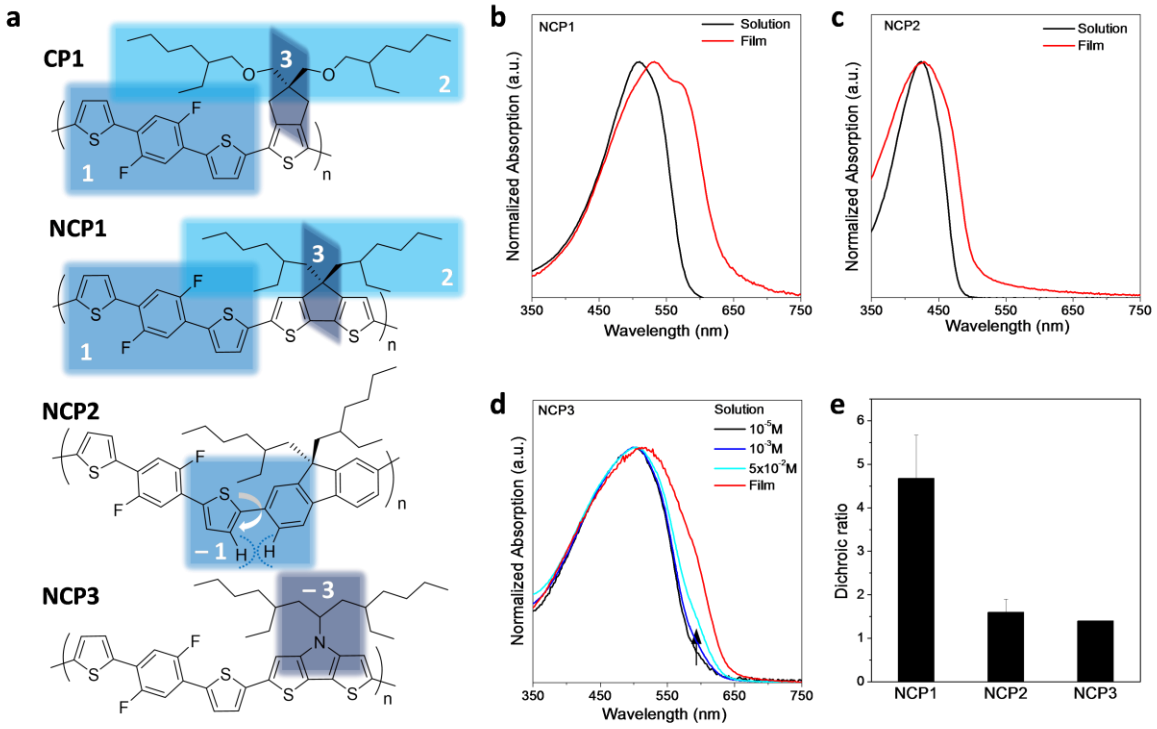

Figure 4.1 Chemical structures, optical and alignment properties of CPs designed based on design principles for directed alignment: (1) concentration-induced planarization unit, and (2) bulky side chains linked to (3) a tetrahedral carbon. (a) Chemical structures of CP1, NCP1, NCP2 and NCP3. (b-d) UV-vis absorption spectra of (b) NCP1, (c) NCP2 and (d) NCP3. (e) Dichroic ratio of aligned CP films.

It is worth to note that CPs which are capable of directed alignment have a distinct UV-vis absorption trait; no aggregation band in solution even in a highly concentrated regime (~100 $mg \cdot ml^{-1}$) but largely red-shifted λ_{max} in the solid state due to the concentration-induced planarization. Therefore, simple UV-vis absorption analysis in the solution and the solid state can single certain CPs out for more systematic LC analysis and alignment test.

To systematically investigate molecular design principles for directed alignment of CPs, seven new polymers (NCP1~7) are designed and synthesized through the Stille palladium coupling polymerization. Polymer purification and contact coating for directed CP alignment were conducted according to the previous procedures.[40] Firstly, NCP1, NCP2 and NCP3 were

prepared to confirm the suggested preliminary design principles (**Figure 4.1a**). From the CP design, the cyclopenta[*c*]thiophene building block of CP1 is substituted to the cyclopenta[2,1-*b*:3,4-*b'*]dithiophene building block in NCP1. Still, NCP1 satisfies all three design factors by including concentration-induced planarization unit via S-F interaction as well as bulky 2-ethylhexyl side chains on a tetrahedral carbon in the CP analogue. On the other hand, NCP2 cannot satisfy the concentration induced chain planarization requirement because the large thienyl-phenyl dihedral angle as depicted in **Figure 4.1a**. NCP3 have a nitrogen atom replacing the tetrahedral carbon of NCP1 as a linker to connect the side chains. As a result, NCP3 fails to satisfy the third design parameter, the out-of-plane side chain linker requirement.

The solution and film absorption spectra of NCP1, NCP2 and NCP3 clearly indicate whether the polymer would have the capability of CP alignment that was set from the CP design. NCP1 shows no aggregation band in solution due to the twisted phenyl group and bulky side chains that effectively prevent interaction between polymer chains (**Figure 4.1b**), the same absorption trait of the CP1 solution.[40] On the other hand, in the solid state NCP1 shows red-shifted λ_{max} (~22 nm) and an additional aggregation shoulder band due to concentration-induced chain planarization and developed interchain packing (**Figure 4.1b**). Different from NCP1, NCP2 exhibits no significant red-shifted absorption λ_{max} in film compared to diluted solution due to the restricted chain planarization of the twisted fluorene building block (**Figure 4.1, a** and **c**). On the other hand, the diluted NCP3solution shows an aggregation band in the absorption spectra as increasing solution concentration due to the absence of the out-of-plane linker to prevent massive aggregation (black arrow, **Figure 4.1d**).

The alignment properties reflect the trend in UV-vis absorption of the three CPs very well (**Figure 4.1e**). NCP2 and NCP3 which lack of one required design parameter each exhibit

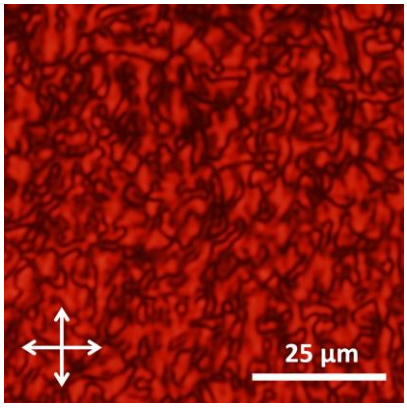

Figure 4.2 Liquid crystalline behavior of concentrated NCP1 solution under crossed polarizer. Highly concentrated NCP1 solution (ca. 250 mg·ml^{-1}) exhibits birefringence under crossed polarizer.

negligible alignment under a shear flow (dichroic ratio ~1). However, even though new building block of CP was applied, NCP1 that satisfies all three design requirements shows lyotropic LC behavior in highly concentrated solution (ca. 250 mg·ml^{-1}, **Figure 4.2**) and is aligned along the flow field direction with dichroic ratio of 4.67 (**Figure 4.1e**, by contact coating, blade speed of 25 µm·sec^{-1}). Therefore, we conclude that the suggested CP design principles are generally applicable to different type of building blocks for directed alignment of CPs.

To provide better insight on the material design for directed CP alignment beyond the three established design parameters, we further investigated other possible design factors that can affect the alignment properties of CPs. Especially, in this work, we focused on the effect of the structural factors of the bulky side chains and the concentration-induced planarization unit. As described above, the branched bulky side chains, stretching out-of-plane direction from the CP main chain, are essential to prevent massive aggregation which restricts chain mobility during the alignment process. However, it is still not conclusive what kind of side chain structure is beneficial for CPs to be aligned; is the branching point of the bulky out-of plane side chain also important? To answer this question, NCP4 is designed and synthesized by substituting 2-ethylhexyl side chains of NCP1 with 5-methylhexyl side chains (**Figure 4.3a**). Interestingly, NCP4 with 5-methylhexyl side chains shows a distinct aggregation band at ca. 590 nm in its UV-vis absorption spectrum even in a diluted solution (**Figure 4.3b**), while no aggregation band is

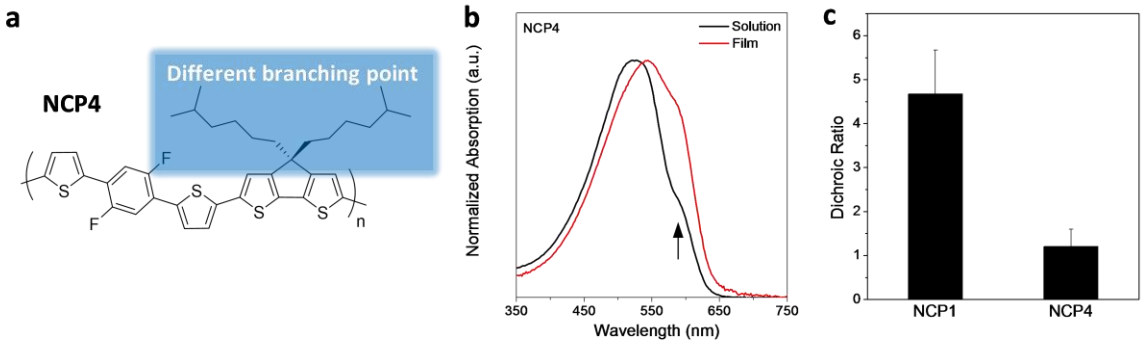

Figure 4.3 CP design, optical and alignment properties of CP with different side chain branching location. (a) Chemical structure of NCP4. (b) UV-vis absorption spectra of NCP4 solution and film. (c) Dichroic ratio of aligned CP films.

observed from the NCP1 solution (**Figure 4.1b**). Consequently, NCP4 does not show directed alignment under an applied shear flow (**Figure 4.3c**). The difference in the alignment property between NCP1 and NCP4 is attributed to the different branching point of the side chains. If the branch junction is near the conjugated backbone like the 2-ethylhexyl of NCP1, the side chains likely provide good enough steric hindrance so as to efficiently prevent π-π stacking between CP main chains. In contrast, 5-methylhexyl side chains of NCP4 which have the branching points far from the conjugated backbone is less effective in preventing π-π interaction between CP backbones. Therefore, in the stage of CP design, the structure of the bulky side chains is also crucial factor to accomplish alignment of CP chains.

From the comparison between NCP1 and NCP2, it is confirmed that the concentration-induced planar conformation of CP backbone is vital for CP alignment. However, the role of the concentration-induced planarization unit (S-F interaction building block) is not fully understood; what if CPs have an intrinsically planar conformation from the solution state? In contrast to CP1 and NCP1, which would have a non-planar conformation caused by the large thienyl-phenyl dihedral angle in a diluted solution, NCP5 and NCP6 have an intrinsically planar polythiophene

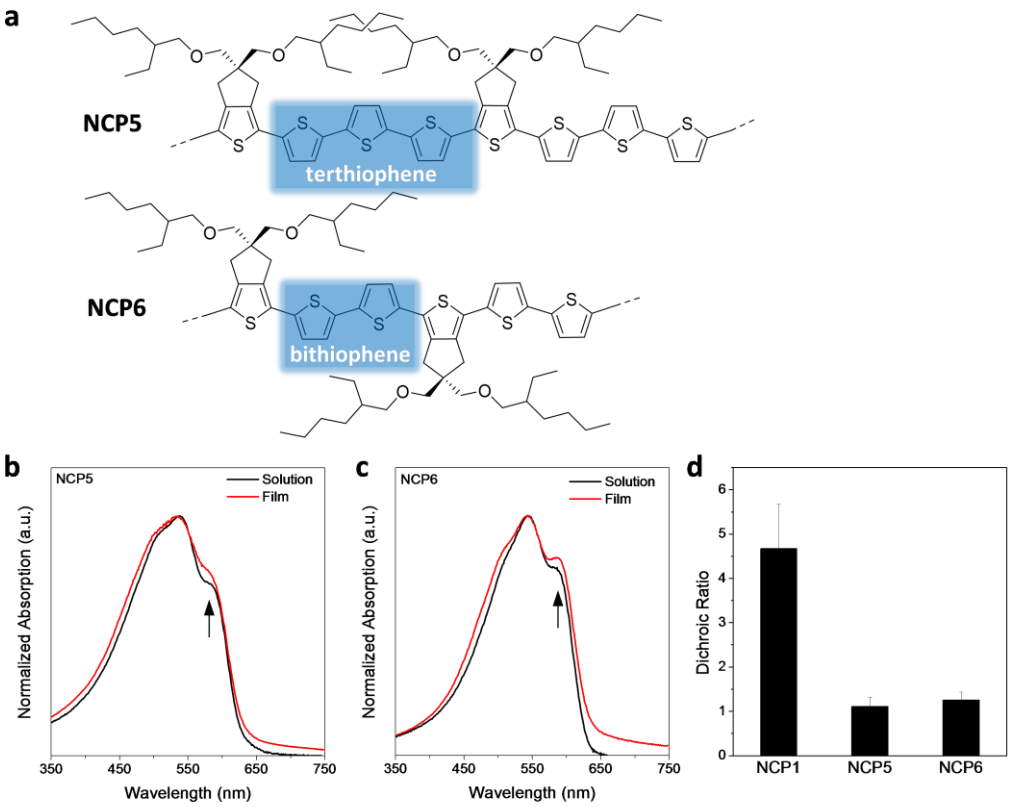

Figure 4.4 CP design, optical and alignment properties of CPs without concentration-induced planarization unit. (a) Chemical structure of NCP5 and NCP6. (b–c) UV-vis absorption spectra of (b) NCP5 and (c) NCP6. (e) Dichroic ratio of aligned CP films.

backbone (**Figure 4.4a**). The variation between NCP5 and NCP6 is a number of thienyl groups between the cyclopenta[*c*]thiophene units to which side chains are attached, that affects the spatial location of the side chains relative to the polymer backbone. NCP5 having the terthiophene building block is designed to maintain the distance between the side chain linked cyclopenta[*c*]thiophene units similar to CP1. While all side chains of NCP5 locate at the same side of the conjugated backbone (**Figure 4.4a**), NCP6 with bithiophene unit has its side chains alternatingly on the opposite sides of the main chain (**Figure 4.4a**). From the absorption spectra of both CPs in solution, strong aggregation band is observed at ca. 580 nm (black arrows, **Figure 4.4, b** and **c**). No additional red-shift in absorption λ_{max} is observed in film compared to that of

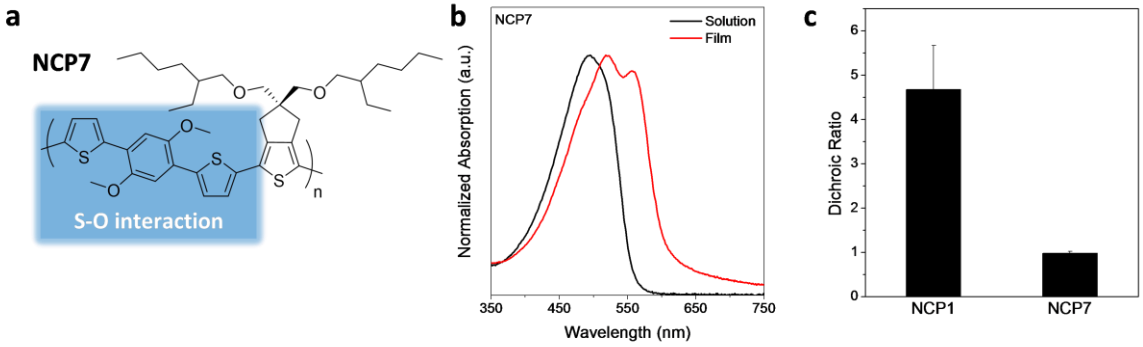

Figure 4.5 CP design, optical and alignment properties of CP with different concentration-induced planarization group. (a) Chemical structure of NCP7. (b) UV-vis absorption spectra of NCP7. (e) Dichroic ratio of aligned CP films.

solution because both CPs retain a planar conformation from the solution state. As the consequence, these two CPs do not exhibit any alignment under a shear flow (**Figure 4.4d**), which supports that a concentration-induced planarization unit is an important design factor to prevent massive aggregation of CPs and provide alignment capability to CPs.

Furthermore, we investigated a new intramolecular interaction analogous to the S-F interaction. We incorporated S-O interactions into the NCP7 to examine its capability as for the concentration-induced planarization function and its effect on the CP alignment (**Figure 4.5a**).[41–44] NCP7 exhibits a very similar UV-vis absorption trait of CP1[40] and NCP1, manifesting the effectiveness of the S-O interaction for the concentration-induced planarization; no

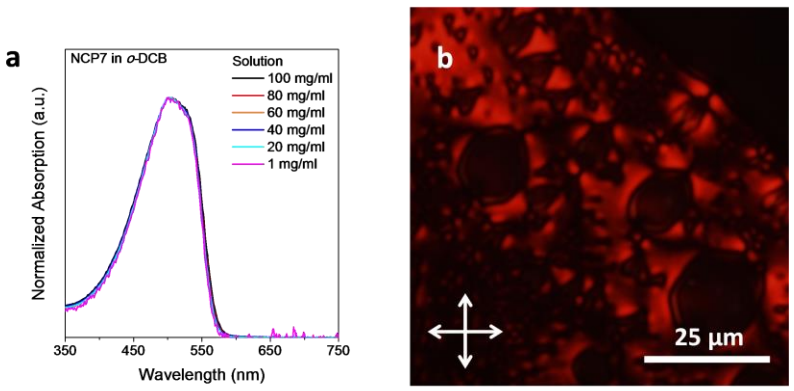

Figure 4.6 Optical properties and birefringence of NCP7 solution. (a) UV-vis absorption spectra of NCP7 solutions with different concentration. (b) Birefringent texture of the highly concentrated NCP7 solution (over 200 mg·ml^{-1}) under crossed polarizer.

aggregation band is observed in solution, even in highly concentrated solutions (~100 mg·ml^{-1}), and red-shifted absorption λ_{max} (~23 nm) is observed in film (**Figure 4.5b** and **Figure 4.6a**). However, NCP7 shows no alignment under contact coating (**Figure 4.5c**), nevertheless of the observed clear birefringence under crossed polarizer implying LC formation (**Figure 4.6b**). This discrepancy likely stems from the wettability (surface energy) difference between NCP7 and CP1 (or NCP1). The CP1 and NCP1 have two fluorine atoms having a low surface energy, different from NCP7 bearing two methoxy groups. This surface energy difference might largely affect the wettability and arrangement of the polymer chains on a substrate and makes NCP7 to respond differently under the contact coating condition. Indeed, an interesting result has been published recently showing that the CP arrangement on a substrate is distinctly differentiated as incorporated functional groups on CP analogue differ. Cho *et al.* reported that the substituting fluoride functional groups with methoxy groups converted the CP arrangement from edge-on to face-on on a substrate.[41] Therefore, the result implies that the fluorine atoms in the CP analogue influence on the effective alignment of CPs by providing suitable wettability and arrangement relative to the substrate.

4.3. Conclusion

In summary, the molecular design principles for directed CP alignment are systematically validated and expanded with seven newly designed polymers. The universal applicability of the previous identified design rules are confirmed with NCP1, NCP2 and NCP3 that are designed based on the three design parameters; (1) concentration-induced planarization unit, and (2) bulky side chains linked to (3) a tetrahedral carbon. From the UV-vis absorption and the alignment characteristics, we confirmed that various CPs can be aligned under a shear flow if the CP

satisfies all three design rules. We have also additionally examined other molecular design factors beyond the established three design rules to provide better insight on the material design for CP alignment. The side chain branching point turned out to be critically important. Only if the branch junction is near the conjugated backbone, the side chains provide good enough steric hindrance to efficiently prevent π-π stacking between CP main chains. We also further examine the role of the concentration-induced planarization unit. CPs having an intrinsically planar conformation from the diluted solution are not free from π-π aggregation in solution, and thereby no alignment can be achieved. The role of S-F interaction unit for concentration induced planarization is further implied through the replacement of S-F with S-O intramolecular interaction. Even though NCP7 having the S-O interactions as the concentration induced chain planarization unit shows a LC phase, it does not align along the shear flow, strongly suggesting that the low surface energy of fluoride functional groups and its consequent low wetting property on a substrate also plays an imperative role on molecular orientation and directed alignment. The results provide insightful molecular design strategies for directed self-assembly and alignment of conjugated polymers to fully realize their anisotropic optoelectronic properties in various device applications.

4.4. Experimental Section

4.4.1. Methods

4.4.1.1. Spectroscopic Characterization

^{1}H-NMR spectrum was characterized by a Varian, Inova 500 (500 MHz) and Varian, MR400 (400 MHz) in $CDCl_3$ solution. Chemical shift values were recorded as parts per million relative to tetramethylsilane as an internal standard. Coupling constants were recorded in Hertz. Mass

spectra were recorded on an Agilent Q-TOF 6520 system using electron impact ionization (EI) and atmospheric-pressure chemical ionization (APCI) in positive ion detection mode. UV-visible absorption spectra were measured on a Varian Cary50 UV/Vis spectrophotometer. Photoluminescence of contact coated CP films were measured to verify dichroic ratio by mean of the ratio of polarized PL intensity, using PTI QuantaMasterTM spectrofluorometers equipped with linear polarizer.

4.4.1.2. Contact Coating of CP Film

The CP solutions were prepared in a concentration of 2.5 $mg \cdot ml^{-1}$ in *o*-dichlorobenzene, containing 5 vol% of additive (1,8-octanedithiol). Substrates were cleaned by sonication in a sequence of water, acetone, and isopropanol for 15 min each, followed by UV/O_3 treatment for 10 min (UV/Ozone ProCleaner, BioForce Nanosciences). The cleaned substrate was placed on a hot stage, and the gap between substrate and contact coating blade was controlled as 50 μm with standard polyimide film including micro-gauge. The CP solution was spread onto the substrate, and coated by moving blade (speed: 25 $\mu m \cdot sec^{-1}$) at 140 ^{o}C.

4.4.2. Materials and Synthesis

All the chemicals and solvents for the synthesis were purchased from commercial suppliers (TCI, Acros, Sigma-Aldrich, and Fisher Sci.). The syntheses of monomers were conducted following previously described synthetic routes.[40,45–50]

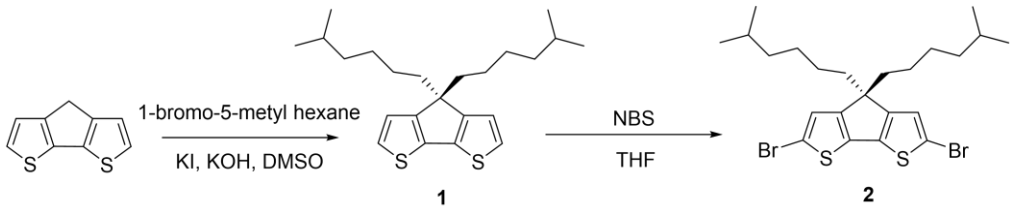

Figure 4.7 Synthetic route of a monomer for NCP4.

4.4.2.1. Synthesis of 4,4-bis(5-methylhexyl)-4H-cyclopenta[2,1-b:3,4-b']dithiophene [1]

4H-cyclopenta[2,1-b:3,4-b']dithiophene (0.2 g, 1.12 mmol), 1-bromo-5-metyl hexane (0.442 g, 2.47 mmol), potassium iodide (0.013 g, 0.076 mmol) were added to dimethyl sulfoxide (20 ml). The solution was cooled down to 0 ^{o}C followed by addition of potassium hydroxide (0.201 g, 3.59 mmol) in small portions. After stirring overnight at room temperature, the reaction mixture was poured into water and extracted with methylene chloride. The organic phase was dried over $MgSO_4$, and solvent was evaporated in *vacuo*. Column chromatography using hexane as eluent gave yellowish liquid as product. 0.301 g (72%). ^{1}H NMR (400 MHz, CDCl3): δ 7.15 (d, J=4.9 Hz, 2 H), 6.94 (d, J=4.9 Hz, 2 H), 1.85 – 1.81 (m, 4H), 1.44 – 1.36 (m, 2H) 1.15 – 1.06 (m, 4H) 1.05 – 0.99 (m, 4H), 0.95 – 0.88 (m, 4H), 0.79 (d, J=6.7 Hz, 12H). MS m/z (EI+, relative intensity): 374 (M^+, 100), 289 (25), 275 (25), 203 (23), 191 (32), 179 (33), 57 (23), 43 (27). HRMS (EI+) calcd. for $C_{23}H_{34}S_2$ (M^+) 374.2102, found 374.2106.

4.4.2.2. Synthesis of 2,6-dibromo-4,4-bis(5-methylhexyl)-4H-cyclopenta[2,1-b:3,4-b']dithiophene [2]

Compound 1 (0.2 g, 0.534 mmol) was added to dry tetrahydrofuran (15 ml). Under Ar condition, the mixture was cooled down to 0 ^{o}C, and N-bromosuccinimide (0.209 g, 1.17 mmol) was added. After stirring overnight at room temperature, the reaction mixture was poured into

water and extracted with methylene chloride. The organic phase was dried over $MgSO_4$, and solvent was evaporated in *vacuo*. Column chromatography using hexane as eluent gave yellowish liquid as product. 0.245 g (86%). ^{1}H NMR (400 MHz, CDCl3): δ 6.93 (s, 2 H), 1.80 – 1.74 (m, 4H), 1.45 – 1.38 (m, 2H) 1.16 – 1.08 (m, 4H) 1.08 – 0.99 (m, 4H), 0.95 – 0.86 (m, 4H), 0.81 (d, J=6.6 Hz, 12H). MS m/z (EI+, relative intensity): 532 (M^+, 100), 453 (11), 354 (15), 283 (18), 270 (14), 84 (35), 57 (54), 43 (76). HRMS (EI+) calcd. for $C_{23}H_{32}Br_2S_2$ (M^+) 530.0312, found 530.0310.

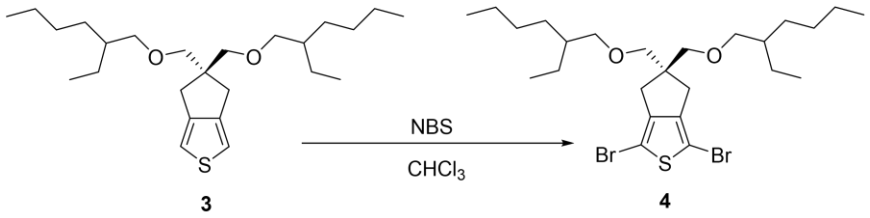

Figure 4.8 Synthetic route of a monomer for NCP5, 6, 7.

4.4.2.3. Synthesis of 1,3-dibromo-5,5-bis(((2-ethylhexyl)oxy)methyl)-5,6-dihydro-4H-cyclopenta[c]thiophene [4]

Compound 3 is prepared as previously described manner.[40] Compound 3 (2 g, 4.89 mmol) was added to dry chloroform (25 ml). Under Ar condition, the mixture was cooled down to 0 ^{o}C, and N-bromosuccinimide (2.18 g, 12.23 mmol) was added. After stirring 4 hr at room temperature, the reaction mixture was poured into water and extracted with methylene chloride. The organic phase was dried over $MgSO_4$, and solvent was evaporated in *vacuo*. Column chromatography using mixed solvent (methylene chloride : hexane = 1 : 1) as eluent gave colorless liquid as product. 2.397 g (87%). ^{1}H NMR (500 MHz, CDCl3): δ 3.32 (s, 4 H), 3.28 (d, J=6.0 Hz, 4 H), 2.53 (s, 4H), 1.50 – 1.45 (m, 2H), 1.42 – 1.26 (m, 16H), 0.91 – 0.84 (m, 12H).

MS m/z (APCI+, relative intensity): 567 (M^++1, 100), 409 (5), 279 (10), 205 (5), 149 (29), 113 (19). HRMS (APCI+) calcd. for $C_{25}H_{42}Br_2O_2S$ (M^++1) 565.1345, found 565.1340.

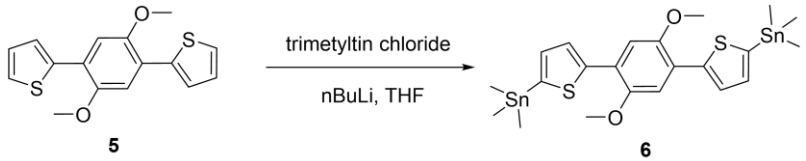

Figure 4.9 Synthetic route of a monomer for NCP7.

4.4.2.4. Synthesis of ((2,5-dimethoxy-1,4-phenylene)bis(thiophene-5,2-diyl))bis(trimethylstannane) [6]

Compound 5 is prepared as previously described manner.[47] Under Ar condition, compound 5 (0.5 g, 1.65 mmol) was added to dry tetrahydrofuran. At 0 ^oC, n-butyl lithium (2.5 M in hexane, 1.52 ml) was added into solution dropwise. The reaction mixture was stirred for 30 min at room temperature, and trimethyltin chloride (1 M in tetrahydrofuran, 4.13 ml) was added. The mixture was further stirred overnight at room temperature. Then, it was poured into water and extracted with chloroform. The organic phase was dried over $MgSO_4$, and solvent was evaporated in *vacuo*. Recrystallization was conducted in ethanol, and bright yellow crystals were obtained as product. 0.54 g (52%). ^1H NMR (500 MHz, CDCl3): δ 7.63 (d, J=3.5 Hz, 2 H), 7.23 (s, 2 H), 7.19 (d, J=3.5 Hz, 2 H), 3.932 (s, 6H), 0.39 (s, 18H). MS m/z (EI+, relative intensity): 628 (M^+, 100), 466 (14), 299 (32), 165 (16), 84 (17), 49 (25). HRMS (APCI+) calcd. for $C_{22}H_{30}O_2S_2Sn_2$ (M^++1) 628.9804, found 628.9786.

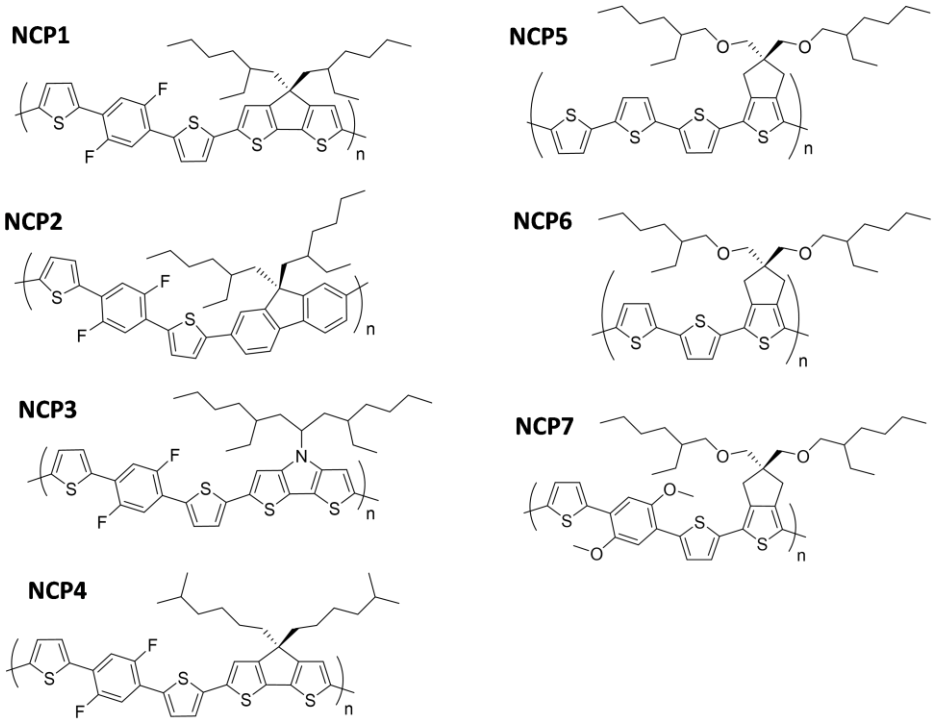

Figure 4.10 Chemical structures of the synthesized CPs.

4.4.2.5. General Procedure of Stille Type Polymerization

Under Ar conditions, the prepared monomers, compound 4 and 6 for NCP7 for example, were added (1:1 in equivalent) into an anhydrous toluene and N,N-dimethylformamide mixed solvent (5:1 in volume). After adding 5 mol% of tetrakis(triphenylphosphine)palladium (0), the reaction mixture was heated up to 120 ^{o}C and stirred for 12 hours. End-capping was further conducted by adding 2-tributylstannyl thiophene and stirring for 6 hours, followed by adding 2-bromothiophene and stirring for another 6 hours. The final CPs were collected via reprecipitation of the reaction mixture into methanol. The precipitated polymers were collected through a nylon filter, and further washed with hexane, methanol, and acetone in a soxhlet apparatus to remove the small molecular weight portion and catalyst residue. Only the part of CPs soluble to chloroform and toluene was obtained. For the alignment test, CPs were further purified through a column chromatography using Cellite and Florosil as a packing materials. The molecular weights

of the synthesized polymers were measured by mean of gel permeation chromatography (GPC): **NCP1** (M_n: 6782, M_w: 8766, PDI: 1.293), **NCP2** (M_n: 2458, M_w: 4166, PDI: 1.695), **NCP3** (M_n: 7260, M_w: 9733, PDI: 1.341), **NCP4** (M_n: 6969, M_w: 10421, PDI: 1.495), **NCP5** (M_n: 8072, M_w: 16680, PDI: 2.066), **NCP6** (M_n: 8227, M_w: 10507, PDI: 1.277), **NCP7** (M_n: 20188, M_w: 38078, PDI: 1.886)

4.5. Author Contribution

K. Chung, B.-G. Kim, J. Kim, D. S. Yang, G. Jang, M. S. Kwon, T. S. Lee, J. Kim, Molecular design principles for directed alignment of conjugated polymers. *Manuscript in preparation*

Kyeongwoon Chung, Bong-Gi Kim and Jinsang Kim designed the project, and Jinsang Kim directed the project. Kyeongwoon Chung, Bong-Gi Kim, Jongho Kim, Da Seul Yang, Geunseok Jang synthesized the series of CPs. Optical and alignment properties of CPs are analyzed by Kyeongwoon Chung and Bong-Gi Kim. Kyeongwoon Chung and Jinsang Kim wrote the manuscript for publication, and all other authors had input.

4.6. References and Notes

1. J. Lee, H. Jun, J. Kim, Polydiacetylene-Liposome Microarrays for Selective and Sensitive Mercury(II) Detection. *Adv. Mater.* **21,** 3674–3677 (2009).
2. J. Kim, D. T. McQuade, S. K. McHugh, T. M. Swager, Ion-Specific Aggregation in Conjugated Polymers: Highly Sensitive and Selective Fluorescent Ion Chemosensors. *Angew. Chemie* **112,** 4026–4030 (2000).
3. K. Lee, L. K. Povlich, J. Kim, Recent advances in fluorescent and colorimetric conjugated polymer-based biosensors. *Analyst* **135,** 2179–2189 (2010).
4. J. Lee, S. Seo, J. Kim, Colorimetric Detection of Warfare Gases by Polydiacetylenes Toward Equipment-Free Detection. *Adv. Funct. Mater.* **22,** 1632–1638 (2012).
5. H.-A. Ho, M. Boissinot, M. G. Bergeron, G. Corbeil, K. Doré, D. Boudreau, M. Leclerc, Colorimetric and Fluorometric Detection of Nucleic Acids Using Cationic Polythiophene Derivatives. *Angew. Chemie Int. Ed.* **41,** 1548–1551 (2002).
6. B. Yoon, J. Lee, I. S. Park, S. Jeon, J. Lee, J.-M. Kim, Recent functional material based

approaches to prevent and detect counterfeiting. *J. Mater. Chem. C* **1,** 2388 (2013).
7. B. Yoon, D.-Y. Ham, O. Yarimaga, H. An, C. W. Lee, J.-M. Kim, Inkjet printing of conjugated polymer precursors on paper substrates for colorimetric sensing and flexible electrothermochromic display. *Adv. Mater.* **23,** 5492–5497 (2011).
8. B. Yoon, H. Shin, O. Yarimaga, D.-Y. Ham, J. Kim, I. S. Park, J.-M. Kim, An inkjet-printable microemulsion system for colorimetric polydiacetylene supramolecules on paper substrates. *J. Mater. Chem.* **22,** 8680 (2012).
9. K. Chung, A. McAllister, D. Bilby, B.-G. Kim, M. S. Kwon, E. Kioupakis, J. Kim, Designing interchain and intrachain properties of conjugated polymers for latent optical information encoding. *Chem. Sci.* **6,** 6980–6985 (2015).
10. H. N. Tsao, K. Müllen, Improving polymer transistor performance via morphology control. *Chem. Soc. Rev.* **39,** 2372–2386 (2010).
11. M. Gross, D. Muller, H. Nothofer, U. Scherf, D. Neher, C. Brauchle, K. Meerholz, Improving the performance of doped pi-conjugated polymers for use in organic light-emitting diodes. *Nature* **405,** 661–665 (2000).
12. S. Günes, H. Neugebauer, N. S. Sariciftci, Conjugated polymer-based organic solar cells. *Chem. Rev.* **107,** 1324–1338 (2007).
13. K. Chung, Y. Yu, M. S. Kwon, J. Swets, J. Kim, J. H. Youk, Assembly and alignment of conjugated polymers: materials design, processing, and applications. *MRS Commun.* **5,** 169–189 (2015).
14. V. Cimrová, M. Remmers, D. Neher, G. Wegner, Polarized light emission from LEDs prepared by the Langmuir-Blodgett technique. *Adv. Mater.* **8,** 146–149 (1996).
15. J. Kim, S. K. McHugh, T. M. Swager, Nanoscale Fibrils and Grids: Aggregated Structures from Rigid-Rod Conjugated Polymers. *Macromolecules* **32,** 1500–1507 (1999).
16. T. Kanetake, K. Ishikawa, T. Koda, Y. Tokura, K. Takeda, Highly oriented polydiacetylene films by vacuum deposition. *Appl. Phys. Lett.* **51,** 1957 (1987).
17. H. Heil, T. Finnberg, N. von Malm, R. Schmechel, H. von Seggern, The influence of mechanical rubbing on the field-effect mobility in polyhexylthiophene. *J. Appl. Phys.* **93,** 1636–1641 (2003).
18. L. Biniek, S. Pouget, D. Djurado, E. Gonthier, K. Tremel, N. Kayunkid, E. Zaborova, N. Crespo-Monteiro, O. Boyron, N. Leclerc, S. Ludwigs, M. Brinkmann, High-Temperature Rubbing: A Versatile Method to Align π-Conjugated Polymers without Alignment Substrate. *Macromolecules* **47,** 3871–3879 (2014).
19. Z. Zheng, K.-H. Yim, M. S. M. Saifullah, M. E. Welland, R. H. Friend, J.-S. Kim, W. T. S. Huck, Uniaxial alignment of liquid-crystalline conjugated polymers by nanoconfinement. *Nano Lett.* **7,** 987–992 (2007).
20. M. Aryal, K. Trivedi, W. W. Hu, Nano-confinement induced chain alignment in ordered P3HT nanostructures defined by nanoimprint lithography. *ACS Nano* **3,** 3085–3090 (2009).
21. G. Ding, Y. Wu, Y. Weng, W. Zhang, Z. Hu, Solvent-Assistant Room Temperature Nanoimprinting-Induced Molecular Orientation in Poly(3-hexylthiophene) Nanopillars. *Macromolecules* **46,** 8638–8643 (2013).
22. C. De Rosa, C. Park, E. Thomas, B. Lotz, Microdomain patterns from directional eutectic solidification and epitaxy. *Nature* **405,** 433–437 (2000).
23. M. Brinkmann, J.-C. Wittmann, Orientation of Regioregular Poly(3-hexylthiophene) by Directional Solidification: A Simple Method to Reveal the Semicrystalline Structure of a

Conjugated Polymer. *Adv. Mater.* **18,** 860–863 (2006).
24. C. Müller, M. Aghamohammadi, S. Himmelberger, P. Sonar, M. Garriga, A. Salleo, M. Campoy-Quiles, One-Step Macroscopic Alignment of Conjugated Polymer Systems by Epitaxial Crystallization during Spin-Coating. *Adv. Funct. Mater.* **23,** 2368–2377 (2013).
25. B. Dörling, V. Vohra, T. T. Dao, M. Garriga, H. Murata, M. Campoy-Quiles, Uniaxial macroscopic alignment of conjugated polymer systems by directional crystallization during blade coating. *J. Mater. Chem. C* **2,** 3303 (2014).
26. C.-C. Kuo, C.-T. Wang, W.-C. Chen, Highly-Aligned Electrospun Luminescent Nanofibers Prepared from Polyfluorene/PMMA Blends: Fabrication, Morphology, Photophysical Properties and Sensory Applications. *Macromol. Mater. Eng.* **293,** 999–1008 (2008).
27. M. Campoy-Quiles, Y. Ishii, H. Sakai, H. Murata, Highly polarized luminescence from aligned conjugated polymer electrospun nanofibers. *Appl. Phys. Lett.* **92,** 213305 (2008).
28. K. Yin, L. Zhang, C. Lai, L. Zhong, S. Smith, H. Fong, Z. Zhu, Photoluminescence anisotropy of uni-axially aligned electrospun conjugated polymer nanofibers of MEH-PPV and P3HT. *J. Mater. Chem.* **21,** 444 (2011).
29. H. Sirringhaus, R. J. Wilson, R. H. Friend, M. Inbasekaran, W. Wu, E. P. Woo, M. Grell, D. D. C. Bradley, Mobility enhancement in conjugated polymer field-effect transistors through chain alignment in a liquid-crystalline phase. *Appl. Phys. Lett.* **77,** 406 (2000).
30. H.-R. Tseng, L. Ying, B. B. Y. Hsu, L. A. Perez, C. J. Takacs, G. C. Bazan, A. J. Heeger, High mobility field effect transistors based on macroscopically oriented regioregular copolymers. *Nano Lett.* **12,** 6353–6357 (2012).
31. H.-R. Tseng, H. Phan, C. Luo, M. Wang, L. A. Perez, S. N. Patel, L. Ying, E. J. Kramer, T.-Q. Nguyen, G. C. Bazan, A. J. Heeger, High-mobility field-effect transistors fabricated with macroscopic aligned semiconducting polymers. *Adv. Mater.* **26,** 2993–2998 (2014).
32. C. Luo, A. K. K. Kyaw, L. A. Perez, S. Patel, M. Wang, B. Grimm, G. C. Bazan, E. J. Kramer, A. J. Heeger, General strategy for self-assembly of highly oriented nanocrystalline semiconducting polymers with high mobility. *Nano Lett.* **14,** 2764–2771 (2014).
33. J. Wu, A. F. Gross, S. H. Tolbert, Host−Guest Chemistry Using an Oriented Mesoporous Host: Alignment and Isolation of a Semiconducting Polymer in the Nanopores of an Ordered Silica Matrix. *J. Phys. Chem. B* **103,** 2374–2384 (1999).
34. W. C. Molenkamp, M. Watanabe, H. Miyata, S. H. Tolbert, Highly polarized luminescence from optical quality films of a semiconducting polymer aligned within oriented mesoporous silica. *J. Am. Chem. Soc.* **126,** 4476–4477 (2004).
35. I. B. Martini, I. M. Craig, W. C. Molenkamp, H. Miyata, S. H. Tolbert, B. J. Schwartz, Controlling optical gain in semiconducting polymers with nanoscale chain positioning and alignment. *Nat. Nanotechnol.* **2,** 647–652 (2007).
36. D. Iacopino, P. Lovera, A. O'Riordan, G. Redmond, Highly polarized luminescence from β-phase-rich poly(9,9-dioctylfluorene) nanofibers. *J. Phys. Chem. A* **118,** 5437–5442 (2014).
37. T. W. Hagler, K. Pakbaz, K. F. Voss, A. J. Heeger, Enhanced order and electronic delocalization in conjugated polymers oriented by gel processing in polyethylene. *Phys. Rev. B* **44,** 8652–8666 (1991).
38. C. Weder, C. Sarwa, C. Bastiaansen, P. Smith, Highly polarized luminescence from

oriented conjugated polymer/polyethylene blend films. *Adv. Mater.* **9,** 1035–1039 (1997).
39. Z. Zhu, T. M. Swager, Conjugated Polymer Liquid Crystal Solutions: Control of Conformation and Alignment. *J. Am. Chem. Soc.* **124,** 9670–9671 (2002).
40. B.-G. Kim, E. J. Jeong, J. W. Chung, S. Seo, B. Koo, J. Kim, A molecular design principle of lyotropic liquid-crystalline conjugated polymers with directed alignment capability for plastic electronics. *Nat. Mater.* **12,** 659–664 (2013).
41. H. G. Kim, B. Kang, H. Ko, J. Lee, J. Shin, K. Cho, Synthetic Tailoring of Solid-State Order in Diketopyrrolopyrrole-Based Copolymers via Intramolecular Noncovalent Interactions. *Chem. Mater.* **27,** 829–838 (2015).
42. J. A. Irvin, I. Schwendeman, Y. Lee, K. A. Abboud, J. R. Reynolds, Low-oxidation-potential conducting polymers derived from 3,4-ethylenedioxythiophene and dialkoxybenzenes. *J. Polym. Sci. Part A Polym. Chem.* **39,** 2164–2178 (2001).
43. H. Huang, Z. Chen, R. Ponce Ortiz, C. Newman, H. Usta, S. Lou, J. Youn, Y.-Y. Noh, K.-J. Baeg, L. X. Chen, A. Facchetti, T. Marks, Combining electron-neutral building blocks with intramolecular 'conformational locks' affords stable, high-mobility p- and n-channel polymer semiconductors. *J. Am. Chem. Soc.* **134,** 10966–10973 (2012).
44. X. Guo, J. Quinn, Z. Chen, H. Usta, Y. Zheng, Y. Xia, J. W. Hennek, R. P. Ortiz, T. J. Marks, A. Facchetti, Dialkoxybithiazole: a new building block for head-to-head polymer semiconductors. *J. Am. Chem. Soc.* **135,** 1986–1996 (2013).
45. J. C. Bijleveld, M. Shahid, J. Gilot, M. M. Wienk, R. A. J. Janssen, Copolymers of Cyclopentadithiophene and Electron-Deficient Aromatic Units Designed for Photovoltaic Applications. *Adv. Funct. Mater.* **19,** 3262–3270 (2009).
46. R. Grisorio, C. Piliego, M. Striccoli, P. Cosma, P. Fini, G. Gigli, P. Mastrorilli, G. P. Suranna, C. F. Nobile, Influence of Keto Groups on the Optical, Electronic, and Electroluminescent Properties of Random Fluorenone-Containing Poly(fluorenylene-vinylene)s. *J. Phys. Chem. C* **112,** 20076–20087 (2008).
47. P. Hermet, S. Lois-Sierra, J.-L. Bantignies, S. Rols, J.-L. Sauvajol, F. Serein-Spirau, J.-P. Lère-Porte, J. J. E. Moreau, Lattice Dynamics of Oligo(phenylenethienylene)s: A Far-Infrared and Inelastic Neutron Scattering Study. *J. Phys. Chem. B* **113,** 4497-4202 (2009).
48. C.-H. Cho, H. Kang, T. E. Kang, H.-H. Cho, S. C. Yoon, M.-K. Jeon, B. J. Kim, Controlling side-chain density of electron donating polymers for improving their packing structure and photovoltaic performance. *Chem. Commun.* **47,** 3577–3579 (2011).
49. E. Zhou, M. Nakamura, T. Nishizawa, Y. Zhang, Q. Wei, K. Tajima, C. Yang, K. Hashimoto, Synthesis and Photovoltaic Properties of a Novel Low Band Gap Polymer Based on N-Substituted Dithieno[3,2- b :2′,3′- d]pyrrole. *Macromolecules* **41,** 8302–8305 (2008).
50. C. J. Mueller, E. Gann, C. R. McNeill, M. Thelakkat, Influence of fluorination in π-extended backbone polydiketopyrrolopyrroles on charge carrier mobility and depth-dependent molecular alignment. *J. Mater. Chem. C* **3,** 8916–8925 (2015).

CHAPTER 5

Highly Selective Alcohol and Water Sensor with Large Fluorescence Signal Contrast based on Solvent-Fluorophore-Substrate Interaction

5.1. Introduction

The characteristics of organic conjugated molecules are prone to be further affected by the environmental aspects such as physicochemical properties of a substrate on which the molecules are coated and interacting surrounding solvent molecules. In this chapter, a systematic investigation is described on the interactions of a rationally designed series of fluorescent molecules with a mesoporous silica substrate and solvents. We devised a novel optical sensor system by exploiting the controlled and distinct interactions between solvent-fluorophore-substrate, and demonstrated a large fluorescence signal contrast as well as high selectivity among various alcohols and water molecules.

Multiple tragic accidents had occurred in 2015 across the world and took lives of over several hundreds of people who drank fatal methanol-contaminated alcoholic beverages.[1,2] Different from ethanol, the primary ingredient in alcoholic beverages, methanol can cause blindness and may prove fatal even in small dose.[3] Even though differentiation of methanol from ethanol is an important issue of interest, due to the similarity in chemical structure as well as

properties it is highly challenging to distinguish them without using special chemical analysis instruments such as NMR and mass spectrometry.

Various approaches have been explored for selective detection of solvents and solvent vapors, and can be sorted into four categories based on their sensing mechanism; sorption,[4–10] solvatochromism,[11–16] chemical reaction,[14–21] and dilation.[22,23] The sorption-based sensors' sensory signal is mainly a current or resistance change when chemical adsorption or deactivation of adsorbed species, such as ionized oxygen molecule, occurs between two electrodes or under transistor geometry which is constructed with nanostructured materials, thin films, or composites.[4–10] Solvatochromic sensors utilize color and/or fluorescence gradation of the sensory molecules (or metal-organic frameworks) responding to the different solvent polarity.[11–16] The sensors based on chemical reaction refer to a system that exhibits color and/or fluorescence alteration by chemical reaction, reduction, oxidation, or metal-ion ligation of the sensory molecules upon binding with analytes.[14–21] As a dilation-based sensor, swelling-induced color change of polydiacetylene-polydimethylsiloxane composites and resistance change in carbon black-polymer composites have been demonstrated.[22,23] Even though these sensor systems have demonstrated efficient sensing of target analytes, they often require complicated device fabrication, sophisticated measurement or data processing, and customized material design for specific chemical reactions with analytes.

In this work, we present a novel optical sensor system that can unequivocally distinguish alcohols and water by utilizing controlled subtle interaction difference between a substrate, fluorescent organic molecules, and the liquid analytes. The devised sensor system based on solvent-fluorophore-substrate interactions is a new type of sensor allowing (i) cost-effective device fabrication by simple drop casting of fluorescent organic solution onto conventional silica

gel substrates as well as (ii) equipment-free visual detection of fluorescent signal change. The interaction between solvent-fluorophore-substrate can be finely controlled via gradual chemical structure modification of the fluorophore, diketopyrrolopyrrole (DPP) derivatives, which allows high selectivity among solvents having similar physicochemical properties such as ethanol, methanol, ethylene glycol, and water. Upon exposure to solvent analytes, the proposed sensor system undergoes an immediate and high-contrast fluorescence signal change.

5.2. Results and Discussion

Four fluorescent DPP derivatives were prepared for the new sensor system (**Figure 5.1a** and **Figure 5.2**, n=4, 8, 12, 16).[24] By simple drop casting of DPP derivative solution (10^{-3} M), the sensor system was successfully fabricated onto a mesoporous silica gel substrate that is conventionally used for thin layer chromatography (TLC). All four DPP derivatives on silica gel substrates exhibit bright green fluorescence under 365 nm UV light (**Figure 5.1b**). In contrast, depending on the chemical structure of the DPP derivatives the green fluorescence becomes dim red upon exposure to a certain solvent analyte, for example, water (**Figure 5.1b**). The proposed mechanism of solvent sensing is schematically illustrated in **Figure 5.1c**. The mesoporous silica gel substrate has strong polar (and/or hydrogen bonding) interaction with the DPP derivatives. Therefore, unless the amount of DPP derivatives on the silica gel substrate is too much, the strong interaction prevents the DPP molecules from aggregation and allows bright fluorescence from the isolated DPP molecules.[25,26] When the as-cast sensor device is dipped into a solvent, it shows two different types of response. A non-polar solvent will not be able to effectively interrupt the existing strong interaction between the adsorbed DPP molecules and the silica gel substrate, thereby the sensor device maintains its original bright green fluorescence. On the other

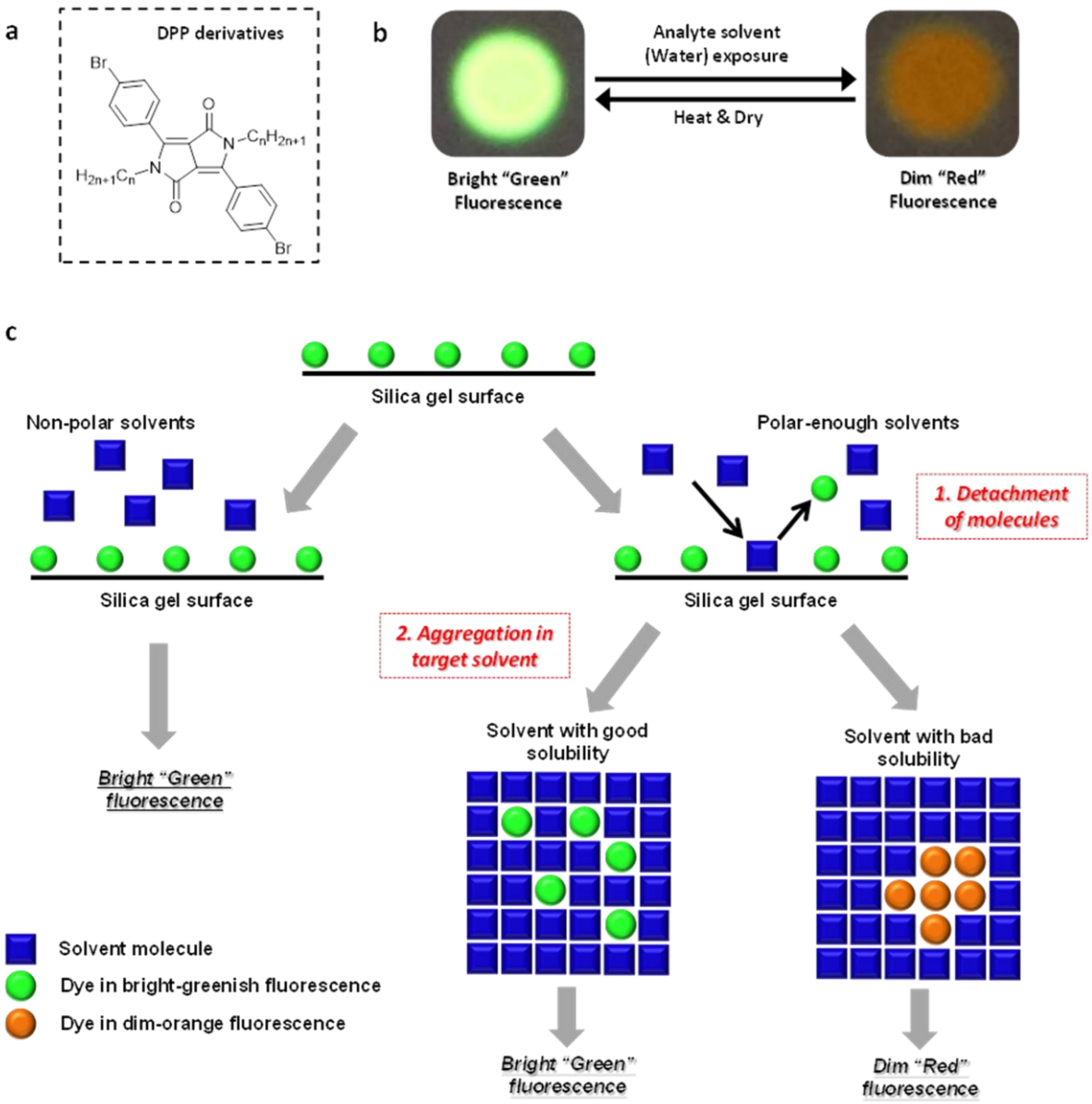

Figure 5.1 A novel sensor system based on subtle difference in interaction between solvent analyte, fluorescent molecule, and mesoporous silica gel substrate. (a) Chemical structure of fluorescent DPP derivatives (n = 4, 8, 12, 16). (b) Reversible fluorescent signal change of the system upon water exposure and drying (under 365nm UV light). (c) Proposed mechanism of fluorescence signal generation upon exposure to solvent analytes.

hand, a polar solvent (or a solvent having strong tendency to form hydrogen bonding) can disturb the existing interaction between the DPPs and the substrate, thereby detaching DPPs from the silica gel surface. Now the detached fluorescent DPP molecules will aggregate each other if the

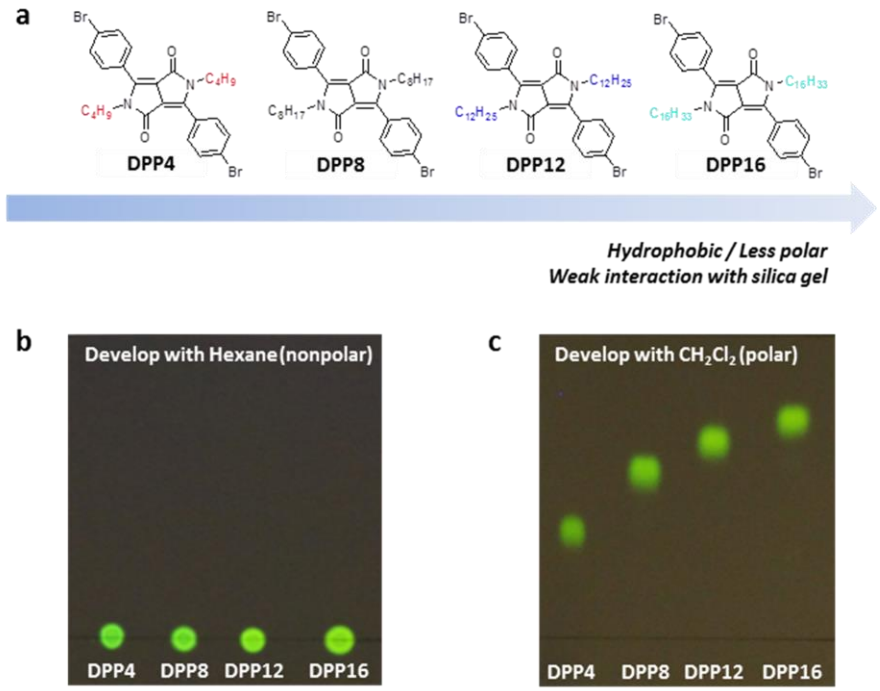

Figure 5.2 Development test of DPP derivatives on silica gel substrate with solvents of different polarity. (a) Chemical structure of fluorescent DPP derivatives utilized for the sensor system: DPP4 (n = 4 in Figure 5.1a), DPP8 (n = 8 in Figure 5.1a), DPP12 (n = 12 in Figure 5.1a), DPP16 (n = 16 in Figure 5.1a). (b) Development test with non-polar solvent (Hexane). (c) Development test with polar-enough solvent (dichloromethane). Images (b and c) were taken under 365 nm UV light.

solvent is a poor solvent, resulting in aggregation-induced fluorescence quenching while they remain in the same isolated state in a good solvent and ensuing bright green fluorescence.

To verify the proposed sensing mechanism, TLC development tests on a silica gel substrate with solvents of different polarity were conducted. As expected, a non-polar solvent, hexane, cannot interrupt the interaction between DPPs and the silica gel substrate, and hence causes no movement of DPP spots, which makes DPP spots retain bright green fluorescence (**Figure 5.2b**). In contrast, development with polar dichloromethane leads to upward movement of the DPP spots because dichloromethane breaks the interaction between DPP molecules and the substrate (**Figure 5.2c**). Since dichloromethane is a good solvent for the DPP derivatives, the spots on the silica gel substrate also maintain the bright green fluorescence. It is important to note that the

interaction between DPPs and the silica gel substrate can be successfully modified by modulating alkyl side chain length of DPP molecules without notable fluorescence emissive property change. As the alkyl chain length increases, from DPP4 (n = 4) to DPP16 (n = 16), molecules become more hydrophobic and less polar, which weakens their interaction with the silica gel substrate (**Figure 5.2a**). This trend is clearly manifested in the retention factor (Rf) value of DPP derivatives on the TLC development test with dichloromethane; the Rf value gradually increases with the increasing side chain length (**Figure 5.2c**). Since the modification of molecular interactions by chemical structure design can be equally applied to the interaction between DPPs and solvent molecules, we adapted the tunable interaction control between substrate-fluorophore-solvent for the development of a new optical sensory system to distinguish alcohols and water.

First, we optimized the amount of DPP molecules for the sensory unit preparation. The optimum concentration should allow DPPs to be isolated from each other for bright fluorescence emission in the as-cast state but still within close proximity to form aggregation once DPPs are detached from the surface of silica gel substrate by the analyte solvent for aggregation-induced quenching, resulting in large fluorescence emission change as a noticeable sensory signal. We tested three solution concentrations; 10^{-4} M, 10^{-3} M, and 10^{-2} M, and used water as a solvent analyte since water is a highly polar but non-solvent for DPPs. As one can see from **Figure 5.3** the fluorescence emission spectra of the as-cast sensory unit prepared with 10^{-4} M and 10^{-3} M solutions are essentially the same but that of the 10^{-2} M solution is 20 nm red-shifted, indication concentration-induced aggregation even in the as-cast state. Regarding the emission spectrum of the sensor after the water exposure, the sample prepared from 10^{-4} M solution does not exhibit notable fluorescence change even after solvent exposure likely because DPP molecules are

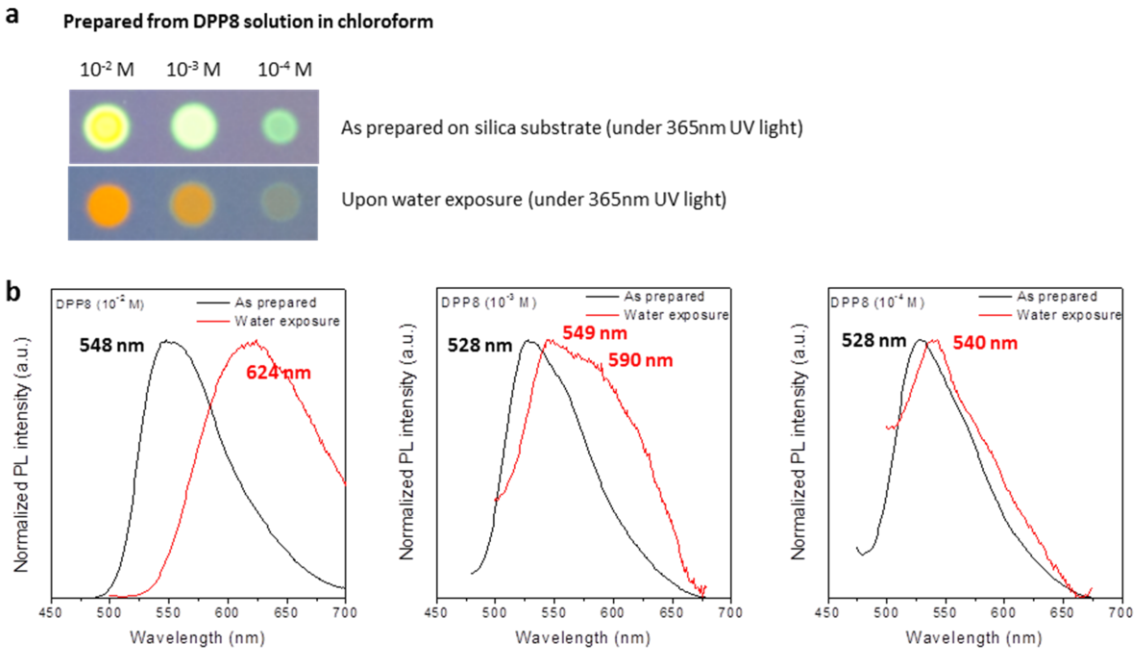

Figure 5.3 Molecular concentration dependent fluorescence of the sensors before and after exposure to water (target analyte). (a) Fluorescence images of the sensors prepared with DPP8 solution of 10^{-2} M, 10^{-3} M, and 10^{-4} M, respectively, before (as-prepared) and after exposure to water (under 365 nm UV light). (b) Normalized photoluminescence spectra of the sensors prepared with 10^{-2} M (left), 10^{-3} M (middle), and 10^{-4} M (right) DPP8 solution before and after exposure to water.

separated too far away from each other to form effective aggregation upon detached from the substrate (**Figure 5.3**). From the result, 10^{-3} M was identified as the optimum concentration of the DPP solutions to prepare the sensors and used for the investigation presented in this contribution.

Using water as a solvent analyte, the optical properties of the sensor system prepared with the four DPP derivatives were investigated. Apparent color and brightness change, from bright green to dim reddish fluorescence, is clearly observable to the naked eye upon water exposure for all four derivatives under 365 nm UV light (**Figure 5.4a**). We analyzed emission spectrum (**Figure 5.4b** and **Figure 5.5a**) and quantum yield (QY) (**Figure 5.4c**) of the sensors before and after the water exposure to find that the water exposed sensors exhibit a large QY drop accompanied by a

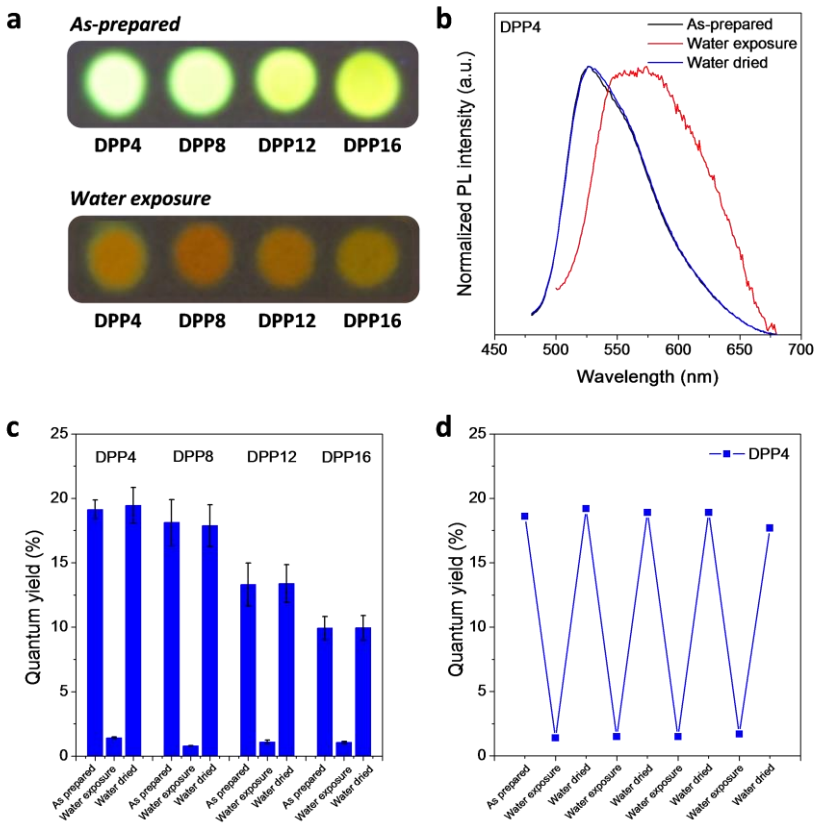

Figure 5.4 Optical properties of the sensor system. (a) Fluorescence images of the sensors made with the four DPP derivatives (DPP4, 8, 12, 16) before and after water (solvent analyte) exposure (under 365 nm UV light). (b) Photoluminescence spectrum of a DPP4 sensor in as-prepared, water exposure, and dried state. (c) Fluorescence quantum yield of the DPP sensors (DPP4, 8, 12, 16) in as-prepared, water exposure, and water dried state. (d) Fluorescence quantum yield trend of a DPP4 sensor upon multiple water exposure and drying.

red-shifted and broaden PL spectrum compared to the as-prepared sensor. Furthermore, the original bright green fluorescence was completely recovered by drying of water. After a brief heat treatment at 150 ^{o}C, the sensors showed the identical PL spectrum to that of the as-prepared sensor (**Figure 5.4b** and **Figure 5.5a**) as well as a fully recovered QY (**Figure 5.4c**). Even after multiple water-dipping and drying cycles, reversible QY quenching and restoration was maintained (**Figure 5.4d** and **Figure 5.5b**).

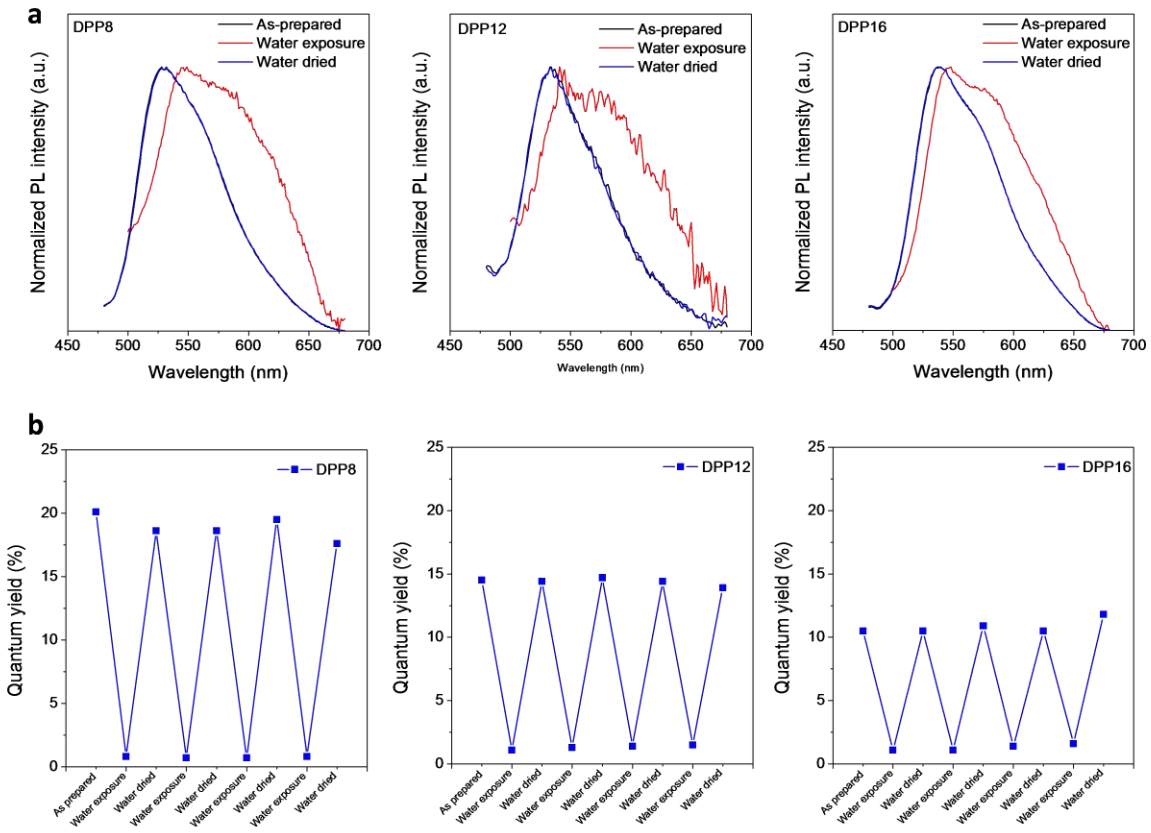

Figure 5.5 Optical properties of the sensor system. (a) Photoluminescence spectrum of a sensor with DPP8 (left), DPP12 (middle), and DPP16 (right) for as-prepared, water exposure, and water dried state. (b) Fluorescence quantum yield trend of a sensor with DPP8 (left), DPP12 (middle), and DPP16 (right) upon multiple water exposure and drying.

It is worth to note that the QY of as-prepared sensors gradually decreases as increasing alkyl chain length of the DPP derivative (**Figure 5.4c**). As discussed above, alteration of the alkyl chain length affects the interaction between the DPP molecules and silica gel substrates manifested in the Rf value difference. As the alkyl side chain gets longer the corresponding DPP derivative becomes more hydrophobic and less polar, which weaken its interaction with a highly polar and hydrogen bonding favorable silica gel plate and makes it to be more prone to molecular aggregation, thereby its QY gradually decreases.

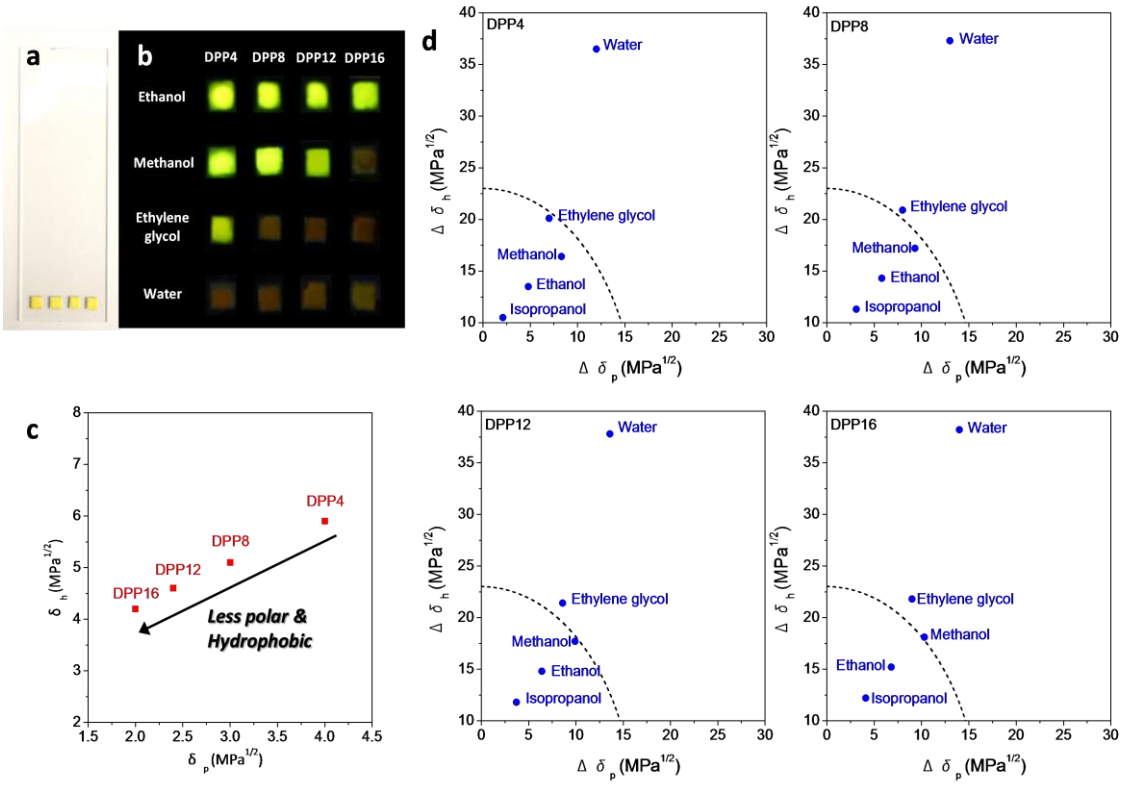

Figure 5.6 Highly selective alcohol and water sensor kit made of DPP derivatives. (a) An optical image of the sensor kit under room light. From the left to right, DPP4, 8, 12, 16 is coated on a square silica gel substrate, respectively, and the silica squares are attached to a slide glass. (b) Fluorescence image of the sensor kit upon alcohols and water exposure (under 365 nm UV light). The sensor kit is able to clearly distinguish ethanol, methanol, ethylene glycol, and water. (c) Trend of Hansen solubility parameter, δ_p (polar cohesion parameter) and δ_h (hydrogen bonding cohesion parameter), of the DPP derivatives. As alkyl chain length increases the molecule become less polar and more hydrophobic. (d) Mapping of $\Delta\delta_p$ (= δ_p(solvent) - δ_p(molecule)) and $\Delta\delta_h$ (= δ_h(solvent) – δ_h(molecule)) for each DPP derivatives and each solvent analyte. The trend of fluorescence change upon different alcohol (or water) exposure clearly matched with the location of each spot in the plot, compared to the suggested threshold curve ($2\Delta\delta_p^2 + \Delta\delta_h^2 = 23^2$).

In parallel, the alkyl chain length also affects the interaction between the DPP derivatives and solvent analytes, which enables a highly selective alcohols and water sensor with large signal contrast. **Figure 5.6a** shows a single sensor kit composed of four silica squares coated with DPP4, 8, 12, and 16. Upon exposure to ethanol, methanol, ethylene glycol, and water the DPP

sensors responded differently and clearly distinguished the four similar solvent analytes (**Figure 5.6b**). Upon ethanol exposure, all four DPP derivatives maintain bright green fluorescence. However, upon methanol exposure, the fluorescence of DPP16 is significantly quenched into dim reddish color, producing a completely different fluorescence pattern of the sensor kit. On the other hand, upon ethylene glycol exposure, DPP8, 12, as well as 16 shows fluorescence quenching. As we presented above, in case of water, all four derivatives exhibit fluorescence quenching with large color change. The fluorescence change occurred immediately upon exposure to the solvents.

The intriguing selectivity in sensing alcohols and water is ascribed to the difference in interaction between DPPs and solvent analytes, which can be directly linked to the solubility of the molecules in solvents. We rationalized the fluorescence signal trend of the presented sensor system based on the solubility parameter.[27–29] From the Hansen solubility parameter calculation of molecules, DPP derivatives are characterized to have gradual δ_p (polar cohesion parameter, 4~2) and δ_h (hydrogen bonding cohesion parameter, 5.9~4.2) as alkyl chain length changes, which means molecules become more hydrophobic and less polar as the alkyl side chain length increases (**Figure 5.6c** and **Table 5.1**).[29] Since the smaller difference in the solubility parameter between a solvent and a molecule implies a better solubility of the

Table 5.1 Calculated solubility parameters of the DPP derivatives[29]

Solubility Parameter	δ_d ($MPa^{1/2}$)	δ_p ($MPa^{1/2}$)	δ_h ($MPa^{1/2}$)	δ ($MPa^{1/2}$)
DPP4	19.6	4	5.9	20.9
DPP8	18.8	3	5.1	19.7
DPP12	18.3	2.4	4.6	19.0
DPP16	18	2	4.2	18.6

Table 5.2 Solubility parameters of alcohols and water[28]

Solubility Parameter	δ_d ($MPa^{1/2}$)	δ_p ($MPa^{1/2}$)	δ_h ($MPa^{1/2}$)	δ ($MPa^{1/2}$)
Isopropanol	15.8	6.1	16.4	23.5
Ethanol	15.8	8.8	19.4	26.6
Methanol	15.1	12.3	22.3	29.7
Ethylene Glycol	17	11	26	32.9
Water	15.5	16	42.4	47.9

molecule in the solvent, the difference in the solubility parameter between the DPP derivatives is highly likely to induce different aggregation behavior of the DPP derivatives upon exposure to specific alcohol. For quantitative comparison, $\Delta\delta_p$ (= δ_p(solvent) - δ_p(molecule)) and $\Delta\delta_h$ (= δ_h(solvent) – δ_h(molecule)) between each DPP derivative and each solvent analyte were calculated and plotted in **Figure 5.6d**. As the number of hydroxyl group and alky chain length varies, the solubility parameter of alcohols and water also varies (**Table 5.2**) and results in different $\Delta\delta_p$ and $\Delta\delta_h$ for each DPP derivative.[28] From the two dimensional mapping of $\Delta\delta_p$ and $\Delta\delta_h$, water locates farthest from the origin for all four DPP derivatives, thereby providing a bad solubility power and consequent aggregation-induced fluorescence quenching (**Figure 5.6d**). Moreover, the trend of the fluorescence change upon different alcohol exposure can be reasonably explained with the solubility threshold curves in the plot: (i) only water is outside of the threshold curve in the DPP4 plot, (ii) the water and ethylene glycol are outside of the threshold curve in the DPP8 and DPP12 plots, and (iii) DPP16 plot shows that ethanol locates inside of the calculated threshold curve while methanol, ethylene glycol, and water are outside of the curve. This rationale is further validated by absence of fluorescent quenching upon exposure of sensor device to isopropanol which locates inside of the threshold curve for all four DPPs (**Figure 5.6d**). Therefore, DPP derivatives' different solubility in the tested alcohols produces distinct aggregation status of DPPs on a silica gel substrate and distinguishes alcohols from their bright fluorescence or aggregation-induced fluorescence quenching as a sensory signal (**Figure 5.6d**).

5.3. Conclusion

In summary, we presented a novel type of optical solvent sensor system developed on subtle differences in interaction between solvent analytes, fluorescent DPP derivatives, and a mesoporous silica gel substrate as a new sensing mechanism. Gradual change in the chemical structure of the DPP derivatives alters their interaction with the silica gel substrate and solubility in alcohols and waters, which makes distinct intermolecular aggregation of the DPP derivatives on the silica gel plate depending on the solvent environment and produces fluorescence color and intensity change as a sensory signal. The devised sensor device, which is fabricated with simple drop casting of the fluorescent DPP derivative solutions onto a silica gel substrate, exhibited a completely reversible fluorescence signal change with large signal contrast both in color and fluorescence quantum efficiency, which allows selective solvent detection by simple optical observation with naked eye under UV light. Highly selective alcohol and water sensor system which can clearly distinguish the ethanol, methanol, ethylene glycol and water is demonstrated, regardless of the similarity in chemical structure and properties of the analytes.

5.4. Experimental Section

5.4.1. Methods

5.4.1.1. Sensor Fabrication and Fluorescence Signal Observation

The 10^{-3} M solutions of the fluorescent DPP molecules were dispensed onto a silica gel substrate. After solvent evaporation by brief heating at 150 ^{o}C, the samples were measured for the as-prepared (or as-cast) optical properties and used as a sensor without further treatment. Fluorescence signal change was monitored under 365 nm UV light after short dipping the sensor unit into target analyte, and the recovery of the fluorescence was monitored under 365 nm UV light after heating of the sensor unit at 150 ^{o}C for 2 min.

5.4.1.2. Spectroscopic Characterization

Photoluminescence spectrum, absolute quantum yield of the samples were characterized using PTI QuantaMasterTM spectrofluorometers equipped with an integrating sphere.

5.4.1.3. Solubility Parameter Calculation

The Hansen solubility parameters of DPP derivatives (**Table 5.1**) were caculated through the method of Hoftyzer and Van Krevelen[29] using solubility parameter calculation software (the HSPiP, 4th Edition 4.1.07). The Hansen solubility parameters of the solvent analytes (**Table 5.2**) were cited from a literature.[28]

5.4.2. Materials and Synthesis

All solvent analytes and silica gel substrate were purchased from commercial suppliers (Sigma-Aldrich, Acros, Merck, EMD Millipore). The DPP derivatives were synthesized as previously described manner.[24]

5.5. Author Contribution

K. Chung, D. Seo, D. S. Yang, M. S. Kwon, and J. Kim, Highly Selective Alcohol and Water Sensor with Large Fluorescence Signal Contrast based on Solvent-Fluorophore-Substrate Interaction. *Manuscript submitted.*

Kyeongwoon Chung and Jinsang Kim designed the project, and Jinsang Kim directed the project. Kyeongwoon Chung and Min Sang Kwon synthesized the series of molecules. Optical and sensor characteristics are analyzed by Kyeongwoon Chung and partly by Deokwon Seo and Da

Seul Yang. Kyeongwoon Chung and Jinsang Kim wrote the manuscript for publication, and all other authors had input.

5.6. References and Notes

1. See news article: Malwani hooch tragedy: 'Methanol supplier' Atiq arrested from Delhi (http://timesofindia.indiatimes.com/city/mumbai/Malwani-hooch-tragedy-Methanol-supplier-Atiq-arrested-from-Delhi/articleshow/47791144.cms). (2015).
2. See article: Methanol Poisoning in Rivers State, Nigeria (http://www.globalhealthnow.org/news/methanol-poisoning-in-rivers-state-nigeria). (2015).
3. J. A. Kruse, Methanol poisoning. Intensive Care Med. **18,** 391–397 (1992).
4. Q. Wan, Q. H. Li, Y. J. Chen, T. H. Wang, X. L. He, J. P. Li, C. L. Lin, Fabrication and ethanol sensing characteristics of ZnO nanowire gas sensors. Appl. Phys. Lett. **84,** 3654 (2004).
5. J. Liu, X. Wang, Q. Peng, Y. Li, Vanadium Pentoxide Nanobelts: Highly Selective and Stable Ethanol Sensor Materials. Adv. Mater. **17,** 764–767 (2005).
6. P. P. Sahay, R. K. Nath, Al-doped ZnO thin films as methanol sensors. Sensors Actuators B Chem. **134,** 654–659 (2008).
7. T. Someya, J. Small, P. Kim, C. Nuckolls, J. T. Yardley, Alcohol Vapor Sensors Based on Single-Walled Carbon Nanotube Field Effect Transistors. Nano Lett. **3,** 877–881 (2003).
8. D. L. McCorkle, R. J. Warmack, S. V. Patel, T. Mlsna, S. R. Hunter, T. L. Ferrell, Ethanol vapor detection in aqueous environments using micro-capacitors and dielectric polymers. Sensors Actuators B Chem. **107,** 892–903 (2005).
9. A. A. Athawale, S. V. Bhagwat, P. P. Katre, Nanocomposite of Pd–polyaniline as a selective methanol sensor. Sensors Actuators B Chem. **114,** 263–267 (2006).
10. M. Y. Lee, H. J. Kim, G. Y. Jung, A.-R. Han, S. K. Kwak, B. J. Kim, J. H. Oh, Highly sensitive and selective liquid-phase sensors based on a solvent-resistant organic-transistor platform. Adv. Mater. **27,** 1540–1546 (2015).
11. T. A. Dickinson, J. White, J. S. Kauer, D. R. Walt, A chemical-detecting system based on a cross-reactive optical sensor array. Nature **382,** 697–700 (1996).
12. C.-G. Niu, P.-Z. Qin, G.-M. Zeng, X.-Q. Gui, A.-L. Guan, Fluorescence sensor for water in organic solvents prepared from covalent immobilization of 4-morpholinyl-1, 8-naphthalimide. Anal. Bioanal. Chem. **387,** 1067–1074 (2007).
13. Z.-Z. Lu, R. Zhang, Y.-Z. Li, Z.-J. Guo, H.-G. Zheng, Solvatochromic behavior of a nanotubular metal-organic framework for sensing small molecules. J. Am. Chem. Soc. **133,** 4172–4174 (2011).
14. D. Citterio, K. Minamihashi, Y. Kuniyoshi, H. Hisamoto, S. Sasaki, K. Suzuki, Optical Determination of Low-Level Water Concentrations in Organic Solvents Using Fluorescent Acridinyl Dyes and Dye-Immobilized Polymer Membranes. Anal. Chem. **73,** 5339–5345 (2001).
15. C. Zhang, K. S. Suslick, A colorimetric sensor array for organics in water. J. Am. Chem.

Soc. **127,** 11548–11549 (2005).
16. S. H. Lim, L. Feng, J. W. Kemling, C. J. Musto, K. S. Suslick, An optoelectronic nose for the detection of toxic gases. Nat. Chem. **1,** 562–567 (2009).
17. N. A. Rakow, K. S. Suslick, A colorimetric sensor array for odour visualization. Nature **406,** 710–713 (2000).
18. T. Gupta, M. E. van der Boom, Optical sensing of parts per million levels of water in organic solvents using redox-active osmium chromophore-based monolayers. J. Am. Chem. Soc. **128,** 8400–8401 (2006).
19. B. Bag, A. Pal, Water induced chromogenic and fluorogenic signal modulation in a bi-fluorophore appended acyclic amino-receptor system. Org. Biomol. Chem. **9,** 915–925 (2011).
20. S. Ishihara, N. Iyi, J. Labuta, K. Deguchi, S. Ohki, M. Tansho, T. Shimizu, Y. Yamauchi, P. Sahoo, M. Naito, H. Abe, J. P. Hill, K. Ariga, Naked-eye discrimination of methanol from ethanol using composite film of oxoporphyrinogen and layered double hydroxide. ACS Appl. Mater. Interfaces **5,** 5927–5930 (2013).
21. M. Devi, A. Dhir, C. P. Pradeep, A Tris(hydroxymethyl)aminomethane-Rhodamine Spirolactam Derivative as Dual Channel pH and Water Sensor and Its Application to Bio Imaging. European J. Org. Chem. **2015,** 4650–4657 (2015).
22. M. C. Lonergan, E. J. Severin, B. J. Doleman, S. A. Beaber, R. H. Grubbs, N. S. Lewis, Array-Based Vapor Sensing Using Chemically Sensitive, Carbon Black−Polymer Resistors. Chem. Mater. **8,** 2298–2312 (1996).
23. D.-H. Park, J. Hong, I. S. Park, C. W. Lee, J.-M. Kim, A Colorimetric Hydrocarbon Sensor Employing a Swelling-Induced Mechanochromic Polydiacetylene. Adv. Funct. Mater. **24,** 5186–5193 (2014).
24. K. Chung, M. S. Kwon, B. M. Leung, A. G. Wong-Foy, M. S. Kim, J. Kim, S. Takayama, J. Gierschner, A. J. Matzger, J. Kim, Shear-Triggered Crystallization and Light Emission of a Thermally Stable Organic Supercooled Liquid. ACS Cent. Sci. **1,** 94–102 (2015).
25. R. P. W. Scott, The silica-gel surface and its interactions with solvent and solute in liquid chromatography. Faraday Symp. Chem. Soc. **15,** 49 (1980).
26. K. Chung, A. McAllister, D. Bilby, B.-G. Kim, M. S. Kwon, E. Kioupakis, J. Kim, Designing interchain and intrachain properties of conjugated polymers for latent optical information encoding. Chem. Sci. **6,** 6980–6985 (2015).
27. C. M. Hansen, *Hansen solubility parameters: A user's handbook, 2nd edition*. (CRC Press, Taylor & Francis Group, LLC., Boca Raton, 2007).
28. J. Brandrup, E. H. Immergut, E. A. Grulke, *Polymer handbook, 4th edition.* (John Wiley & Sons, Inc., New York, 1999).
29. D. W. Van Krevelen, *Properties of polymers, 3rd edition.* (Elsevier B. V., Amsterdam, 1997).

CHAPTER 6

Conclusion and Insights

Rational molecular design regulating both the intrinsic intramolecular properties and the intermolecular packing is inevitable to fully realize distinct optoelectronic properties of organic conjugated molecules for applications. In this dissertation, thorough investigation on the molecular design strategies is presented focusing on the relationship between chemical structural parameters of organic conjugated molecules and polymers and their intramolecular and intermolecular properties, which enables us to achieve unique optoelectronic properties via distinct supramolecular interactions and assemblies for various optical, electronic, and biomedical applications.

In Chapter 2, through controlling the intermolecular interactions via molecular design, unique thermally stable supercooled liquid of a conjugated organic molecular system is presented. A supercooled liquid is generally considered as a kinetically trapped short-lived state. Different from the general observation, a crystalline diketopyrrolopyrrole derivative, DPP8, is observed to form thermally stable supercooled liquid which does not transform back to its crystal phase even after multiple thermal cycles of molten DPP8. The origin of this stable supercooled liquid is ascribed to the small Gibbs free energy difference (ΔG) between the supercooled liquid and the crystalline solid of DPP8, which enlarges the critical radius of nucleation (r^*) and thereby restricts crystal nucleation in the supercooled liquid even in the temperature range of 100 ^{o}C

below its melting temperature. From a systematic investigation performed with DPP8 and its derivatives on the correlation between chemical structures and thermal stability of their supercooled liquid, this small ΔG between the two phases of DPP8 is attributed to the delicate force balance between the aromatic interaction among DPP cores and the van der Waals interaction among aliphatic side chains acting in opposite directions. More intriguingly, the supercooled liquid DPP8 is converted back to its crystalline solid phase under a shear condition accompanied by tremendous increase in photoluminescence intensity and color change. The role of shear force in the shear-triggered lighting-up crystallization was scrutinized by means of sonication test and heterogeneous nucleation test, confirming that the shear force induces density fluctuation of molecules, thereby helping embryos surpass the critical radius of nucleation to form stable nuclei. Different modes of the shear-triggered crystallization are successfully demonstrated by applying shear force to the supercooled liquid DPP8 at different temperatures; direct writing of fine fluorescent patterns is demonstrated at room temperature and propagating amplification of fluorescence is presented at 120 ^{o}C. Furthermore, the shear-triggered crystallization is accomplished by living cell attachment, demonstrating high sensitivity of the shear-triggered crystallization. The threshold shear stress to trigger crystallization was observed as low as 0.9 kPa which is comparable to the cells' traction force. Also, this threshold value is ca. million times more sensitive than the reported mechanochromic organic molecular systems. The shear-triggered crystallization of DPP8 by living cell attachment strongly suggests the possibility of applying this phenomenon to a highly sensitive novel sensor system with fluorescence turn-on signaling.

Molecular design consideration for interchain packing as well as intrinsic intrachain properties is also critical to fully utilize conjugated polymers' optoelectronic properties in the

solid state. Chapter 3 demonstrates a straightforward and effective conjugated polymer (CP) design strategy to devise optical properties of CPs for latent optical information encoding using CPs as security inks. Conventional CP design strategies have focused on the chemical structure design of CPs' conjugated backbone to mainly regulate the intrinsic intrachain properties of CPs. On the other hand, side chains of CPs have been considered mostly only as a solubilizing group nevertheless of their substantial impact on the interchain interaction. Differentiating from the general approaches, the synthesized CPs, P1, P2, and P3, are designed for distinct optical properties, by considering both intrachain and interchain properties via combined main chain and side chain design in a single CP system. The three CPs exhibit almost identical optical absorption spectra and color in solution, resulting from the essentially the same intrachain property which originates from the conjugated main chain design. However, the CPs in the solid state shows distinct gradation in color and absorption spectra due to the adjusted propensity to aggregation by rational side chain designs. The tailored optical properties are further emphasized in the demonstrated security ink application of CPs. The CPs cast onto a silica substrate retain the hardly distinguishable solution-like color among them, while reveals hidden information (pattern or letter) upon water dipping because of the distinct color gradation developed by CP aggregation.

For recent decades, CPs have become active components in the applications of electronic and energy devices. In these applications, CPs films are generally spin-cast and subsequently the CP chains are randomly oriented in the film. However, to fully utilize the optoelectronic properties of CPs, macroscopic alignment of CP chains is essential since CPs have a rigid rod-like structure and anisotropic properties originated from the one-dimensional p-orbital overlap along the conjugated main chain. In Chapter 4, design principles for directed CP alignment that has a

crucial impact on the optoelectronic applications of CPs are validated and expanded. First, three new CPs, NCP1, NCP2, and NCP3, are designed based on the preliminary design principles, (1) concentration-induced planarization unit, and (2) bulky side chains linked to (3) a tetrahedral carbon, with building blocks with different chemical structures. From the optical properties and alignment properties of the three newly designed CPs, we confirmed that the suggested design principles are generally applicable to different CP building blocks. In addition, four new CPs, NCP4, NCP5, NCP6, and NCP7 are prepared to identify additional design factors that largely affect the directed alignment of CPs. From the investigation on NCP4, the branching point of the side chain turned out to be important to accomplish efficient alignment of CPs; branching point near the conjugated backbone is necessary to prevent massive aggregation formation between CP chains so as to enable CPs to have suitable mobility for directed alignment. The role of concentration induced planarization unit is also scrutinized. CPs having an intrinsically planar conformation (NCP5 and NCP6) are not suitable for CP alignment since the CP aggregation is clearly observed in their absorption spectra even in diluted solutions. The role of S-F interaction unit for concentration induced planarization is further verified through replacement of S-F to S-O intramolecular interaction unit (NCP7). No alignment is observed from NCP7 even though NCP7 shows the same trend as CP1 and NCP1 in the absorption spectra and forms a lyotropic liquid crystalline phase confirmed by birefringence under the crossed polarizer. The result strongly implies that the low surface energy of fluoride and its consequent effect on the chain arrangement and wetting property play a considerable role on directed alignment of CPs. The thoroughly discussed insightful molecular design strategies for directed alignment of CPs open up the possibility of new CP design for various optoelectronic applications.

The characteristics of organic conjugated materials are prone to be largely influenced by the environmental aspects, such as applied substrate and surrounding solvent molecules. In Chapter 5, a novel type of optical sensor system is presented based on subtle differences in interaction between solvent analytes, fluorescent molecules, and a mesoporous silica gel substrate as a new sensing mechanism. The developed fluorescent DPP derivatives exhibits bright green fluorescence when they are dispersed onto a silica gel substrate, while the fluorescence undergoes significant color change to dim red together with emission quenching upon exposure to highly a polar (and/or hydrogen-bonding favorable) solvent due to the detachment of molecules from the silica gel surface and consequence development of molecular aggregation. The fluorescence quenching and recovery of the DPP derivatives upon solvent analyte exposure were demonstrated in a completely reversible manner, and the characteristics of the fluorescence change are precisely controlled by rationally designed interaction difference between substrate, fluorescent molecule, and solvents. By utilizing the different characteristic fluorescence responses of DPP derivatives upon solvent exposure, a sensor system is devised with multiple DPP derivatives in a single sensor kit. The sensor devices, which are fabricated through simple drop casting of the DPP derivative solutions onto a silica gel substrate, exhibit a large signal contrast both in fluorescence color and quantum efficiency and a high selectivity which can clearly distinguish ethanol, methanol, ethylene glycol and water, despite of their physicochemical similarity.

The works presented in this dissertation also suggest interesting future works which may further impact on various applications of organic conjugated molecules and polymers. First, based on the defined molecular features for CP alignment, new alignment-capable CPs with distinct properties, such as n-type or p-type semiconducting, polarized emission with specific

colors, and responsive to stimuli or biomolecules, can be further designed for target applications. Furthermore, the charge transport properties of aligned CPs can be further improved. The distance between CP chains in the solid state largely affects the interchain hopping rate of charge carriers in the charge transport process. It can further be reduced in the aligned CP films by introducing reconfigurable form-factor units and/or cleavable side chains in the CP design. On the other hand, the thermally stable supercooled liquid system has a great potential in biomedical applications. Based on the built insight on the correlation between the molecular design and crystallization behavior, the supercooled liquid system can be further adjusted to tune the threshold force to induce the shear-triggered crystallization. Then the series of supercooled liquid films having gradually tuned sensitivity will be an excellent tool to sort cells having different traction forces. The newly suggested sensing mechanism based on the subtle interaction difference between substrate, fluorophore, and solvent can be further utilized for various chemical sensors by designing suitable fluorophores having distinct interactions with an applied substrate and target analytes.